Universidad de Alcalá
COMISIÓN DE ESTUDIOS OFICIALES
DE POSGRADO Y DOCTORADO

ACTA DE EVALUACIÓN DE LA TESIS DOCTORAL

(FOR EVALUATION OF THE ACT DOCTORAL THESIS)

Año académico (*academic year):* 2016/17

DOCTORANDO *(candidate PHD)*: **NUÑEZ CASCAJERO, ARÁNTZAZU**

PROGRAMA DE DOCTORADO *(Academic Committee of the Programme)*: **D332 DOCTORADO EN ELECTRÓNICA:SISTEMAS ELECTRÓNICOS AVANZADOS.SISTEMAS INTELIGEN**
DEPARTAMENTO DE *(Department)*: **ELECTRÓNICA**
TITULACIÓN DE DOCTOR EN *(Phd title)*: **DOCTOR/A POR LA UNIVERSIDAD DE ALCALÁ**

En el día de hoy 22/06/17, reunido el tribunal de evaluación, constituido por los miembros que suscriben el presente Acta, el aspirante defendió su Tesis Doctoral **con Mención Internacional** (*In today assessment met the court, consisting of the members who signed this Act, the candidate defended his doctoral thesis with mention as International Doctorate),* elaborada bajo la dirección de (*prepared under the direction of*) FERNANDO BERNABÉ NARANJO VEGA // MIGUEL GONZÁLEZ HERRÁNEZ.

Sobre el siguiente tema *(Title of the doctoral thesis)*: *DEVELOPMENT OF NITRIDES BASED ON INN FOR SENSOR APPLICATIONS*

Finalizada la defensa y discusión de la tesis, el tribunal acordó otorgar la CALIFICACIÓN GLOBAL[2] de (**no apto, aprobado, notable** y **sobresaliente)** *(After the defense and defense of the thesis, the court agreed to grant the GLOBAL RATING (fail, pass, good and excellent)*: SOBRESALIENTE

Alcalá de Henares, a 22 de JUNIO de 2017

Fdo. *(Signed)*: CARLOS PRIETO DE CASTRO

Fdo. *(Signed)*: SERGIO FERNÁNDEZ GARRIDO

Fdo. *(Signed)*: OSCAR ESTEBAN MARTÍNEZ

FIRMA DEL ALUMNO (candidate's signature),

Arantxa N.C.

Fdo. *(Signed)*: ARÁNTZAZU NÚÑEZ CASCAJERO

Con fecha 29 de junio de 2017 la Comisión Delegada de la Comisión de Estudios Oficiales de Posgrado, a la vista de los votos emitidos de manera anónima por el tribunal que ha juzgado la tesis, resuelve:

☒ Conceder la Mención de "Cum Laude"
☐ No conceder la Mención de "Cum Laude"

La Secretaria de la Comisión Delegada

[2] La calificación podrá ser "**no apto**" "**aprobado**" "**notable**" y "**sobresaliente**". El tribunal podrá otorgar la mención de "cum laude" si la calificación global es de sobresaliente y se emite en tal sentido el voto secreto positivo por unanimidad. (*The grade may be "**fail**" "**pass**" "**good**" or "**excellent**". The panel may confer the distinction of "cum laude" if the overall grade is "Excellent" and has been awarded unanimously as such after secret voting.).*

INCIDENCIAS / OBSERVACIONES:
(Incidents / Comments)

SIN INCIDENCIAS.

Universidad de Alcalá

COMISIÓN DE ESTUDIOS OFICIALES
DE POSGRADO Y DOCTORADO

En aplicación del art. 14.7 del RD. 99/2011 y el art. 14 del Reglamento de Elaboración, Autorización y Defensa de la Tesis Doctoral, la Comisión Delegada de la Comisión de Estudios Oficiales de Posgrado y Doctorado, en sesión pública de fecha 29 de junio, procedió al escrutinio de los votos emitidos por los miembros del tribunal de la tesis defendida por *NUÑEZ CASCAJERO, ARÁNTZAZU*, el día 22 de junio de 2017, titulada *DEVELOPMENT OF NITRIDES BASED ON INN FOR SENSOR APPLICATIONS*, para determinar, si a la misma, se le concede la mención "cum laude", arrojando como resultado el voto favorable de todos los miembros del tribunal.

Por lo tanto, la Comisión de Estudios Oficiales de Posgrado **resuelve otorgar** a dicha tesis la

MENCIÓN "CUM LAUDE"

Alcalá de Henares, 11 julio de 2017
EL PRESIDENTE DE LA COMISIÓN DE ESTUDIOS
OFICIALES DE POSGRADO Y DOCTORADO

Firmado digitalmente por VELASCO PEREZ JUAN RAMON - DNI 03087239H
Fecha: 2017.07.12 22:45:50 +02'00'

Juan Ramón Velasco Pérez

Copia por e-mail a:
Doctorando: NUÑEZ CASCAJERO, ARÁNTZAZU
Secretario del Tribunal: ÓSCAR ESTEBAN MARTÍNEZ.
Directores de Tesis: FERNANDO BERNABÉ NARANJO VEGA // MIGUEL GONZÁLEZ HERRÁEZ

Universidad de Alcalá

ESCUELA DE DOCTORADO
Servicio de Estudios Oficiales de Posgrado

DILIGENCIA DE DEPÓSITO DE TESIS.

Comprobado que el expediente académico de D./Dª ARÁNTZAZU NÚÑEZ CASCAJERO reúne los requisitos exigidos para la presentación de la Tesis, de acuerdo a la normativa vigente, y habiendo presentado la misma en formato: ☒ soporte electrónico ☐ impreso en papel, para el depósito de la misma, en el Servicio de Estudios Oficiales de Posgrado, con el nº de páginas: 201 se procede, con fecha de hoy a registrar el depósito de la tesis.

Alcalá de Henares a 24 de ABRIL de 2017

Aurora Juárez Abril

Fdo. El Funcionario

Programa de Doctorado en Electrónica:
Sistemas Electrónicos Avanzados, Sistemas Inteligentes

Development of nitrides based on InN for sensor applications

Tesis presentada por:

Arántzazu Núñez Cascajero

2017

Universidad de Alcalá

DEPARTAMENTO DE ELECTRÓNICA
Edificio Politécnico
Campus Universitario s/n
28805 Alcalá de Henares (Madrid)
Teléfono: 91 885 65 40
Fax: 91 885 65 91
dpto.electronica@uah.es

Dr. Fernando B. Naranjo Vega, Profesor Titular de la Universidad de Alcalá

Dr. Miguel González Herráez, Profesor Titular de la Universidad de Alcalá

INFORMAN: Que la Tesis Doctoral titulada "**DEVELOPMENT OF NITRIDES BASED ON InN FOR SENSOR APPLICATIONS**" presentada por Dña. Arántzazu Núñez Cascajero, y realizada bajo la dirección de los doctores D. Fernando B. Naranjo Vega y D. Miguel González Herráez, dentro del campo Tecnología Electrónica, reúne los méritos de calidad y originalidad para optar al Grado de Doctor.

Alcalá de Henares, a 18 de Abril de 2017

Fdo. D. Fernando B. Naranjo Vega

Fdo. D. Miguel González Herráez

Universidad de Alcalá

DEPARTAMENTO DE ELECTRÓNICA
Edificio Politécnico
Campus Universitario s/n
28805 Alcalá de Henares (Madrid)
Teléfono: 91 885 65 40
Fax: 91 885 65 91
dpto.electronica@uah.es

Dra. Sira Elena Palazuelos Cagigas, Directora del Departamento de Electrónica de la Universidad de Alcalá,

INFORMA: Que la Tesis Doctoral titulada "**DEVELOPMENT OF NITRIDES BASED ON InN FOR SENSOR APPLICATIONS**" presentada por Dña. Arántzazu Núñez Cascajero, y dirigida por los doctores D. Fernando B. Naranjo Vega y D. Miguel González Herráez, cumple con todos los requisitos científicos y metodológicos, para ser defendida ante un Tribunal.

Alcalá de Henares, a 18 de Abril de 2017

UNIVERSIDAD DE ALCALÁ, PATRIMONIO DE LA HUMANIDAD

Fdo. Dña. Sira Elena Palazuelos Cagigas

Programa de Doctorado en Electrónica:
Sistemas Electrónicos Avanzados, Sistemas Inteligentes

Development of nitrides based on InN for sensor applications

Tesis presentada por:

Arántzazu Núñez Cascajero

Directores:

Dr. Fernando B. Naranjo Vega

Dr. Miguel González Herráez

Alcalá de Henares, 2017

Agradecimientos

Este camino comenzó hace ya 5 años, hace 5 años pisé por primera vez el Campus Externo de la Universidad de Alcalá y conocí al Dr. Fernando Naranjo y al Dr. Miguel González, recuerdo la primera vez que entré en el laboratorio de óptica y en el sputtering durante la entrevista, nada más entrar dije "¡pero si esto no es un laboratorio!", claro yo venía de laboratorios de azulejos blancos, con reactivos químicos por doquier, campanas extractoras, matraces, probetas… y para mí todo esto era nuevo y diferente… sin embargo, ellos se animaron a darme una oportunidad y así fue como empezó esta andadura.

Gracias a ellos he aprendido un montón de cosas que no sabía y aunque el camino no siempre ha sido liso y fácil de llevar han estado ahí para ayudarme a sortear las distintas piedras que se nos han ido poniendo delante.

Pero esto no hubiese sido posible sólo gracias a ellos, también han colaborado en hacer el camino más llevadero Laura, enseñándome todo lo que sé del sputtering y ayudándome en lo que para mí era el mundo de la óptica, ese al que tanto miedo le tenía y que gracias a ella y a Marco le he ido perdiendo un poco el miedo… Laura ha hecho que los días de sputtering fuesen más llevaderos, hubo un tiempo en el que hasta hicimos dos turnos porque las muestras se volvían excesivamente largas, desde aquí quiero agradecerte toda la ayuda puesto que sin ella no habría sido posible realizar todas las muestras que he hecho durante esta tesis. A Marco debo agradecerle la paciencia por esos días de laboratorio en los que le hacía trabajar completamente a oscuras y gracias a sus conocimientos de LabView me ayudó a que esos días a oscuras no fuesen eternos.

También agradecer al Dr. Óscar Esteban su constante ayuda y conocimientos durante la fabricación de los SPRs puesto que gracias a él mi mundo empezó a ser menos negro.

Por otra parte, quiero agradecer a la Dra. Eva Monroy por su gran acogida durante la estancia en Grenoble, por enseñarme a manejarme en los laboratorios de allí y ayudarme de forma constante durante la estancia y durante las largas correcciones de los artículos posteriormente. Y la Dra. Sirona Valdueza por su ayuda en Grenoble y su esfuerzo para la realización de las células solares.

Y como no todo es trabajo, también quiero agradecer a Inés, Miguel y el resto de GRIFOs los momentos de esparcimiento durante las comidas, me hubiese gustado poder compartir más con todos vosotros, pero la verdad es que el vivir tan lejos siempre me complicaba acudir a las distintas quedadas que realizabais.

Por último, quiero agradecer a mi familia y a mis amigos el haberme apoyado durante todos estos años, en particular a mi padre, a mi hermana, a Jorge, a Javi, a Paula y a Jon porque gracias a ellos y a su paciencia esto también ha sido posible, ellos son los que han aguantado mis momentos de frustración cuando no salían las cosas, mis momentos de alegría cuando empezaron a salir y mis momentos de estrés cuando pensé que esto nunca llegaría a su fin. Gracias también a mi madre porque, aunque no esté presente, su educación pasada me ha hecho llegar a donde estoy y me hubiese gustado que viese todo lo que he conseguido.

Gracias a todos y cada uno de vosotros, también gracias a los que no he nombrado pero que estáis ahí siempre, por dejarme ser como soy, por comprenderme y ayudarme en todo momento.

Abstract

The unique properties of the III-nitrides, their high radiation hardness, high thermal stability and wide direct band gap makes them interesting for its application in electronic and opto-electronic devices.

$Al_xIn_{1-x}N$ is of particular interest because its band gap energy can be tuned between 0.7 to 6.2 eV depending on the alloy composition so that it is possible to engineer the electronic structure for each specific application.

It has been grown by different techniques, among them, radio frequency reactive sputtering allows deposition in a wide range of substrate types and temperatures, these advantages together with the low cost of the technique are the reasons for which sputtering technique has been selected for this Thesis.

Several substrates such as sapphire, p-silicon (111), glass and optical fibers have been used for growing $Al_xIn_{1-x}N$ by radio frequency reactive sputtering. The growth conditions of $Al_xIn_{1-x}N$ have been optimized for the different substrates by studying its structural, chemical, morphological, electrical and optical properties.

$Al_xIn_{1-x}N$ layers grown with the best growth conditions were processed into devices. The layers grown on sapphire substrates were processed into photoconductors. Their characterization shows a strongly sublinear response with the optical power and a smooth drop of the responsivity for excitation below the band gap. Also these devices present persistent photoconductivity effects. On the other hand, the layers grown on p-silicon (111) have been processed as solar cells, it has been demonstrated that the devices change their behavior when they are irradiated with light, the IV characteristics and external quantum efficiency are presented and show that the use of a 4 nm AlN buffer layer improves the device properties. The layers grown at low substrate temperature on optical fibers have been studied as

surface plasmon resonance sensors. It has been demonstrated that the homogeneity of the ternary compound acting as dielectric layer is very important to obtain better sensitivities and narrower transmittance dips. The use of different compositions in the dielectric layer allows the selection of the transmittance resonance dip. The metal layer thickness effect has also been studied showing that higher metal thicknesses increase the sensitivity with an increase in the full width at half maximum of the transmittance dip, so it has to be chosen taking into account the use of the sensor.

Resumen

Las propiedades únicas de los nitruros del grupo III, como son su alta resistencia a la radiación, su alta estabilidad térmica y su amplia energía de gap directa los hacen atractivos para su aplicación en dispositivos electrónicos y optoelectrónicos.

Entre ellos, el nitruro de aluminio e indio es de gran interés porque su energía de gap se puede variar entre 0.7 y 6.2 eV en función de la composición de la aleación. De esta forma es posible desarrollar cada capa teniendo en cuenta la aplicación para la que se va a usar.

El $Al_xIn_{1-x}N$ se ha crecido empleando distintas técnicas de crecimiento, en particular la técnica de pulverización catódica reactiva permite depositar $Al_xIn_{1-x}N$ sobre distintos sustratos y empleando un gran rango de temperaturas. Además de estas características esta técnica es de bajo coste y por ello se considera apropiada para emplear durante esta Tesis.

Distintos sustratos se han empleado durante esta Tesis para crecer $Al_xIn_{1-x}N$ por pulverización catódica, entre ellos se ha usado zafiro, silicio (111) tipo p, vidrio y fibra óptica. En primer lugar, se optimizan las condiciones de crecimiento óptimas para cada sustrato teniendo en cuenta las propiedades estructurales, químicas, morfológicas, eléctricas y ópticas de las capas.

Una vez conocidas las mejores condiciones de crecimiento para cada sustrato se realizan capas de $Al_xIn_{1-x}N$ sobre los distintos sustratos para distintas aplicaciones. Se han fabricado fotoconductores con las capas crecidas sobre zafiro, su caracterización muestra una respuesta altamente sublineal con la potencia óptica incidente, además la responsividad cae suavemente cuando se ilumina por debajo de la energía de gap. Todos los dispositivos estudiados presentan fotoconductividad persistente. Por otra parte, las capas crecidas sobre silicio (111) tipo p se

procesaron para desarrollar células solares, estos dispositivos presentan un cambio en su comportamiento bajo iluminación. Las curvas características IV y la eficiencia cuántica externa muestran que el uso de una capa amortiguadora de 4 nm de AlN mejora las propiedades del dispositivo. Las capas crecidas a temperatura ambiente sobre fibra óptica se emplearon como base para la fabricación de sensores de plasmón superficial. Se ha demostrado que la homogeneidad de la capa de $Al_xIn_{1-x}N$ empleada como material dieléctrico es muy importante para obtener alta sensibilidad y picos de absorción estrechos. Empleando distintas composiciones en la capa dieléctrica se puede elegir la longitud de onda a la que aparece el pico de absorción. Otro factor importante que se ha estudiado es el efecto del espesor de la capa metálica, observando que cuanto mayor es el espesor mayor es la sensibilidad del dispositivo, aunque se produce un aumento de la anchura a media altura del pico de absorción, por eso se debe elegir el espesor de la capa metálica según el uso que se le vaya a dar al sensor.

Index

List of figures

List of tables

List of symbols and abbreviations

a	→	Lattice constant: edge length of the basal hexagon
AFM	→	Atomic force microscopy
$Al_xIn_{1-x}N$	→	Aluminum indium nitride
AlN	→	Aluminum nitride
b	→	Bowing parameter
c	→	Lattice constant: height of the hexagonal prism
c	→	Light speed
C_{ij}	→	Elastic tensor
DC	→	Direct current
E_g	→	Band gap energy
e_{ij}	→	Piezoelectric coeficients
EQE	→	External Quantum Efficiency
E_{tot}	→	Total internal electric field
FESEM	→	Field emission scanning electron microscopy
FWHM	→	Full width at half maximum
GaN	→	Gallium nitride
G_R	→	Growth rate

h	→	Planck constant
HRXRD	→	High resolution X-ray diffraction
I	→	Current
I_0	→	Initial current
I_l	→	Light generated current
InN	→	Indium nitride
I_{ph}	→	Photocurrent
IR	→	Infrared
I_{sc}	→	Short circuit current
J_{sc}	→	Short circuit current density
k_B	→	Boltzman constant
LD	→	Laser diode
LED	→	Light emitting diode
LT	→	Low temperature
MBE	→	Molecular beam epitaxy
MOCVD	→	Metalorganic chemical vapour deposition
MOVPE	→	Metalorganic vapor phase epitaxy
n	→	Refractive index in SPR
n	→	Ideality factor in solar cells
P_{Al}	→	Power applied to the aluminum target
PL	→	Photoluminescence
P_{opt}	→	Optical power
P_{pz}	→	Piezoelectric polarization

P_{sp}	→	Spontaneous polarization
P_{tot}	→	Total crystal polarization
q	→	Electron charge
R	→	Responsivity
RF	→	Radio frequency
RIU	→	Refractive index units
RMS	→	Root mean surface
R_s	→	Series resistance
R_{sh}	→	Shunt resistance
RT	→	Room temperature
SPR	→	Surface plasmon resonance
T_S	→	Substrate temperature
UV	→	Ultraviolet
UWTFs	→	Uniform-waist tapered fibers
V	→	Voltage
V_d	→	Voltage diode
V_{oc}	→	Open circuit voltage
V_T	→	Thermal voltage
V_{Th}	→	Threshold voltage
WDX	→	Wavelength dispersive X-ray
x	→	Composition
XPS	→	X-ray photoelectron spectroscopy
XRR	→	X-ray reflectivity

ε_0	$\rightarrow$	Vaccum permitivity
ε_{kl}	$\rightarrow$	Strain
ε_r	$\rightarrow$	Dielectric constant
λ	$\rightarrow$	Wavelength
σ_{ij}	$\rightarrow$	Stress

Chapter 1

Introduction

This Chapter presents a brief overview of the state of the art of the growth and application of III-nitrides, particularly it is focused on the growth and applications of AlN, InN and $Al_xIn_{1-x}N$ layers. It also explains the objectives of this study and in the last part it describes how this manuscript is organized.

1.1. Motivation

In the last years, the group III-nitrides (AlN, GaN, InN and their ternary alloys) has arisen as one of the most important semiconductor materials and has attracted much attention. III-nitride semiconductors present unique properties such as high radiation hardness, and high thermal and chemical stability and a wide direct band gap (see Figure 1.1) [Amba98, Gil98, NeEk96, Stri92]. These properties make III-nitrides feasible for electronic and opto-electronic devices. The large differences in the metals ionic radii and bonding energies of N-metal lead to different lattice constants, electron affinities and band gap energies which challenge the epitaxial deposition of the III-nitrides and their alloys.

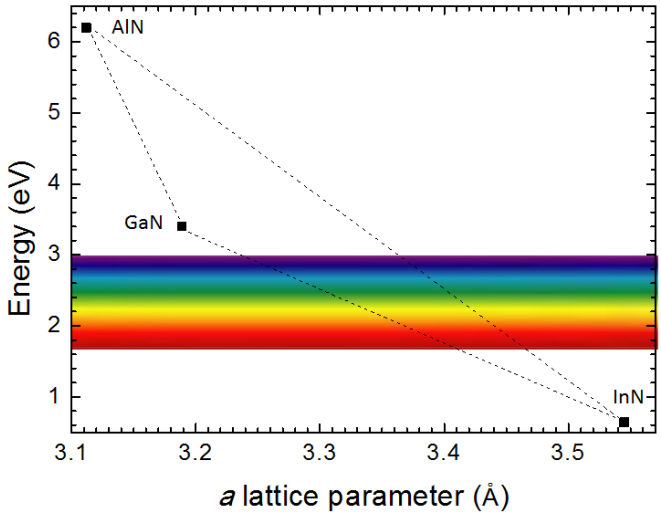

Figure 1.1. Direct band gap energy as a function of the in-plane lattice parameter for wurtzite III-nitrides.

1.1.1. Properties of InN, AlN and $Al_xIn_{1-x}N$

Among the group III-nitrides, InN attracted a lot of attention. Its low dissociation temperature (around 500°C) [WaYo04] joint to the fact that there are no lattice-matched substrates make difficult the achievement of high quality InN layers. During the 90s the sputtering technique was mainly used for growing InN and a band gap energy of ~1.9 eV [TaFo86] was assumed, but in the early 2000 the optimization of the growth by MBE led to a band gap energy of ~0.7 eV [WWYA02]. So the band gap energy of the InN was revised and the accepted value converged to 0.64 eV [BuTa05, WWSY03]. The differences between both band gap energies were explained by the high carrier concentration and low crystal quality that present the layers grown by sputtering. Other interesting properties of InN are its low effective mass and its high electron mobility and radiation resistance [BhHY03].

On the other hand, AlN is another attractive material due to its large direct band gap energy of 6.2 eV [YSZP73], its high acoustic velocity, strong piezoelectricity and mechanical robustness [Gil98], also it presents excellent chemical stability, high hardness, high thermal conductivity, high volume resistivity and low dielectric constant [KZWC12]. Due to strong chemical bonding, AlN has outstanding physical (high melting point and mechanical strength) and chemical properties.

The $Al_xIn_{1-x}N$ ternary alloy is of particular interest because its band gap can be tuned in a wide-range of direct band gaps depending on the composition, it ranges from the near infrared to the deep ultraviolet. This wide band gap range offers large possibilities to engineer the electronic structure for each specific application.

However, the growth of high-quality and single-phase $Al_xIn_{1-x}N$ remains challenging due to the large immiscibility gap of the alloy [FeBe02, HBDD07] and the large growth temperature difference between InN and AlN [NeEk96].

1.1.2. Growth of InN, AlN and $Al_xIn_{1-x}N$

Different techniques have been used for growing InN, AlN and $Al_xIn_{1-x}N$, they have been successfully grown by molecular beam epitaxy (MBE) [CWPH14, CWTY14, GKBB06, KAGR03, KSKF97, LDNH01, NFTK07, SHKY02, WWCT14, YMAN09] and metalorganic vapor phase epitaxy (MOVPE) [ADKA10, BRMG09, Hash94, HBDD07, KMCD11, LYTT08, TaKM07, YKNK98, YWYL11], with these techniques single-crystalline films with high electron mobility and low carrier concentration are achieved. However, MBE requires higher maintenance procedures than sputtering due to the ultra-high vacuum environment used. At the same time, in MOCVD growth very high growth temperatures are required to crack the process gases.

Sputtering deposition is a low cost technique that allows low temperature deposition thanks to the high kinetic energy of the ions involved in the growth process. It also permits the deposition of polycrystalline films on large area substrates using a low cost process, but at the expense of delivering layers with lower crystal quality than those grown by MOVPE or MBE. The use of this technique for growing InN overcomes the problem of the low decomposition temperature of InN [AHNA11, HaWo16, TaFo86, VIMG12, VNGL11]. It is also an attractive technique to synthesize AlN [GTNO06, HGCA02, MVNG13] and $Al_xIn_{1-x}N$ films [AfDI16b, AfDI16a, KuKF89, LDTD13, LTDC12, LüDW13, NMVN16, NVMM16, PPQO97, DXCL09, GOKT07, GTNO08, GYTN03, HCFG10, HCFW10, HDDS10, JiSG09], allowing the deposition in a wide range of temperatures and substrates. Most of the reports on the growth of $Al_xIn_{1-x}N$ layers by sputtering are focused on the use of a mixture of N_2 and Ar gases for generating the plasma, also a large number of reports use a single composite target. However,

as it is explained later we propose the use of pure nitrogen as reactive gas, this leads to lower deposition rates and thus to different layer properties; in InN layers grown by sputtering it has been demonstrated that when growing under pure nitrogen conditions better crystalline properties are achieved [GSMN99, VNGL10]. Also we propose the use of separate targets to achieve a better compositional control of the grown layer due to the large difference between the sputtering yield of Al and In [KuKF89].

1.1.3. Applications of InN, AlN and $Al_xIn_{1-x}N$

InN has emerged as a potential candidate for many applications including high-efficiency solar cells [Hash94, Mala03], opto-electronic, high speed and high-power electronic devices, optical coatings and low resistivity contact layers [Amba98, BhHY03, Stri92, Wu09]. Moreover, InN has received remarkable interest for the development of chemical sensors and biosensors due to its high surface donor density and the corresponding surface electron accumulation [ChSo08, ENDV11, LSES03], chemical inertness, and chemical recognition capabilities [ASGK13, ENDV11, SCGU10].

The properties of AlN films described previously make this material a suitable semiconductor for its application in optical components in the ultraviolet spectral region [TaKa11, TaKM06], deep ultra-violet light-emitting diodes (LEDs) [JJLK15, TaKM06], laser diodes (LDs), surface acoustic wave devices [AHEA04, RIAV12], micro-electro-mechanical systems [GITM09], field emission displays [GCZD15], thermoelectric devices and coating layers. The use of AlN as a buffer layer for the growth of GaN is widely accepted because in this way the lattice mismatch is reduced, the metal polarity is stabilized and the unwanted reactions between GaN and substrate are prevented [LWGX08, YKDY09, YLYW12]. AlN has also been used as a buffer layer for the growth of InN nanocolumns [MVNR16].

$Al_xIn_{1-x}N$ has application in light-emitting devices [MSTW15, WPMI15], opto/chemical sensing [WCHH09], multijunction solar cells [LDTD13, LTDC12, YIKH10], high electron mobility transistors [ESCA15, SMBM15] and Bragg reflectors [BDBK13, BDBL15, KBBF10]. Also it has been demonstrated that it can be lattice match to GaN when the $Al_xIn_{1-x}N$ composition is near x=0.83 [LFAW06].

In this work, we have proposed different applications for the $Al_xIn_{1-x}N$ layers grown by RF sputtering depending on the substrate that has been used.

Photoconductors are the proposed devices for the $Al_xIn_{1-x}N$ layers grown on sapphire due to the simplicity of the devices. Their operation is related with a change in conductivity induced by light.

On the other hand, the layers grown on silicon substrates have been proposed for solar cell application. The possibility of tuning its band gap energy makes $Al_xIn_{1-x}N$ a very interesting material for improving single-junction solar cells, this material could complement the already existing Si solar cells and maybe increase the now limited efficiency.

Finally, the $Al_xIn_{1-x}N$ layers grown on optical fibers are used as the dielectric layer in surface plasmon resonance sensors. This kind of sensors is widely used for chemical, biomedical and environmental monitoring due to its high sensitivity to small changes in the refractive index. The use of $Al_xIn_{1-x}N$ for the dielectric layer is desirable in order to expand the refractive index range of the sensor by tuning the Al composition.

1.2. Objective

This work focuses on the growth of aluminum indium nitride by RF sputtering and on its structural, chemical, morphological, electrical and optical characterization. The objectives of the work are specified below:

- Study the effect of the RF power applied to the aluminum target (0 – 150 W) and the substrate temperature (300 - 550°C) on the properties of the $Al_xIn_{1-x}N$ layers grown on sapphire and on p-Si (111) substrates under pure nitrogen plasma. The use of pure nitrogen instead of an argon and nitrogen mixture leads to lower deposition rates and thus the layer properties are highly affected.

- Improve the growth of $Al_xIn_{1-x}N$ layers grown on p-Si (111) by including an AlN buffer layer.

- Study the effect of growing at room and low temperature (100°C) on the properties of AlIN films grown on sapphire, p-Si (111) and glass substrates.

- Finally, we have studied the applications in which the developed layers can be used. Photoconductors, solar cells and surface plasmon resonance sensors have been studied as possible applications for the $Al_xIn_{1-x}N$ layers grown on sapphire, p-Si (111) and optical fibers, respectively.

This work has been performed within the framework of several projects from different institutions:

- Spanish Government projects: FASTCOM (TEC2009-14423-C02-02), CISTER (TEC2012-37958-C02-01), MAGMA (TEC2014-58843-R) and ANOMALOS (TEC2015-71127-C2-2-R).
- Community of Madrid project: SINFOTON (S2013/MIT-2790)
- Alcalá University projects: DIBOS (UAH2011/EXP24), DESLAP (CCG2013/EXP-052), SOLARSEN (CCG2014/EXP-051), AlInNano (CCG2015/EXP-014), PhotoAl (CCG2016/EXP-019).
- Alcalá University FPI grant.

1.3. Outline

This manuscript is divided into nine Chapters. After the introduction presented in this Chapter, Chapter 2 describes the properties of III-nitride materials with wurtzite structure. An explanation of the growth technique used in this work can be found in Chapter 3. The description of the characterization techniques used for studying the different properties of the grown layers is done in Chapter 4.

Chapter 5, Chapter 6 and Chapter 7 focuses on the experimental growth of $Al_xIn_{1-x}N$ layers on different substrates by RF sputtering. In particular, Chapter 5 describes the growth of $Al_xIn_{1-x}N$ layers on sapphire substrates, the influence of the power applied to the aluminum target and the substrate temperature on the structural, chemical, morphological, electrical and optical properties are investigated. In the case of Chapter 6, it describes the growth of $Al_xIn_{1-x}N$ layers on p-Si (111), the first part is focused in the effect of the power applied to the aluminum target and the substrate temperature on the properties of the layers, the second part describes the optimization of AlN on p-Si (111) so that it can be used as a buffer layer and finally this Chapter describes the effect of the AlN buffer layer

thickness on the properties of the $Al_xIn_{1-x}N$ layer. Chapter 7 describes the growth of $Al_xIn_{1-x}N$ layers at low temperature on different substrates and a comparison of the properties of $Al_xIn_{1-x}N$ layers grown at RT and 100°C between the different substrates is presented.

Chapter 8 describes the applications of the $Al_xIn_{1-x}N$ layers, it is divided into three sections, the first one describes the application of the $Al_xIn_{1-x}N$ layers grown on sapphire as photoconductor devices, the second part is focused on the processing of $Al_xIn_{1-x}N$ layers grown p-Si (111) into solar cells and finally in the third part the application of $Al_xIn_{1-x}N$ as surface plasmon resonance sensors is described using an optical fiber as substrate.

Finally, Chapter 9 indicates the conclusions achieved along this study while providing new ideas for further improvement of the work presented in this manuscript.

Chapter 2

Properties of III-Nitrides

In this Chapter the basic properties of III-nitrides are summarized. The structural, morphological and optical properties of InN, AlN and GaN are described; also data about lattice parameters, elastic coefficients, polarization values, semiconductor band gap energies, etc. are given.

2.1. Crystalline structure

III-nitrides (GaN, AlN, InN and their alloys) can crystallize in three crystal structures: wurtzite (α -phase), zinc-blend (β -phase) and rocksalt (γ -phase) (see Figure 2.1). The wurtzite structure is the most thermodynamically stable one and it is the one that appears at room temperature, however by epitaxial growth and using cubic substrates is possible to achieve a metastable zinc-blende structure. The rocksalt structure appears only at very high pressures and cannot be stabilized by the epitaxial growth.

From now on, only the wurtzite structure is going to be taken into account because it is the stable structure at room temperature and it is the one that present the layers under study.

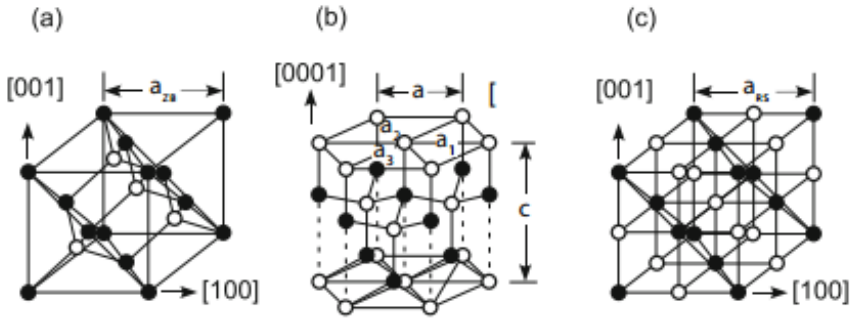

Figure 2.1. Crystalline structures of III-nitrides: (a) zincblende, (b) wurtzite and (c) rocksalt [Hana09].

The wurtzite structure has a hexagonal unit cell and thus it is characterized by two lattice constants; the out-plane, c (height of the hexagonal prism) and the in-plane, a (edge length of the basal hexagon) (see Figure 2.2, left). Each unit cell of the wurtzite structure contains six atoms of each type. It is formed by two hexagonal compact sublattices, one of metal (Al, Ga or In) atoms and the another of nitrogen (N) atoms, they are shifted vertically with respect to each other ideally by a distance u~5/8c, where u is the so called internal parameter defined as the anion-cation bond length along the [0001] axis.

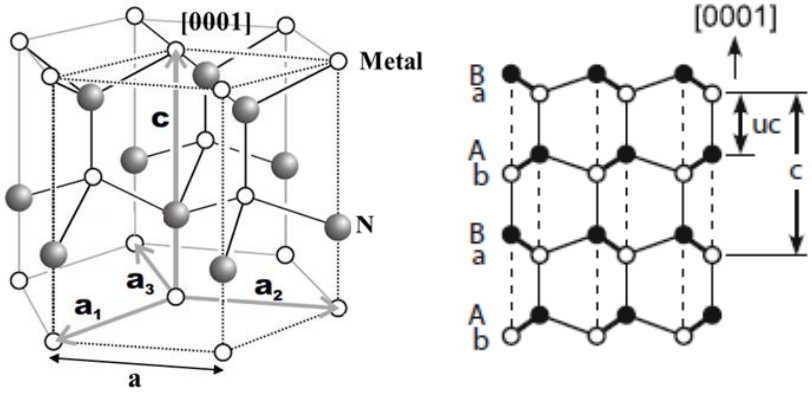

Figure 2.2. (Left) III-nitride wurtzite structure, the unit cell (dotted contour) is defined by the lattice vectors a_1, a_2 and c: modified from [März09]. (Right) Stacking periodicity for wurtzite ABABA... planes along the [0001] axis [Hana09].

In this structure, each group III atom is coordinated by four nitrogen atoms, they are bonded by sp^3-type hybrid bonds, this chemical bond has high strength and provides III-nitrides high melting point and high mechanical stability. Nitride structure is formed by alternating biatomic close-packed (0001) planes of metal and

N pairs, thus the stacking sequence of the (0001) plane is ABAB… in the (0001) direction (Figure 2.2, right).

In an ideal wurtzite crystal, the *c/a* ratio is 1.633 ($8/3^{1/2}$) and *u* is 3/8=0.375. The real nitride structure presents a certain deviation from these expected values, which depends on the metal cation. In Table 2.1 the values of the lattice parameters *a* and *c*, and the metal-N bond length *u* are summarized for AlN, GaN and InN at room temperature. The deviation from the ideality induces spontaneous polarization (see section 2.3.1).

Table 2.1. Room temperature wurtzite lattice parameters and c/a ratio of the different binary III-nitride semiconductors, a, c and c/a has been extracted form [VuMe03], while u has been extracted from [BeFV97]. Spontaneous polarization (P_{sp}) of metal-faced wurtzite structure [VuMe03].

	a (Å) [VuMe03]	**c (Å)** [VuMe03]	**c/a** [VuMe03]	**u** [BeFV97]	**P_{sp} (C/m²)** [VuMe03]
AlN	3.112	4.982	1.601	0.380	-0.090
GaN	3.189	5.185	1.626	0.376	-0.034
InN	3.545	5.703	1.612	0.377	-0.042

In ternary compounds, $A_xB_{1-x}N$, the lattices parameters can be estimated by using the Vegard's law [Vega21], this law assumes that the lattices parameters of the ternary compound can be linearly interpolated form the lattice parameters of the binary constituents and taking into account the composition (x), as it is shown in equations (2.1) and (2.2).

$$a_{A_xB_{1-x}N} = xa_{AN} + \ 1-x \ a_{BN} \tag{2.1}$$

$$c_{A_xB_{1-x}N} = xc_{AN} + \ 1-x \ c_{BN} \tag{2.2}$$

The crystal planes of a hexagonal unit cell are identified by four indices based on Miller-Bravais ones, these indices are denoted by the letters $\{h,k,i,l\}$ and related to the projection of the considered direction on the vectors of the basic cell $\{\overrightarrow{a_1},\overrightarrow{a_2},\overrightarrow{a_3},c\}$, respectively. As shown in the left Figure 2.2, $\overrightarrow{a_1},\overrightarrow{a_2},\overrightarrow{a_3}$ are the basal axes, while c is the vertical axis of the hexahedron. As $\overrightarrow{a_3} = -\overrightarrow{a_1} + \overrightarrow{a_2}$, a (hkl)

plane is equivalent to (hkil) under the Miller notation because the sum of the first three indices is necessarily zero $i = -h + k$, so the [*hkil*] direction is perpendicular to the (*hkil*) plane for some particular plane families.

In Figure 2.3 the main-planes of the wurtzite structure are shown. Each plane is described by a direction, in the case of the c-plane the direction is the (0001), for the m-plane the direction is the $(10\bar{1}0)$ and the a-plane is described by the $(11\bar{2}0)$ direction.

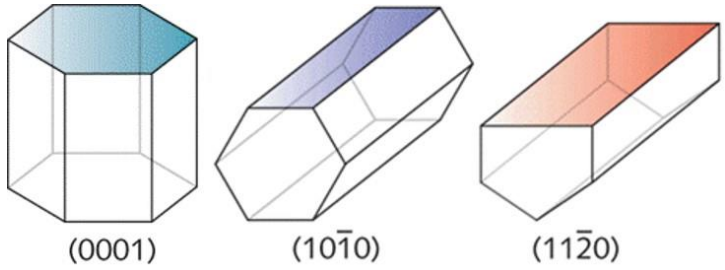

Figure 2.3. Representation of the c-plane (0001), m-plane $(10\bar{1}0)$ and a-plane $(11\bar{2}0)$ [Jeff10].

2.2. Elastic properties

The growth of III-nitrides on non-lattice-matched substrates and with different thermal expansion coefficients lead to heteroepitaxial growth, and induce strain in the grown layers.

Strain affects to optical and electrical properties and also to the band gap properties of III-nitrides.

The stress (σ_{ij}) of the material is related with the strain (ε_{kl}) by Hooke's Law through C_{ij} which is the elastic tensor of the material, see Eq. (2.3).

$$\sigma_{ij} = \sum C_{ij}\varepsilon_{kl} \tag{2.3}$$

In the case of materials with hexagonal symmetry, five of the six elastic coefficients are independent, and the equation (2.3) is as follows:

$$\begin{pmatrix} \sigma_{xx} \\ \sigma_{yy} \\ \sigma_{zz} \\ \sigma_{yz} \\ \sigma_{zx} \\ \sigma_{xy} \end{pmatrix} = \begin{pmatrix} C_{11} & C_{12} & C_{13} & 0 & 0 & 0 \\ C_{12} & C_{11} & C_{13} & 0 & 0 & 0 \\ C_{13} & C_{13} & C_{33} & 0 & 0 & 0 \\ 0 & 0 & 0 & C_{44} & 0 & 0 \\ 0 & 0 & 0 & 0 & C_{44} & 0 \\ 0 & 0 & 0 & 0 & 0 & \frac{C_{11}-C_{12}}{2} \end{pmatrix} \times \begin{pmatrix} \varepsilon_{xx} \\ \varepsilon_{yy} \\ \varepsilon_{zz} \\ \varepsilon_{yz} \\ \varepsilon_{zx} \\ \varepsilon_{xy} \end{pmatrix} \tag{2.4}$$

When the growth direction is along the [0001], the in-plane stress is uniform ($\sigma_{xx} = \sigma_{yy}$) and the stress along the growth direction is 0 ($\sigma_{zz} = 0$). So that the strain is zero in the directions $\varepsilon_{yz}, \varepsilon_{zx}, \varepsilon_{xy}$ and thus the elastic tensor matrix is simplified (Eq. (2.5)). The elastic tensor coefficients of III-nitride materials are summarized on Table 2.2.

$$\begin{pmatrix} \sigma_{xx} \\ \sigma_{yy} \\ 0 \end{pmatrix} = \begin{pmatrix} C_{11} & C_{12} & C_{13} \\ C_{12} & C_{11} & C_{13} \\ C_{13} & C_{13} & C_{33} \end{pmatrix} \times \begin{pmatrix} \varepsilon_{xx} \\ \varepsilon_{yy} \\ \varepsilon_{zz} \end{pmatrix} \tag{2.5}$$

Table 2.2. Elastic tensor coefficients [VuMe03] and piezoelectric coefficients [VuMR01] for the different III-nitride materials.

	C_{11} (GPa) [VuMe03]	**C_{12} (GPa)** [VuMe03]	**C_{13} (GPa)** [VuMe03]	**C_{33} (GPa)** [VuMe03]	**e_{31} (C/m^2)** [VuMR01]	**e_{33} (C/m^2)** [VuMR01]
AlN	396	137	108	373	-0.5	1.79
GaN	390	145	106	398	-0.35	1.27
InN	223	115	92	224	-0.57	0.97

For III-nitrides grown on substrates with different a lattice parameter than the nitride and with the [0001] direction as growth direction, strain along this direction (ε_{zz}) and in the perpendicular plane ($\varepsilon_{xx}, \varepsilon_{yy}$) are induced. The strain state in each direction is defined by the following equations:

$$\varepsilon_{zz} = \frac{c - c_0}{c_0} \tag{2.6}$$

$$\varepsilon_{xx} = \varepsilon_{yy} = \frac{a - a_0}{a_0} \tag{2.7}$$

The relationship between the in-plane and the out-plane deformation is through the elastic tensor as follows:

$$\varepsilon_{zz} = -\frac{2C_{13}}{C_{33}}\varepsilon_{xx} \tag{2.8}$$

2.3. Crystal polarization

The crystal polarization of III-nitrides is very important because it influences the optical and electrical properties of the material, specially in nitride based heterostructures.

The total crystal polarization (P_{tot}) is the sum of the spontaneous polarization (P_{sp}) and the piezoelectric polarization (P_{pz}). It induces a total internal electric field (E_{tot}) within the material, given by the Eq. (2.9).

$$E_{tot} = -\frac{P_{tot}}{\varepsilon_0 \varepsilon_r} \tag{2.9}$$

where ε_0 is the vacuum permittivity and ε_r is the dielectric constant of the material.

2.3.1. Spontaneous polarization

The intrinsic asymmetry of the wurtzite structure makes possible the spontaneous generation of a dipole oriented along the *c*-axis from the nitrogen atom to the metal atom. The resultant polarization field is known as spontaneous polarization. The deformation of the tetrahedron due to the electronegativity difference between the nitrogen (~3) and metal (~1.6—1.8) atoms that form the covalent bond also induces the spontaneous polarization. The higher electronegativity of the nitrogen atoms increases the attraction of the metal valence electrons by nitrogen atoms. Also, this lack of symmetry, makes the [0001] and the [0001] directions not equivalent.

There are two different polarities as a function of the atoms that are present at the top of the nitrogen-metal bilayer, see Figure 2.4:

- The metal polarity (Ga-, Al-, In-face) in which the top of the bilayer is composed by metal atoms, in this case the P_{sp} vector points to the substrate.
- The nitrogen polarity (N-face) in which the top of the bilayer is formed by nitrogen atoms. In this case the P_{sp} vector points to the layer surface.

The P_{sp} affect the surface properties and it should be considered that structures with different polarities are not equivalent as they can present differences in physical and chemical properties.

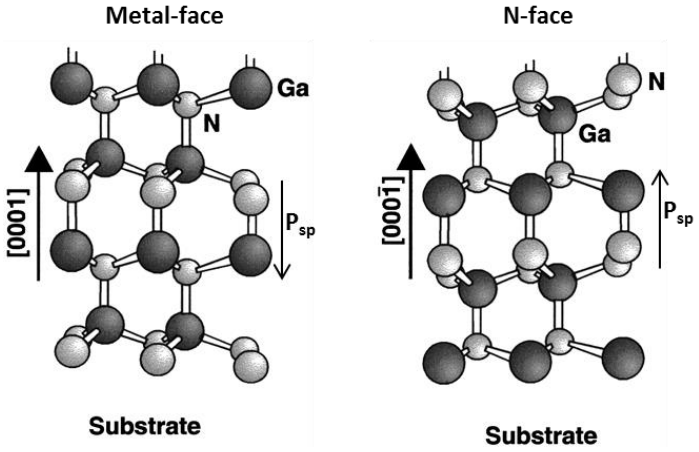

Figure 2.4. Wurtzite polarities: (left) metal-polarity and (right) N-polarity [Amba98].

In a wurtzite system, three types of crystal planes can be distinguished. The {0001} planes or *c*-plane are commonly referred to as polar plane that can be metal- or nitrogen-polar. The other planes are perpendicular to the (0001) plane and are called non-polar planes, these ones are the {1120} or *a*-plane and the {1010} or *m*-plane. The planes involving some component along the [0001] direction are the semipolar ones (see Figure 2.3).

The higher is the deviation from the ideal wurtzite structure of the nitride material, the higher spontaneous polarization has that material. This relationship is shown in Table 2.1, where it is seen that AlN presents the highest P_{sp} and also the highest deviation from ideality. The P_{sp} of ternary compounds is related with its composition in a first approximation by the Vegard's law [BeFi99, Vega21].

2.3.2. Piezoelectric polarization

The piezoelectric polarization effect appears when the layers suffer from mechanical stress, and thus, the atomic positions of the crystal are modified leading to a different spatial distribution of charges.

As it has been presented before, the thermal expansion coefficients and the lattice constants of III-nitrides makes impossible its homoepitaxial growth due to the lack of lattice-matched substrates. So III-nitrides are grown heteroepitaxially on different substrates, this heteroepitaxial growth is associated with strain (ε_{ij}) in the layers and thus with the piezoelectric polarization by the following equation:

$$P_{pz} = \begin{pmatrix} 0 & 0 & 0 & 0 & e_{15} & 0 \\ 0 & 0 & 0 & e_{15} & 0 & 0 \\ e_{31} & e_{31} & e_{33} & 0 & 0 & 0 \end{pmatrix} \times \begin{pmatrix} \varepsilon_{xx} \\ \varepsilon_{yy} \\ \varepsilon_{zz} \\ \varepsilon_{yz} \\ \varepsilon_{zx} \\ \varepsilon_{xy} \end{pmatrix} \tag{2.10}$$

where e_{ij} are the piezoelectric coefficients. Due to the symmetry of the wurtzite crystals, only three piezoelectric constants are considered: e_{15}, e_{31}, e_{33}.

It is possible to relate the piezoelectric polarization along the [0001] ($\mathrm{P_{pz}^{Z}}$) with the elastic properties of the material (Eq. (2.11)) by combining Eqs. (2.8) and (2.10), and knowing that the piezoelectric polarization along the (0001) plane is null $P_{pz}^{X} = P_{pz}^{Y} = 0$.

$$P_{pz}^{Z} = 2\frac{a - a_0}{a_0}\left(e_{31} - e_{33}\frac{C_{13}}{C_{33}}\right) \tag{2.11}$$

Table 2.2 shows that for all III-nitrides $\left(e_{31} - e_{33}\frac{C_{13}}{C_{33}}\right) < 0$. This means that the piezoelectric polarization along the [0001] direction is positive if the material is under compressive strain ($a<a_0$) and negative when it is under tensile strain ($a>a_0$).

2.4. Optical properties

III-nitrides (AlN, GaN, InN and their alloys) present a direct band gap, this mean that the maximum of the valence band and the minimum of the conduction band are centered at the Brillouin zone. In this case, the direct band-to-band absorption

and emission processes take place just involving photons with energies higher than that of the band gap.

The dependence of the band gap energy with the temperature is described by the Varshni's equation (Eq. (2.12)) [Vars67], the lattice thermal expansion and electron-photon interaction induces a change in the band structure of the semiconductors which is related with a change in the band gap energy with the temperature.

$$E_g\ T\ = E_g\ 0\ - \frac{\gamma T^2}{\beta + T} \tag{2.12}$$

The Varshni's equation gives information of the optical parameters that are related with the band gap, such as the band gap energy at 0 K ($E_g(0)$), γ which is a constant and β that is a parameter associated with the Debye temperature of the crystal.

Table 2.3 summarizes the commonly accepted band gap energy values at low $E_g(0)$ and at room temperature $E_g(300)$ and the Varshni constants of high crystal quality III-nitride binary compounds grown by MBE.

Table 2.3. Commonly accepted band gap energy values of III-nitride binary compounds at low and room temperature and Varshni constants of the binary compounds [VuMe03].

	$E_g(0)$ (eV) [VuMe03]	**$E_g(300)$ (eV)** [VuMe03]	**γ (meV/K)** [VuMe03]	**β (K)** [VuMe03]
AlN	6.25	6.14	1.799	1462
GaN	3.51	3.43	0.909	830
InN	0.69	0.64	0.245	624

In the case of ternary alloys, they allow the work in a wide spectral range, because the band gap energy of these compounds can be tuned by changing the composition of the alloy. These alloys ($Al_xIn_{1-x}N$, InGaN, AlGaN) make possible the development of devices working in the range of 200 nm to 1900 nm by changing the metal content. In the particular case of $Al_xIn_{1-x}N$, the band gap energy can be tuned from the ultraviolet of AlN to the near infrared of InN.

The band gap energy of the ternary alloys ($A_xB_{1-x}N$) is related with the composition and the band gap energy of the binary compounds that form it by a modification of the Vegard's Law [Vega21], that takes into account a deviation from the linearity [LiYK04]. This relationship is a quadratic polynomial equation with a nonlinear coefficient known as bowing parameter (b), see Eq. (2.13).

$$E_{g_{A_xB_{1-x}N}} = xE_{g_{AN}} + \ 1-x \ E_{g_{BN}} - bx(1-x) \tag{2.13}$$

The bowing parameter of the $Al_xIn_{1-x}N$ alloy ranges from ~ 3 to ~20 eV [SCTP13] for $Al_xIn_{1-x}N$ layers grown by MOCVD with different layer compositions, it increases when decreasing the In composition. For layers grown by MBE with similar compositions as the ones used in this Thesis, the calculated bowing parameter is of 4.96 eV [TCIY06].

2.4.1. Burstein-Moss Effect

The InN semiconductor has been intensively under study in the last decade because there were some inconsistencies in the different reported values of the band gap energy. At the beginning, the band gap energy of the InN was reported to be of 1.9 eV [TaFo86], this value was achieved in a InN layer grown by RF sputtering on glass substrates, the layer presented polycrystalline structure and a residual carrier concentration above 10^{19} cm^{-3}.

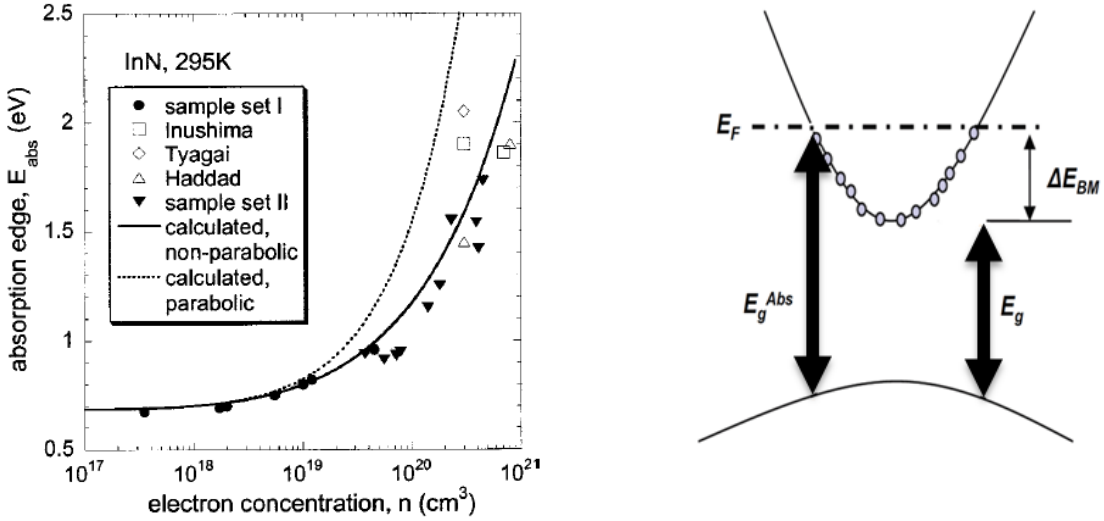

Figure 2.5. Left: Band gap energy of InN layers as a function of the carrier concentration [WWLA04]. Right: Band filling due to high carrier concentration.

However, in the 2000 different groups presented very different band gap energies for InN grown mostly by MBE and with carrier concentrations in the range of 10^{16} cm^{-3}, these band gap energies were in the range of 0.65-0.9 eV [DKSE02, SHKY02, WWYA02]. For layers deposited by sputtering that present high carrier concentration (10^{20}-10^{21} cm^{-3}) the band gap energy is in the range of 1.6-1.9 eV [GSNO98, VIMG12]. The difference between all the band gap values of InN may be attributed to the crystalline quality and the carrier concentration of the InN layers. Figure 2.5 left shows the band gap energy of InN layers as a function of the carrier concentration extracted from [WWLA04].

The high carrier concentration induces the band filling and thus a blue shift of the band gap (see Figure 2.5 right), this is known as Burstein-Moss effect, and is one of the most common accepted reasons for explaining the high band gap energy of the InN layers grown by sputtering. This carrier concentration can be related to impurities, mainly oxygen, hydrogen and carbon. The incorporation of these impurities to the layers increases due to the polycrystalline nature of the sputtering layers, where they can be located in the grain boundaries easily.

Chapter 3

Growth of III-Nitrides by sputtering

There are different growth techniques available for the deposition of thin films. These techniques are mainly classified in four groups depending on the type of the involved process [Sesh02]:

- Evaporative processes such as molecular beam epitaxy (MBE).
- Glow-discharge as in sputtering.
- Gas-phase chemical processes as in chemical vapor deposition (CVD).
- Liquid-phase chemical processes.

During the development of this Thesis, Al, InN, AlN and $Al_xIn_{1-x}N$ thin films have been deposited by sputtering. Thus, a general view of this method for the deposition of III-nitrides is given in this section.

3.1. Sputtering technique

Sputtering is a commonly used technique for thin film deposition of metals, insulating materials and semiconductors. It is also used for etching process and for surface cleaning. Sputtering is a low cost technique in terms of equipment and

maintenance, it also allows the deposition of thin films in a wide range of temperatures (even at room temperature), and on both rigid and flexible substrates.

3.1.1. Principles of sputtering

In the sputtering technique, the atoms of a gas are ionized by the application of a (radiofrequency or DC) voltage and a plasma is formed. The ionized atoms of the plasma are accelerated into the surface of a target in order to discharge atoms from it; this is achieved due to the transference of kinetic momentum. These ejected or sputtered atoms can then be condensed under the right deposition conditions onto a substrate to nucleate a thin film of that material. The bombardment of the target by the plasma ions produces the pulverization of the target and also the emission of energetic secondary electrons, which are accelerated towards the plasma enabling the maintenance of the plasma discharge. This process takes place in a high vacuum deposition chamber with a base pressure of 10^{-7} mBar in order to minimize the amount of impurities in the grown films. A scheme of the sputtering process can be seen in Figure 3.1.

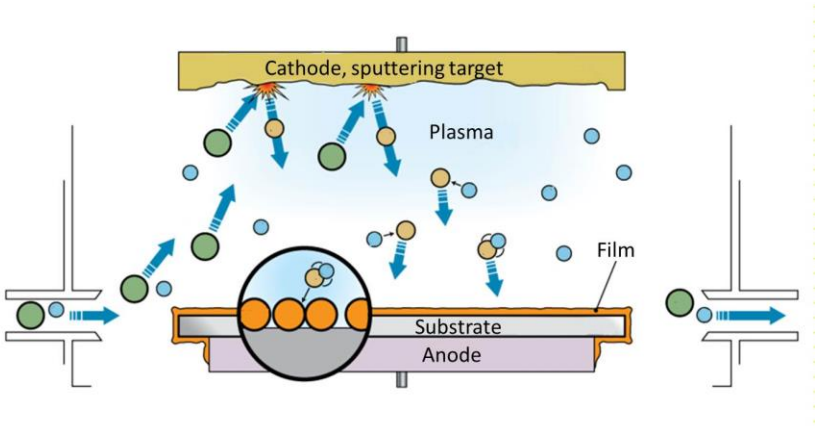

Figure 3.1. Scheme of the bombardment process in a sputtering technique, modified from [Inc00]. Blue circles represent electrons. Green and yellow circles represent ions of gas environment and target constituents, respectively.

The efficiency of the sputtering process is defined by the sputtering yield, which is the average number of atoms ejected from the target per incident ion. It depends on the angle, energy and mass of the incident ion and on the surface binding energy

of atoms in the target. Three effects can be produced as a function of the energy of the incident ions:

- If the positive ions reach the surface of the target with an energy higher than the surface binding energy, the atoms of the target can be ejected and then travel to the substrate to create the film.
- If the energy of the ions is too low, they can be reflected, produce surface damage and surface migration.
- If ions reach the surface of the target with too high energy, ion implantation can occur.

Another important parameter is the mean free path, which is the average distance traveled by a moving particle (such as an atom, a molecule, a photon) within a gas between successive impacts which modify its direction or energy. The mean free path is inversely proportional to the sputtering pressure, so it has to be optimized in order to maximize the mean free path.

3.1.2. Sputtering types

In this section the different types of sputtering will be described. There are different classifications of the sputtering process as a function of the way of generating the plasma, type of cathode and type of gas.

3.1.2.1. Plasma generation

The plasma can be generated under two different conditions in terms of the voltage applied to the cathode: static (DC) and alternating, radiofrequency (RF).

3.1.2.1.1. DC voltage

In the case of applying a DC voltage to generate the plasma, it is necessary to have conductive electrodes in order to sustain a DC glow discharge. The electrodes are placed in a low pressure gas, one of the electrodes is placed in contact with the material that is going to be evaporated (cathode) and the other is placed in contact with the substrate (anode). The DC plasma allows high deposition rates but requires the use of conductive materials in the cathode in order to avoid the accumulation of positive charges in the electrode.

In order to generate the plasma, the pressure has to be within a specific range in the sputtering chamber and a high DC voltage has to be applied in the electrodes, so that the ionization of the gas is possible. In this way, the high intensity of the electric field in the vicinity of the cathode makes possible the ejection of atoms from the cathode.

3.1.2.1.2. RF voltage

For solving the problems related to the use of non-conductive cathodes, it is necessary to apply an alternating voltage between the electrodes, so that each electrode acts alternately as the cathode and the anode. During negative cycle the positive charges are accumulated in the target while during the positive cycle these charges are compensated by incident electrons. During the negative cycle the ions sputter the target surface and the atoms of it are ejected making possible the formation of the layer over the substrate (see Figure 3.2). The frequency used is typically in the radio frequency range (13.56 MHz).

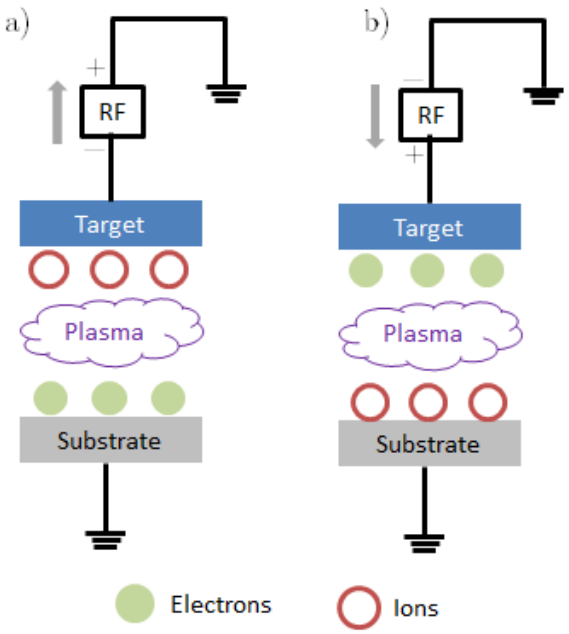

Figure 3.2. a) Negative and b) positive cycles of RF sputtering process.

RF plasma allows the deposition of non-conductive and isolating materials. However, at the same driving power, lower deposition rates are achieved in comparison with the DC voltage (about half of it).

3.1.2.2. Type of cathode

Another way of classifying the sputtering process is as a function of the cathode, there are three types of cathodes: planar diode, magnetron and unbalanced magnetron.

3.1.2.2.1. Planar diode

In this configuration, the two electrodes (anode and cathode) in which the glow discharge is applied are located inside a vacuum system and are separated a certain distance. Under the right conditions, appropriate voltage and gas pressure, the gas will break down into a plasma discharge. Near the cathode there is a space that present a very large electric field in which ions are accelerated across it and they impact the surface of the cathode.

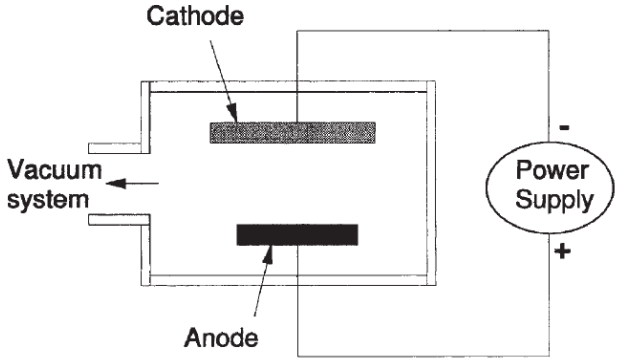

Figure 3.3. Planar diode configuration [Sesh02].

High pressures, in the range of low Torr to high mTorr (normally ~3 Pa), are needed since the plasma remains active thanks to the electron multiplication.

This type of sputtering was used to erode surfaces and for sputter deposition, but its application is limited due to the low deposition rate and the difficulty of sputtering isolating targets.

3.1.2.2.2. Magnetron

Magnetron sputtering deposition takes advantage of a magnetic field to trap electrons, enhancing the efficiency of the initial ionization process and allowing the generation of the plasma at lower pressures which reduces both background gas

incorporation in the growing film and energy loses in the sputtered atom through gas collisions.

For generating the magnetic field, permanent magnets are located between the power supply and the target. The magnetic field is ring-shaped and parallel to the target surface, so that the electrons are effectively confined near the target. The electrons of the plasma and the secondary electrons of the target follow helical paths around the magnetic field due to the Lorentz's force generated between the electric and magnetic fields (see Figure 3.4). The plasma ions, due to their higher mass are not affected by the magnetic field. The confinement of the electrons increases the probability of ionize neutral atoms of the gas that are near the target increasing the density of the plasma. So that is possible to reduce the gas pressure of the chamber and therefore, increase the growth rate (G_R) which is defined as the ratio between the thickness of the layer and the sputtering time. The confinement of the plasma near the target causes erosion tracks in the target's surface.

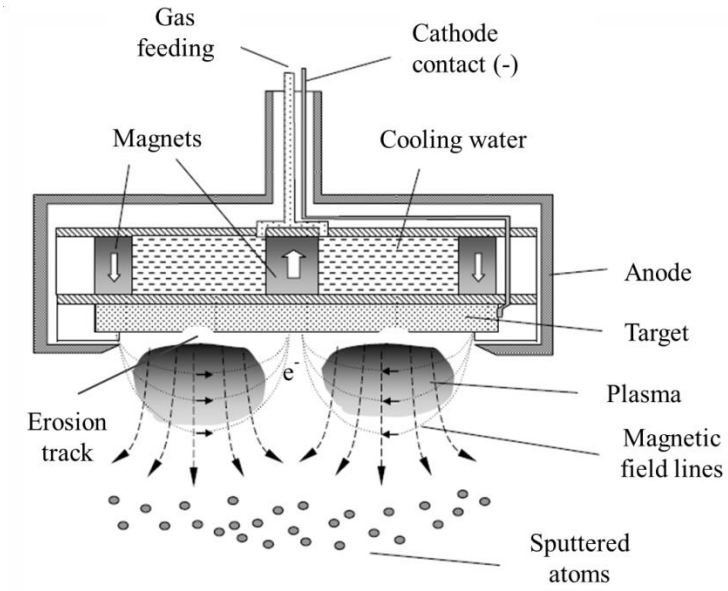

Figure 3.4. Planar sputtering magnetron scheme [Albe03].

The advantages of the magnetron sputtering compared to planar diode are its higher ionization efficiency, lower power discharge, plasma confinement in the target area and the possibility of working at lower pressures, in the range of ~0.1 Pa, leading to higher deposition rates.

The RF voltage is normally used with magnetrons because it is important to confine the movement of the secondary electrons so that the RF glow discharge is maintained.

3.1.2.2.3. Unbalanced magnetron

The difference between the balanced and unbalanced magnetron sputtering is that in the first case all the magnets have the same strength but in the unbalanced magnetron sputtering, the inner magnetron is weakened. In this case, not all the field lines are closed between the central and outer poles in the magnetron. Some are directed towards the substrate allowing some secondary electrons follow these field lines (see Figure 3.5). Consequently, the plasma is no longer strongly confined to the target region, but is also allowed to flow out towards the substrate.

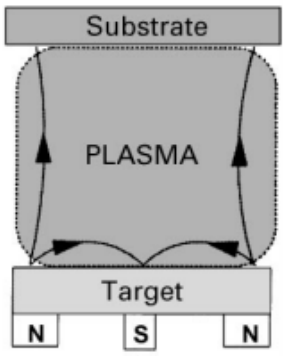

Figure 3.5. Unbalanced magnetron sputtering scheme [KeAr00].

3.1.2.3. Type of gas

Another classification of the sputtering system is as a function of the gas used to generate the plasma, this gas can be reactive or non-reactive.

3.1.2.3.1. Non-reactive gas

In this type of sputtering, the gas used for generating the plasma and for sputtering the target surface is a gas that does not react with the atoms of the target during the growth of the film.

Usually the gas that is used for non-reactive sputtering is a noble gas with high atomic mass, achieving high growth rates due to the enhancement of the

transference of the kinetic momentum to the target atoms. The gas that is mostly used is argon due to its low cost.

3.1.2.3.2. Reactive gas

Nitrogen, oxygen and methane are typical reactive gases; these gases can react with the atoms of the target so that a compound is formed. This compound can be formed on the target surface, in-flight during the trip between the target and the substrate or on the substrate depending on the deposition conditions.

In this type of sputtering it has to be taken into account the possibility of target poisoning, this occurs when the atoms in the target surface react with atoms of the plasma and a thin film of the compound is formed in the target surface, this reduces the sputtering growth rate, so for increasing it is needed more reactive gas. The increase of the reactive gas results in a higher poisoning of the target leading to a positive feedback loop.

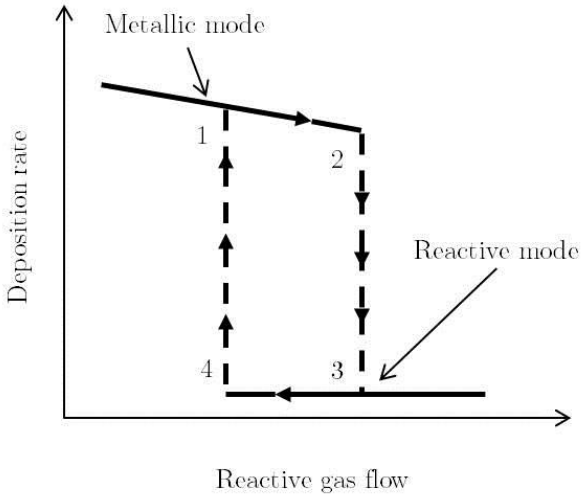

Figure 3.6. Hysteresis process in reactive sputtering.

This positive feedback is seen as a target hysteresis based on sudden changes in the thin film deposition rate as it can be observed in

Figure 3.6. When the reactive gas flow is low, the growth rate is similar to the metallic growth rate and there is not enough gas for reaching stoichiometric compounds. In order to prevent the metallic mode, the reactive gas flow has to be increased (from 1 to 2), the reactive mode begins in this part. This reactive mode is accompanied by a decrease of the growth rate (3) due to the poisoning of the target

while the compound is formed and deposited into the substrate. To reduce the target poisoning, the reactive gas flow has to be reduced (4) so that no more compound can be formed. In this case, the target poisoning disappears and the deposition rate increases drastically beginning again with the metallic mode. The increase in the gas flow is related with an increase in the chamber pressure.

3.1.3. Magnetron sputtering equipment used in this Thesis

All the samples studied in this Thesis were grown in a sputtering system ATC ORION-3-HV from AJA International, this machine is placed in the Electronics department facilities from the University of Alcalá (see Figure 3.7).

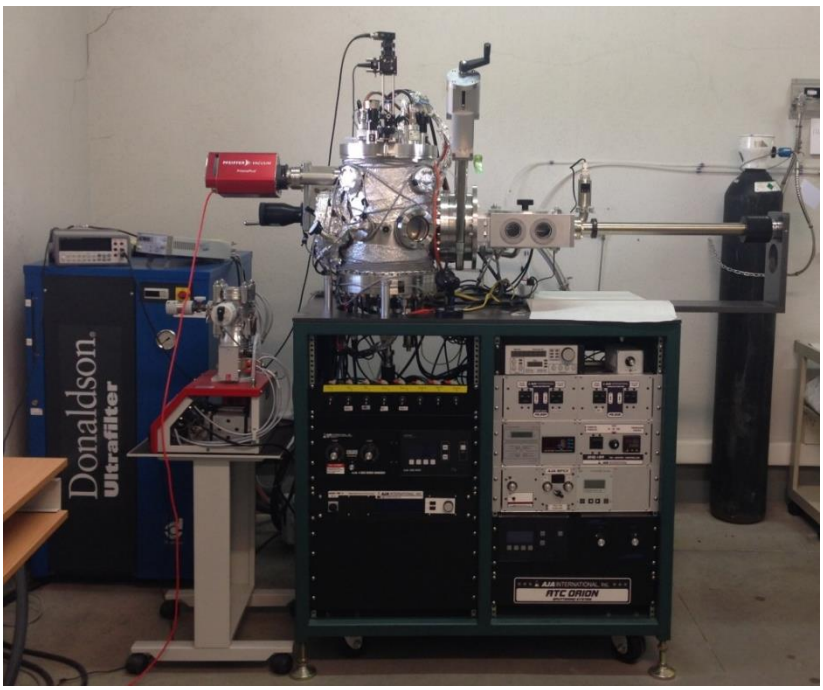

Figure 3.7. Magnetron sputtering system used in this work together with the gas installation in the GRIFO facilities at the University of Alcalá.

This system presents a planar magnetron configuration; the main parts of it are described below:

- High-vacuum manual valve for controlling the pressure in the chamber.

- Pump system formed by a turbomolecular pump (up to 210 l/s) and a mechanical pump (up to 12 m^3/h). The base pressure that can be achieved is of ~10^{-8} mBar.

- Three vacuum gauges for controlling the vacuum pressure in the chamber depending on the pressure range: an ionization gauge for low-base pressures (~10^{-8} mBar), a baratron gauge for pressures in the deposition range (~10^{-4} – 10^{0} mBar) and a convectron gauge for measuring pressures close to atmosphere pressure.

- Gas sources: Ar (5N) and N_2 (6N).

- Mass-flow controllers to control the flow of the gases introduced into the sputtering chamber.

- Variable leak valve for chamber venting with nitrogen.

- Three 2-inch diameter confocal magnetron cathodes with integrated shutters.

- Metal targets: Al (5N) and In (4N5).

- Two RF power sources (up to 300 W) with impedance matching unit and a DC power supply (up to 750 W).

- A 4-inch substrate holder with automatic rotatory system for optimized heating and thin film deposition homogeneity.

- Manually adjustable working distance between the substrate and target. It has been fixed at 10.5 cm.

- Two quartz lamps placed under the substrate holder to heat the substrates up to 850°C.

- One K-type thermocouple placed 2 mm below the substrate holder and controlled by a PID with a resolution of ± 1°C for monitoring the substrate temperature during the deposition process.

- Closed-cycled cooling system for keeping cool the magnetrons and the substrate heater.

- Thin film deposition monitor based in a quartz crystal for measuring the deposited metal thickness.
- Introduction chamber equipped with a turbomolecular pump and a mechanical pump.
- Residual gas analyzer for measuring the residual gases of the chamber.
- Reflectivity system for *in situ* measurement of the reflectivity of the deposited layers during growth.

The growth of InN, $Al_xIn_{1-x}N$ and AlN layers studied during this Thesis were grown using radio-frequency reactive magnetron sputtering. In the case of metal layers, the DC power with non-reactive gas has been used.

3.2. Substrates

As there are no appropriate lattice-matched and thermally-stable substrates for growing III-nitrides in a homoepitaxial growth, the growth of III-nitrides has to be in a heteroepitaxial mode. The mainly used substrates are sapphire (Al_2O_3), silicon (Si), silicon carbide (SiC) and also although they are less used gallium arsenide (GaAs), zinc oxide (ZnO). For choosing the best substrate, it has to be taken into account the lattice and thermal expansion mismatches between layer and substrate. Furthermore, the desired crystal orientation, defect density, surface morphology and substrate cost will depend on the further material application.

In this work, three types of substrates are used: sapphire, p-doped Si (111) and glass.

3.2.1. Sapphire

Sapphire substrates are used for applications in which a transparent substrate is need. It is a relatively low cost substrate which is commercialized in different sizes and crystal orientations. An advantage of sapphire substrates is its high thermal stability at high temperatures. Sapphire can be grown with high crystalline quality, it crystallizes in a hexagonal structure, its lattice parameters (c = 12.99 Å and a = 4.76 Å) are quite higher than those of the III-nitrides.

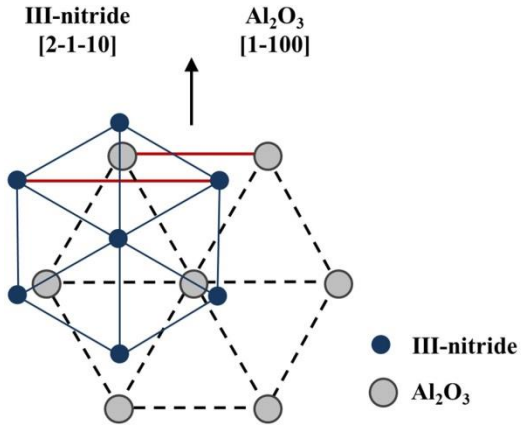

Figure 3.8. Scheme of the epitaxial relationship between III-nitrides and sapphire in (0001) plane [Mont15].

As it is schemed in Figure 3.8, when III-nitrides grow on sapphire, the nitride crystal structure is rotated 30° with respect to the sapphire one. Then, [2110] nitride direction and [1100] sapphire direction are aligned. This rotation leads to an effective lattice parameter of III-nitride when growing on sapphire. This effective lattice parameter is given by the following equation:

$$a'_{III-nitride} = \sqrt{3} a_{III-nitride} \tag{3.1}$$

Table 3.1. Lattice parameters of III-nitrides [VuMe03] and substrates (a). Thermal expansion coefficients (α_a) of nitrides and substrates [NeEk96]. Lattice and thermal mismatch between AlN, GaN and InN and Si (111) and sapphire substrates at 300 K. Δa_{epi} and $\Delta\alpha_{epi}$ is the difference between lattice parameters and the thermal coefficient of the layer and the substrate.

	a (Å)	a' (Å)	$\frac{\Delta a'_{epi}}{a_{sapp}}$ (%)	$\frac{\Delta a_{epi}}{a_{Si(111)}}$ (%)	α_a (10^{-6} K^{-1})	$\frac{\Delta\alpha_{epi}}{\alpha_{sapp}}$ (%)	$\frac{\Delta\alpha_{epi}}{\alpha_{Si(111)}}$ (%)
AlN	3.112	5.390	13.3	-19.0	4.2	-44	17
GaN	3.189	5.524	16.1	-17.0	5.59	-25.5	55.7
InN	3.545	6.14	29.0	-7.7	3.83*	-48.9	6.7
Si (111)	3.840				3.59		
Sapphire	4.758				7.5		

*Value extracted from [WaRe01]

Table 3.1 summarizes the lattice parameters, thermal expansion coefficient and lattice and thermal mismatch between Si (111) and sapphire substrates with the III-nitrides. It shows that III-nitrides grow under tensile strain on Si (111) substrates and under compressive strain when growing on sapphire substrates.

Sapphire substrates have been grown by Czochralski method and supplied by Semiconductor Wafer, INC (see Figure 3.9 left). The sapphire substrate consists of ~500 ± 25-µm-thick double side polished [0001]-oriented Al_2O_3 wafers with 3-inch diameter. A typical AFM measurement of the sapphire substrate is shown in Figure 3.9 right. The RMS surface roughness of sapphire is ~0.3 nm.

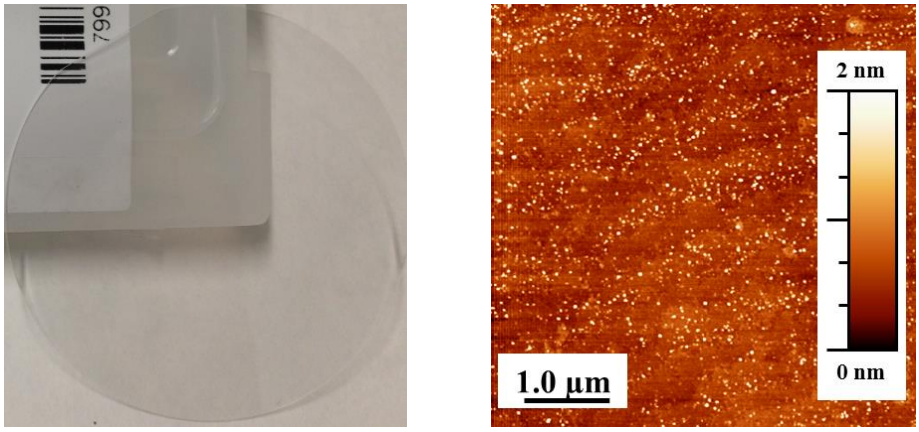

Figure 3.9. Left: Photo of a sapphire substrate. Right: AFM image of the sapphire substrate used in this work.

3.2.2. Silicon (111)

Silicon (Si) is a low cost material which can be obtained with a high crystalline quality. Since the actual technology is based on silicon devices, high dimension wafers are available in the market. Furthermore, growing III-nitrides on Si hold some additional advantages as: integration into the existent technology, possibility of having n-type and p-type conductor substrates, easy cleavage and thermal stability.

Cubic silicon presents hexagonal symmetry within the plane perpendicular to the [111] direction, allowing the growth of wurtzite nitrides. The epitaxial relationship between nitrides and Si (111) comprises the alignment of the [0001] direction of the III-nitride compound and the [111] of the Si.

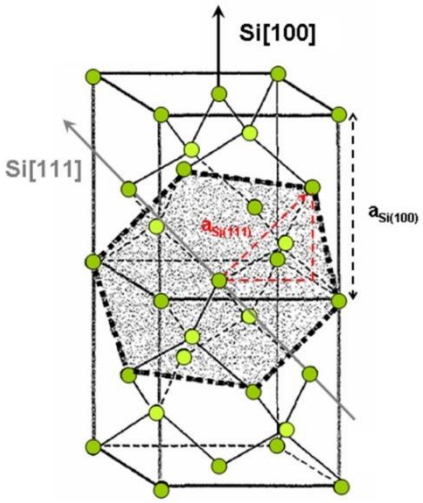

Figure 3.10. Relationship between (100) cubic plane and (111) hexagonal plane of silicon. The red-dashed triangle shows the relationship between silicon cubic and hexagonal phases [Vald11].

Figure 3.10 shows the relation between (100) cubic plane and (111) hexagonal plane of Si. Particularly, the red-dashed triangle shows the lattice parameters relationship which should be considered for the growth of hexagonal nitrides on Si (111). The relationship is given by:

$$a_{Si(111)} = \frac{a_{Si(100)}}{\sqrt{2}} \tag{3.2}$$

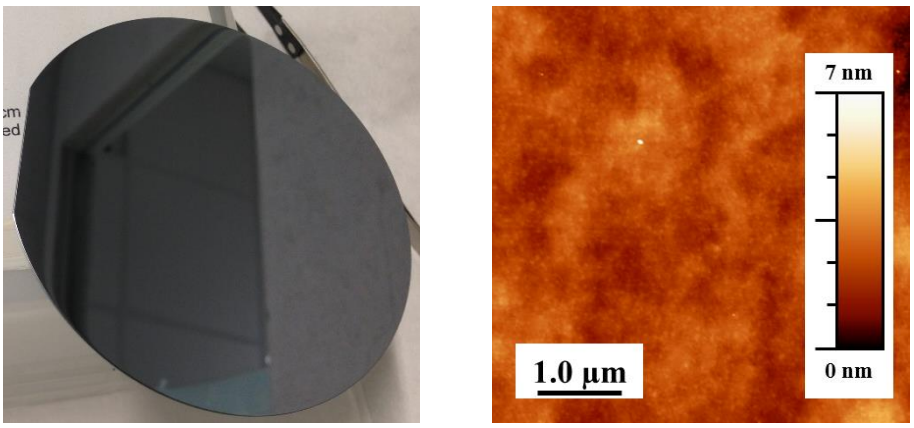

Figure 3.11. Left: Photo of a p-silicon (111) substrate. Right: AFM image of the p-silicon (111) substrate used in this work.

p-type silicon (111) substrates have been supplied by Semiconductor Wafer, INC (see Figure 3.11 left). The dopant of these wafers is B; they are 4-inch diameter,

double side polished ~525 ± 52-µm-thick wafers. Its resistivity is of 1—100 Ωcm. Figure 3.11 right shows the typical AFM image of the p-silicon (111). The RMS surface roughness of the p-Si (111) substrate is of ~0.5 nm.

3.2.3. Glass

For studying the growth of III-nitrides on amorphous substrates, glass substrates were used. The glass substrates were provided by DELTALAB (see Figure 3.12 left), and are double side polished squared substrates of 2.2×2.2 cm, the thickness of these substrates is of ~0.15 ± 0.02 mm. The RMS surface roughness of the glass substrate is of ~2 nm, the AFM image is shown in Figure 3.12 right.

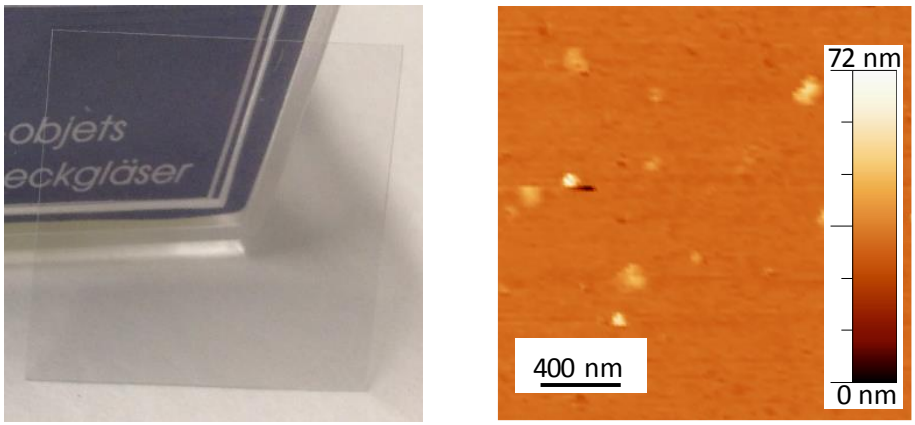

Figure 3.12. Left: Photo of a glass substrate. Right: AFM image of the glass substrate used in this work.

It also gives an idea of the growth of III-nitrides on optical fibers which will be used in Chapter 8.

Chapter 4

Characterization techniques

In this Chapter the experimental techniques used for characterizing the III-nitride layers are described. Structural, morphological, chemical, electrical and optical properties of the developed materials are studied. For the structural and chemical properties, high-resolution X-ray diffraction (HRXRD), wavelength dispersive X-ray (WDX) and X-ray photoelectron spectroscopy (XPS) measurements are used. At the same time, for the morphological properties atomic force microscopy (AFM) and field emission scanning electron microscopy (FESEM) are used. Meanwhile, the electrical properties of the layers are measured by Hall effect measurements. Finally, the layer optical characterization is focused on linear optical experiments consisting of transmittance (Tr), reflectance (R) and photoluminescence (PL) measurements.

All these measurements have been possible thanks to the collaboration with other institutions.

4.1. Structural, chemical and morphological properties

Structural characterization techniques provide information about the structure and crystalline quality of the layers and they can also bring understanding of surface morphology, interface quality and film density.

4.1.1. High Resolution X-Ray Diffraction (HRXRD)

HRXRD has been widely used to assess the crystalline quality of the samples, to verify their crystalline orientation and to determine the lattice parameters. It is based on the principle of interference between electromagnetic waves. In order to get information about a material with this technique, the material should have a periodic structure and the incident wavelength of the probe waves have to be similar to the structure period.

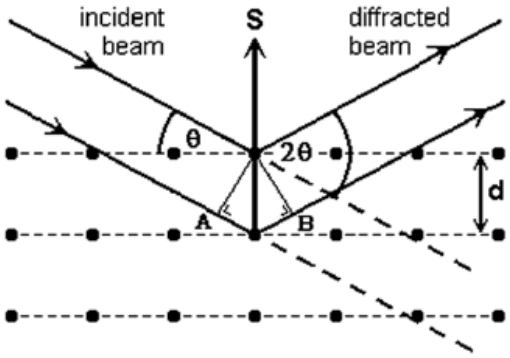

Figure 4.1. Bragg's reflection corresponding to three consecutive planes separated a distance d_{hkl} [MoVi09].

In the case of semiconductors, the X-ray wavelength is in the same range of the typical interatomic distance it being in the range of angstroms (typically, from 1 Å to 100 Å). Figure 4.1 depicts the diffraction effect produced when X-radiation beams of a wavelength λ, interfere with a periodic structure with parallel and equidistant atomic planes separated a distance λ. When a constructive interference between the X-ray beams and the structure occurs, and the Bragg's law given by Eq. (4.1) is fulfilled, the diffraction peak is obtained.

$$2d\text{sen}\theta = n\lambda \tag{4.1}$$

where d is the distance between two consecutive atomic planes, θ is the angle between the incident beam and the planes diffracting it, n is an integer called the diffraction order and λ is the radiation wavelength.

During the development of this Thesis, the X-ray diffraction measurements used are based on the registration of X-ray intensity reflected from the material under study depending on the angles of the incident (ω) and diffracted beams (2θ).

In this study two types of diffractograms under symmetrical configuration (when the angle formed between the detector and the sample is equal to the one formed between the incident beam and the sample) were performed: 2θ/ω-scan and ω-scan (rocking curve). And one in asymmetrical configuration (when the angle between the detector and the sample is different from the one formed by the incident beam and the sample): X-ray reflectivity.

- **2θ/ω-scan:** In this configuration, the X-ray source remains fixed and when the sample rotates an angle ω the detector rotates twice compared to the sample movement, 2θ (see Figure 4.2). The peak position will give the d-spacing for the Bragg peak, this will provide information about changes in the out-of-plane lattice parameter (c) of the unit cell, which is related to composition or strain/relaxation. The intensity of the peaks is proportional to the volume of diffracting material.

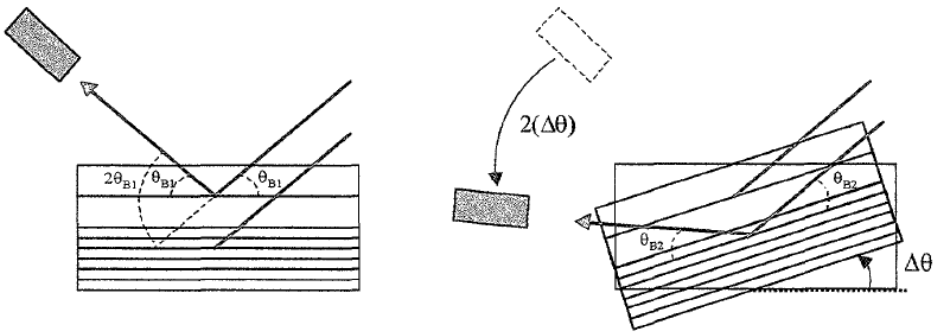

Figure 4.2. Schematic representation of the 2θ/ω-scan [Sánc00].

- **ω-scan (rocking curve):** In this scan, both the X-ray source and the detector are kept fixed in the given diffraction peak position and the sample rotates around the Bragg's condition angle. Figure 4.3 shows a scheme of the rocking curve scan. A perfect single crystal produces a very sharp peak, observed only when the diffraction condition is fulfilled. In this case, the rocking curve measurement presents a minimum FWHM due just to the instrument broadening and the intrinsic width of the crystal material. Larger broadening of the rocking curve of a material can be due to different

contributions like tilt (angular grain inclination with respect to the substrate while keeping the same in-plane lattice parameter, a) and strain surrounding dislocations. The FWHM of the rocking curve of the diffraction beam provides information about the degree of misorientation of the grains in the material and, therefore, its structural quality.

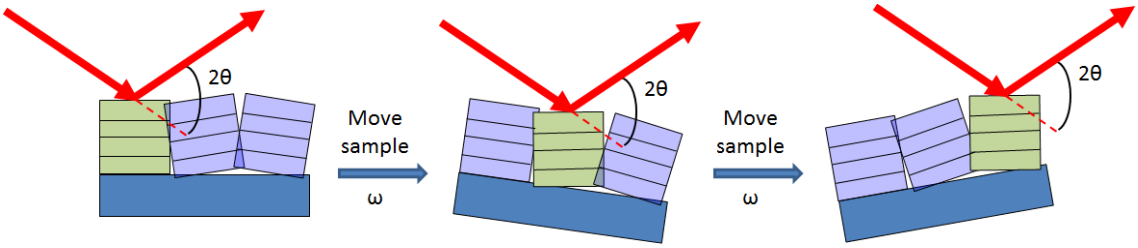

Figure 4.3. Scheme of the rocking curve diffraction measurement, the grains in green color are the grains that produce the diffraction of the X-rays.

- **X-ray reflectivity (XRR):** In this scan, the X-ray source and the sample form an angle that is significantly lower than the first Bragg diffracted and the detector moves 2θ. The material is considered a continuous medium with a certain density. At every interface a portion of X-rays is reflected and the interference of the partially reflected X-rays create a reflectometry pattern. Is a widely-used technique for characterizing layer thickness of thin films and multilayers, surface and interface roughness, surface density gradients and layer density. In this study, XRR measurements were carried out for estimating the thickness and the density of the thin AlN layers grown on p-Si (111). The film thickness has been obtained through the spacing between maximums of the reflectivity together with the Bragg's equation.

The HRXRD measurements allow the estimation of the composition of ternary alloys. In the case of symmetric measurements is done assuming fully relaxed layers and using the Vegard's law [Vega21] which takes into account the c lattice parameter of the binary compounds that form the ternary compound, in the particular case of $Al_xIn_{1-x}N$ the lattice parameters that have been used are InN ($c_{InN} = 5.703$ Å) and AlN ($c_{AlN} = 4.982$ Å) [VuMe03] (see Eq. (2.2)). A more accurate estimation of the composition by HRXRD measurements requires the use of asymmetric measurements where it is possible to measure separately the strain and composition effect.

It is also possible the estimation of the average grain size (G) of the layers by applying the Scherrer formula for spherical particles [Patt39]:

$$G = \frac{0.9\lambda}{\Delta 2\theta} cos\theta \tag{4.2}$$

Figure 4.4. Diffractometers used during this work. Left: Bruker D8-4C Advance located at the X-ray Diffraction Techniques Laboratory at the ICMM-CSIC in Madrid. Right: X'Pert Pro MRD located at the CAI X-ray Diffraction service of the Complutense University.

HRXRD analysis was performed at the X-ray Diffraction Techniques Laboratory at the ICMM-CSIC in Madrid under the supervision of Dr. Ana Ruiz by using a Bruker D8-4C Advance system and at the CAI X-ray Diffraction Service of the Complutense University by using a PANalytical X'Pert Pro MRD system (see Figure 4.4).

These diffractometers are based on 3-axis (x, y, z) and 4-circles (2θ, ω, φ, χ) movements. The X-rays are generated by bombarding a Cu target with electrons in an evacuated tube. The primary beam coming from the X-ray tube is divergent and polychromatic with wavelengths corresponding to the Cu $K\alpha_{1,2}$ and Cu $K\beta$ emission lines. The beam is collimated using a Göbel mirror and the Cu $K\beta$ radiation is removed at the same time. The remaining radiation is led to a rotatory absorber which protects the detector varying the absorption. Afterwards, the beam passes through a 4-bounce monochromator, it removes the Cu $K\alpha_2$ radiation while the Cu $K\alpha_1$ radiation (λ= 1.5406 Å) beam is focused into the sample. The diffracted beam from the material reaches the detector and the beam intensity is monitored during the measurement. There are two different detectors: a scintillation detector and a position sensitive detector. The scintillation detector has an analyzer with selectable divergence slit, this is a punctual detector that measures without

considering the position, this detector is used for the 2θ/ω scan and for the XRR measurements. The position sensitive detector (LynxEye) is sensitive to the position, it consists in a series of linear detectors that can work in linear (1D, all the detectors measuring at the same time) or punctual mode (0D, acts as a single detector, the slits have to be closed), this detector in the 0D mode is used for the rocking curve measurement.

4.1.2. Wavelength Dispersive X-Ray (WDX)

In this non-destructive technique, the sample is bombarded with electrons and the characteristic X-rays generated from the sample are recorded to identify the elemental constituents of it. It separates the X-rays by diffracting them with crystals, collecting one wavelength at a time. Then a spectrum is generated in which the peaks correspond to specific X-ray lines and the elements can be easily identified. Quantitative data can also be obtained by comparing peak heights or areas of the analyzed sample with a standard material with known response. WDX spectrum is acquired sequentially as the full wavelength range is scanned.

In this Thesis, WDX measurements were carried out by PhD. Elaine Taylor and Dr. Robert Martin at the University of Strathclyde. A Cameca SX100 electron probe micro-analyzer (EPMA) was used to analyze the composition of the $Al_xIn_{1-x}N$ layers. The electron beam voltage was set to 7 kV to probe the topmost ~ 200 nm of the layer.

Figure 4.5. Cameca SX100 electron probe micro-analyzer (EPMA) located at the University of Strathclyde.

4.1.3. X-Ray Photoelectron Spectroscopy (XPS)

XPS is a widely-used surface analysis technique that can be applied to a broad range of materials. A X-ray beam is used to excite the sample and to produce photoelectrons. The energy of the photoelectrons leaving the sample provides a spectrum with a series of photoelectron peaks. The binding energy of the peaks is characteristic of each element. The peak intensity can be used (with appropriate sensitivity factors) to determine the composition of the materials surface. The shape of each peak and the binding energy can be slightly altered by the chemical state of the emitting atom. It provides quantitative chemical information from the surface of the material being studied, due to the short range of the photoelectrons that are excited from the solid.

In order to study the composition profile along the sample, XPS measurements were performed combined with Ar sputtering cycles. In this way, the sputtering with Ar removes some atomic layers of the sample each time and it is possible to know by XPS the composition of each layer.

In this work, XPS measurements were done at the IMDEA Nanoscience by Dr. Cristina Navío. These measurements were performed under ultra-high vacuum conditions (UHV, with a base pressure of 5×10^{-10} mBar) on layers grown on sapphire substrates using a monochromatic Al K_α line as exciting photon source ($h\nu = 1486.7$ eV), a hemispherical energy analyzer (SPHERA U7 analyzer pass energy) was set to 20 eV for the XPS measurements to have a resolution of 0.6 eV. To compensate the built-up charge on the sample surface during the measurements it was necessary the use of a flood gun (Specs FG 500) with low energy electrons of 3 eV and 40 A. The depth profile experiments were performed by alternating XPS measurements with cycles of Ar sputtering (Specs IQE 11A sputter gun).

4.1.4. Field Emission Scanning Electron Microscopy (FESEM)

In FESEM measurements, the surface of the sample is scanned point by point with a high-energy beam of electrons. The interaction of these primary electrons with the sample produces the emission of secondary and backscattered electrons. The detected secondary and backscattered electrons are used for building an image which contains information about the surface morphology of the layers.

FESEM images, both in cross-section and surface, have been used to obtain information about the type of growth (columnar or compact), the layer thickness and the material growth rate.

The FESEM images have been done in different places, in the Centro de Apoyo Tecnológico of the Universidad Rey Juan Carlos (URJC) using a FEI Nova NanoSEM 230 microscope, in the CIEMAT in Madrid by Dr. Fernando José Sánchez with a Carl Zeiss Auriga Compact and in the CEA-Grenoble using a Zeiss Ultra 55 Plus microscope by Dr. Sirona Valdueza-Felip under the supervision of Dr. Eva Monroy. All systems consist of a high resolution in-lens secondary detector which allows high contrast topographic imaging working in both secondary and backscatter modes. Thanks to the in-lens secondary detector they can analyze non-conductive materials without a previous metallization process.

4.1.5. Atomic Force Microscopy (AFM)

AFM is a technique that provides a topographic image of the surface of an analyzed sample. This image allows to obtain information about the surface morphology in terms of root-mean-square (RMS) surface roughness, the average grain size and, in some cases, a grain density estimation. AFM is based on the Van der Waals forces of attraction that a tiny silicon probe tip mounted at the end of a cantilever experiences when approaching to the surface of the material under study. Figure 4.6 exhibits a scheme of an AFM system. The cantilever is mounted on a piezoelectric actuator and a laser beam is reflected by the cantilever (coated by aluminum) and collected by a position sensitive photodetector. The deflection of the cantilever (given by the signal in the photodetector) is used as input of the piezoelectric actuator that moves the cantilever along the z-axis.

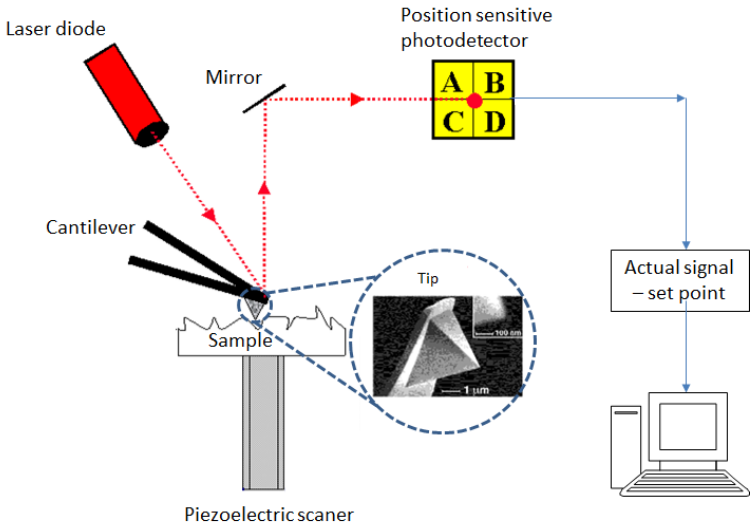

Figure 4.6. Schematic representation of the AFM setup.

Three different measurement modes are commonly used in AFM technique (Figure 4.7). Among the different measurement modes, the contact mode is based on the interaction between the sample and the tip at distances below 1 Å. The force between the tip and the sample surface is kept constant during the scanning of the area under study by maintaining a constant deflection of the cantilever.

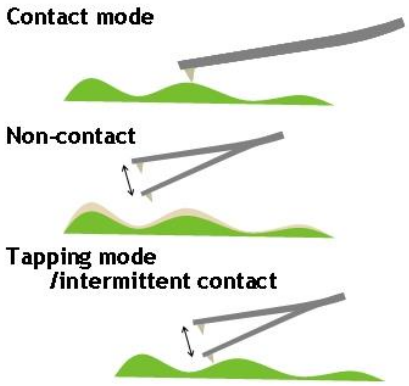

Figure 4.7. Different measurements modes of AFM [Wiki00].

On the contrary, the non-contact mode measures surface topography by using the attractive inter-atomic force between the tip and the sample surface. The absence of repulsive forces permits its use in the imaging of "soft" samples. The non-contact mode has the advantage that the tip never contacts the sample and therefore cannot disturb or destroy the sample.

The tapping mode operation is a type of non-contact mode where the probe tip is oscillating with a fixed frequency at near its resonance, while the amplitude of the oscillation is monitored. Starting from free oscillation amplitude, the tip is approached to the sample until its amplitude is reduced to a given set point value, which is selected to reduce the damage to the sample. When the oscillating tip is close enough to the surface (less than 10 nm), Van der Waals interaction between sample atoms and tip atoms arises. Then, the oscillation amplitude is kept at the set point and the z-position is now controlled by the feedback mechanism. The variations of the z-position of the tip during scanning are plotted as a function of the position of the tip on the xy plane to compose the surface height image.

In this work, AFM measurements were carried out in the CEA-Grenoble facilities under the supervision of Dr. Eva Monroy. These measurements were performed in tapping mode with a Veeco Dimension 3100 microscope and probe tips Bruker OTESPA with a resonant frequency of 300-50 kHz. And in a Nanoscope IIIa system using a Bruker TESP-SS tip which resonant frequency is of 320 kHz was used in the CNME of the Complutense University. Data visualization and processing were performed by using the WSxM software [HFGC07].

4.2. Electrical properties

Electrical characterization techniques could provide information about the carrier concentration, the type of carriers, the resistivity of the material and the carrier mobility. In this section the main methods used to characterize the electrical properties of the group III-nitride layers are described.

4.2.1. Hall Effect

The Hall effect occurs when an electric current flow through a semiconductor placed on a magnetic field which is perpendicular to the electric current, in this case, appears a voltage perpendicular to both, the magnetic field and the electric current direction.

This technique provides information about the carrier concentration (n), the type of majority carriers (p-type or n-type), and the carrier mobility (μ).

The Hall effect has been measured by using the Van der Pauw configuration. Which requires the placement of four small ohmic contacts on the boundaries of the sample.

When the measurement is done without the influence of a magnetic field, forcing the current on adjacent nodes and measuring the voltage on opposite adjacent nodes (see Figure 4.8 right), the resistivity of the material (ρ) is estimated.

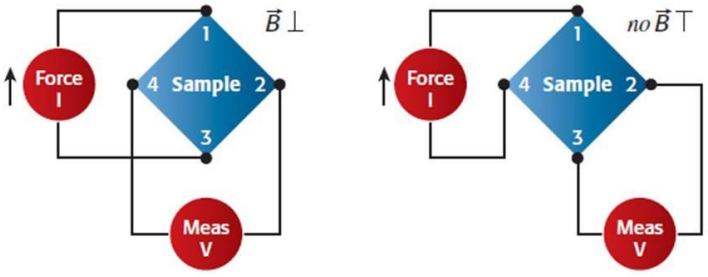

Figure 4.8. Van der Pauw configuration for measuring the: left: Hall scattering factor and right: material resistivity [Gree79].

When the current is forced on opposite nodes of the sample and then the voltage is measured on the other opposite nodes under the influence of a perpendicular magnetic field (see Figure 4.8 left), the Hall scattering factor (R_H) is estimated. The R_H provides information about the type of majority carriers present in the analyzed layer, being positive for p-type samples, and negative for n-type samples. Once the R_H is known, the carrier concentration of the layer is obtained using Eq. (4.3),

$$n = \frac{1}{qR_H} \tag{4.3}$$

where, q is the electron charge.

The carrier mobility (μ) can be also obtained knowing the thickness of the layer and the resistivity of the material (ρ) by applying Eq. (4.4),

$$\mu = \frac{1}{q\rho n} \tag{4.4}$$

where, q is the electron charge, ρ is the resistivity of the material and n is the carrier concentration.

In this work, Hall effect measurements carried out in the Van der Pauw configuration were performed at room temperature. Ohmic indium contacts were placed in $0.5\times0.5\ cm^2$ square samples. The Hall effect measurements were done with a magnetic field intensity of ±1 T. Hall Effect characterization measurements were carried out in the CEA-Grenoble facilities under the supervision of Dr. Eva Monroy.

4.3. Optical properties

The optical characterization is done by optical transmittance (Tr), reflectance (R) and photoluminescence (PL) measurements. They provide information about the band gap energy, and its relationship with impurities and crystal defects. The knowledge of these optical properties is fundamental for optimizing the material growth process.

4.3.1. Transmittance

Optical transmittance measurements allow the estimation of the linear absorption of a semiconductor layer and its band gap energy. The evolution of light intensity when it propagates through an absorptive medium is given by the Lambert-Beer's Law:

$$I\ \lambda, x\ = I_0\ \lambda\ e^{-\alpha\ \lambda\ x} \tag{4.5}$$

where, I(λ,x) is the light intensity at position x, I_0 is the intensity of the light which enters the sample, α(λ) is the absorption coefficient of the sample and x is the position.

The transmission of the light when propagating through a material is defined as the ratio of the transmitted (I) and incident (I_0) light intensity as: $Tr\ \lambda\ = I(\lambda)/\ I_0(\lambda)$. Once the transmittance of the samples is known, it is straightforward to estimate the absorption of the materials through the relation (Eq. (4.6)) which neglects the reflection losses at the different interfaces in the sample and light scattering losses:

$$\alpha\ E\ d = -\ln[Tr\ E\ ] \tag{4.6}$$

where, d is the thickness of the layer.

In this work, the effective band gap energy of the samples under study is estimated assuming a sigmoidal approximation of the absorption coefficient as [MMDS99]:

$$\alpha = \frac{\alpha_0}{1 + e^{\frac{E_0 - E}{\Delta E}}} \tag{4.7}$$

where α_0 is the linear absorption well above the band gap, ΔE is the absorption band edge broadening, E is the photon energy, and E_0 is a fitting parameter that marks the inflection point of the sigmoidal function.

The transmittance of the samples has been studied in the range of 350 to 1700 nm. The light source is a white broadband lamp that presents an emission at this wavelength range. Figure 4.9 left shows the light beam collimated and delivered through the sample. Then the normal incidence transmitted light is focused into a 600-µm-diameter optical fiber using a 20× magnification microscope objective. The optical fiber is connected to an Optical Spectrum Analyzer (O.S.A.) which has two detectors (Si and InGaAs) that cover the visible and near infrared spectral range.

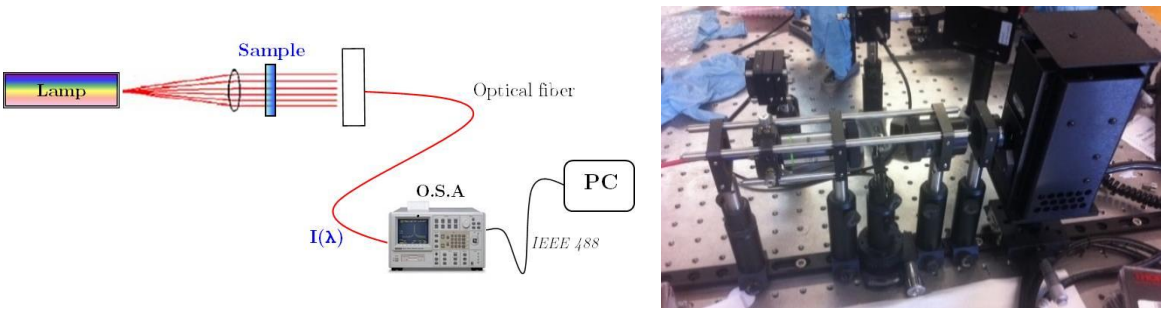

Figure 4.9. Linear optical transmittance setup in the range of 350 to 1700 nm. Left: scheme. Right: Experimental setup located at the Alcalá University.

The measurements are performed with and without sample to obtain the transmittance spectra of the sample by the ratio between them. This system is located at the GRIFO facilities in the Electronics Department of Alcalá University (see Figure 4.9 right).

4.3.2. Reflectance

The reflectance is defined as the ratio of incident flux on a sample surface to reflected flux from the surface, it gives an idea of the amount of light that is reflected by the material.

These measurements were carried out in the CIEMAT in Madrid by Dr. Susana Fernández. The measured reflectance by this system is the specular reflectance. A Perkin–Elmer Lambda 1050 UV/Visible/NIR spectrophotometer is used. The light beam is focused on the sample with mirrors so that it is perpendicular to the sample. As a reference an aluminum mirror is measured. Three detectors (PMT, InGaAs and PbS) are used for collecting the data in the different wavelength ranges.

4.3.3. Photoluminescence

Photoluminescence (PL) spectroscopy consists of the study of the optical emission of a material which is optically excited.

In the PL experiments the sample is excited with a laser, which photon energy is above (wavelength below) the band gap energy (wavelength) of the material in order to generate electron-hole pairs in the sample (see Figure 4.10). The excited electrons can recombine with a hole in the valence band and produce the emission of light (radiative recombination). In this case, the energy of the photoluminescence emission is related to the band gap energy of the material. In general, the yield of PL is governed by a competition between radiative and non-radiative recombination. The sources of non-radiative recombination are mainly defects in the material (for example impurities and crystal disorders).

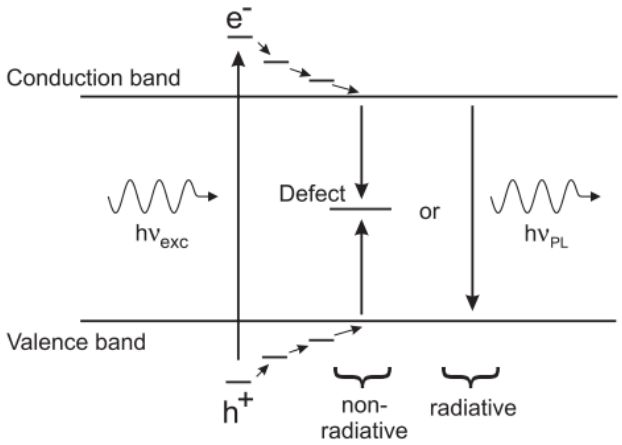

Figure 4.10. PL mechanism in semiconductors, [LGHK01].

Furthermore, the intensity and broadening of the PL emission peaks can be related to the crystalline quality and homogeneity of the sample. In this sense, high-quality

materials present an intense and sharp PL emission. PL measurements as a function of the temperature of the samples also provide information about the thermal activation energy of the involved recombination process.

The integrated PL emission intensity decreases when increasing the temperature, first it decreases smoothly and at higher temperatures (for kT comparable to the activation energy of the impurity) it decreases drastically, this is known as quenching. The fitting of the evolution of the integrated PL intensity as a function of the temperature gives information about the activation energy of the extinction process that is being analyzed. Normally it can be use the equation (4.8) that only takes into account one non-radiative recombination channel [LGBN99]:

$$\mathrm{I\ T\ } = \frac{\mathrm{I(T=0K)}}{1 + a \cdot \exp\left(-\frac{\mathrm{E}_a}{\mathrm{k_B T}}\right)} \tag{4.8}$$

where E_a is the average energetic barrier required for carriers to escape from their localization and reach the non-radiative recombination centers, $\mathrm{k_B T}$ is the thermal energy, and a is a fitting constant associated with a non-radiative-to-radiative recombination ratio.

The Stoke's Shift is a parameter that is obtained from the comparison between the band to band related PL emission energy and the band gap energy calculated from Tr spectra at the same temperature. This parameter provides information about the band edge of the layers.

Figure 4.11. PL experimental setup. Left: continuous-wave argon laser. Right: cold finger Helium cryostat and lenses.

Figure 4.11 illustrates the PL setup used in this work, it is located in the CEA-Grenoble facilities and the measurements were done under the supervision of

Dr. Eva Monroy. The excitation source is a continuous-wave argon laser (λ = 488 nm) with an optical power of 23 mW. The diameter of the laser spot is of 50 µm. The signal is collected into a 45-cm-focal-length Jobin-Yvon monochromator and detected by a charge-coupled-device (CCD) camera. The samples are mounted in a cold finger helium cryostat to perform variable temperature PL measurements ranging from low temperature (T = 5 K) until room-temperature (T = 300 K). The cryostat is equipped with a sapphire window to have minimum absorption in the studied wavelength range. A filter at 515 nm is used for filtering the wavelengths below 515 nm so that the laser effect is removed and the information from the sample is obtained.

Chapter 5

Growth of $Al_xIn_{1-x}N$ on sapphire by RF sputtering

5.1. Introduction

As it was explained in Chapter 1, the III-nitride semiconductors and their ternary alloys have become increasingly important in light-emitting devices, and also as candidates for solar cells and opto/chemical sensing.

Many reports on the synthesis of $Al_xIn_{1-x}N$ on sapphire have been published, some use MOCVD [ADKA10, YKNK98], others MBE [CWPH14, WWCT14], and others sputtering deposition [DXCL09, GOKT07, NMVN16, PPQO97, GTNO08, GYTN03, HCFG10, HCFW10, JiSG09, KuKF89, LDTD13, LüDW13]. The growth by sputtering is mainly done with a plasma formed by a mixture of nitrogen and argon, argon is mainly included for increasing the growth rate. Thus, the use of pure nitrogen instead of an argon and nitrogen mixture leads to lower deposition rates and thus the layer properties are highly affected.

In this Chapter, the effect of the growth conditions (mainly RF power applied to the Al target and substrate temperature) on the structural, chemical,

morphological, electrical and optical properties of the $Al_xIn_{1-x}N$ layers grown on sapphire by RF sputtering is studied. This information has been reported as a journal article in Journal of Physics D: Applied Physics [NVMM16].

5.2. Deposition conditions

The $Al_xIn_{1-x}N$ layers studied in this chapter were grown on (0001)-oriented sapphire substrates using the RF sputtering described in Chapter 3. Pure In (99.995%) and pure Al (99.999%) targets were co-sputtered in a pure nitrogen (99.9999%) ambient. The substrates were chemically cleaned in acetone and methanol and then blown down with nitrogen before being loaded in the sputtering chamber. Then, they were outgassed for 30 min at 550°C. After this cleaning procedure, the substrates were cooled down to the growth temperature. Prior to the deposition, the targets and the substrate were cleaned using plasma etching with Ar (99.999%) in the growth chamber. $Al_xIn_{1-x}N$ layers were then deposited with the nitrogen flow, sputtering pressure and RF power applied to the indium target kept at 14 sccm, 0.47 Pa and 40 W, respectively [VNGL10]. A sputtering time of 4 h was used for all the samples.

Table 5.1. Summary of the growth conditions of the $Al_xIn_{1-x}N$ samples: RF power applied to the Al target (P_{Al}); substrate temperature (T_s).

	Sample	**P_{Al} (W)**	**T_s (ºC)**
Set A	**S1**	0	300
	S2	75	300
	S3	85	300
	S4	105	300
Set B	**S5**	150	300
	S6	150	350
	S7	150	450
	S8	150	500
	S9	150	550

Two set of samples were grown for studying the influence of the deposition conditions on the $Al_xIn_{1-x}N$ properties. In the first one the RF power applied to the Al target (P_{Al}) was varied from 0 W to 150 W while the substrate temperature (T_s) was kept constant at 300°C (set A, S1 – S5). Secondly, T_s was varied from 300°C to 550°C with P_{Al} fixed at 150 W (set B, S5 – S9). The growth conditions are summarized in Table 5.1.

5.3. Experimental results

5.3.1. Structural, chemical and morphological characterization

The 2θ/ω X-ray scans of the samples of set A are depicted in Figure 5.1 left. On it, two peaks are observed within the analyzed 2θ range, they correspond to the $Al_xIn_{1-x}N$ (0002) and the Al_2O_3 (0006) reflections. This confirms that the layers present wurtzite structure with the *c*-axis aligned to that of the sapphire substrate.

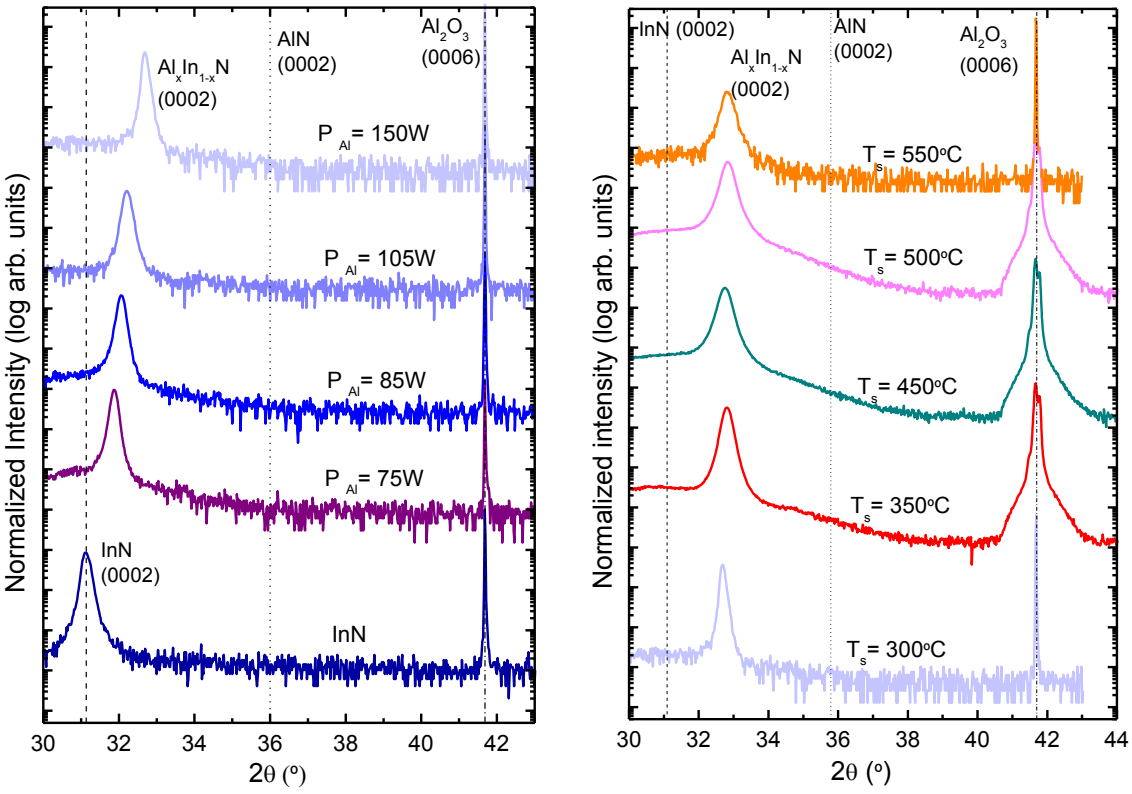

Figure 5.1. 2θ/ω scans of the samples of (left) set A and (right) set B. The dotted and dashed lines point the position of the AlN (0002) and InN (0002) reflection peaks, respectively.

The increase of the P_{Al} leads to an increase of the diffraction angle for the $Al_xIn_{1-x}N$ layer reflection, which is related with a reduction of the *c* lattice parameter from 5.741 Å for S1 to 5.474 Å for S5. As explained in Chapter 4 and using Eq. (2.2) the Al content of the layers can be estimated assuming fully relaxed strain state, for the studied layers of set A it increases from 0 to 0.32 as a function of P_{Al} (see Table 5.2).

Table 5.2. Summary of the layer thickness estimated with FESEM; Al mole fraction x and *c*-axis parameter extracted from HRXRD and WDX measurements respectively; strain along the (0001) axis (ε_{zz}); in-plane strain (ε_{xx}).

Sample	**Thickness (nm)**	**Al content x_{HRXRD}**	**c_{HRXRD} (Å)**	**Al content x_{WDX}**	**c_{WDX} (Å)**	**ε_{zz} (%)**	**ε_{xx} (%)**
S1	365	0	5.741	-	5.703	0.67	-0.81
S2	370	0.13	5.611	-	-	-	-
S3	370	0.17	5.579	0.18	5.574	0.09	-0.12
S4	385	0.21	5.553	0.24	5.531	0.40	-0.54
S5	530	0.32	5.474	0.36	5.445	0.53	-0.76
S6	500	0.34	5.455	-	-	-	-
S7	575	0.33	5.465	0.38	5.431	0.63	-0.90
S8	475	0.35	5.452	-	-	-	-
S9	455	0.35	5.453	0.39	5.423	0.55	-0.78

In the case of the samples grown ranging the substrate temperature, the peak related to $Al_xIn_{1-x}N$ (0002) diffraction (Figure 5.1 right) barely changes its position with the growth temperature (see Table 5.2).

WDX measurements were performed in order to study more precisely the composition of the layers. The values obtained by this technique are summarized in Table 5.2, a comparison with the values obtained previously by HRXRD measurements show that these values are slightly higher than those calculated from HRXRD. This difference can be attributed to residual strain present in the layers due to the lattice mismatch with the sapphire substrate (29% and 13.3% in-plane lattice mismatch for InN and AlN on sapphire, respectively).

The estimation of the strain state (ε_{zz}) of the $Al_xIn_{1-x}N$ layers has been carried out calculating the relaxed *c* lattice parameter using the Al composition obtained by

WDX measurements c_{WDX} (see Eq. (2.2)). Then, the strain along the *c*-axis has been calculated as $\varepsilon_{zz} = c_{HRXRD} - c_{WDX} / c_{WDX}$, obtaining values in the (0.9 to 5.3)×10^{-3} range (tensile strain). Assuming that the stress during the growth was biaxial, i.e. isotropic in-plane stress and no stress along the growth axis, the in-plane strain (ε_{xx}) can be calculated by using Eq. (2.8), the elastic tensor coefficients used are estimated by extrapolating the ones shown in Table 2.2 taking into account the layer composition. The calculated ε_{xx} is in the range of (−1.2 to −7.6)×10^{-3} (compressive strain). The compressive nature of ε_{xx} is consistent with the growth on sapphire substrates, and the fact that the layers are almost fully relaxed as expected in such a mismatched heteroepitaxial system (see Table 5.2). It should be pointed out that the value of $|\varepsilon_{zz}|$ increases when increasing the layer thickness (see Table 5.2), which points to the aluminum content as the main factor at the origin of the strain state of the layers. Furthermore, three layers (S5, S7 and S9) with similar Al composition and different thicknesses present similar strain state.

As described in Chapter 4, the FWHM of the ω−scan gives information about the structural quality of the layers. In the present study, the FWHM of the InN (0002) is of 2.4° while the FWHM of the (0002) $Al_xIn_{1-x}N$ reflection of samples of set A is in the range of 1.4°–1.9°, without a clear trend as a function of P_{Al}. Thus, all the samples present a similar structural quality. These values are comparable with previous results in $Al_xIn_{1-x}N$ samples grown by MBE [TCIY06]. The samples of set B present a FWHM of the ω-scan around the (0002) $Al_xIn_{1-x}N$ reflection peak that increases from 1.4° to 3° when increasing the substrate temperature from 300 to 550°C, this is maybe due to the reduction of the grain size that occurs when increasing the substrate temperature (from 53 to 25 nm, for 300 and 550°C, respectively) associated with the change in the layer morphology from closely-packed columnar to compact.

Figure 5.2(a) shows the evolution of the RMS surface roughness extracted from 2×2 μm^2 AFM images of the $Al_xIn_{1-x}N$ films with P_{Al}. There is a markedly increase of the RMS surface roughness when incorporating Al to the InN layer attributed to a change in morphology from compact InN (S1) to closely-packed columnar $Al_{0.13}In_{0.87}N$ (S2). Figure 5.2 (b-e) show the AFM micrographs and cross-sectional FESEM images of the InN sample (S1) and the $Al_xIn_{1-x}N$ sample deposited with P_{Al} = 75 W (S2). The change in morphology is explained by the low mobility of the

impinging Al atoms which leads to a reduction of the surface mobility of In and N species. The increase of the P_{Al} from 75 W to 150 W induces a decrease of the surface roughness while keeping the closely-packed columnar morphology unaltered (see AFM and FESEM images of S5 in Figure 5.3(b-c), respectively). The reduction of the RMS surface roughness when increasing P_{Al} is attributed to the corresponding increase of kinetic energy of the Al atoms impinging the growing surface.

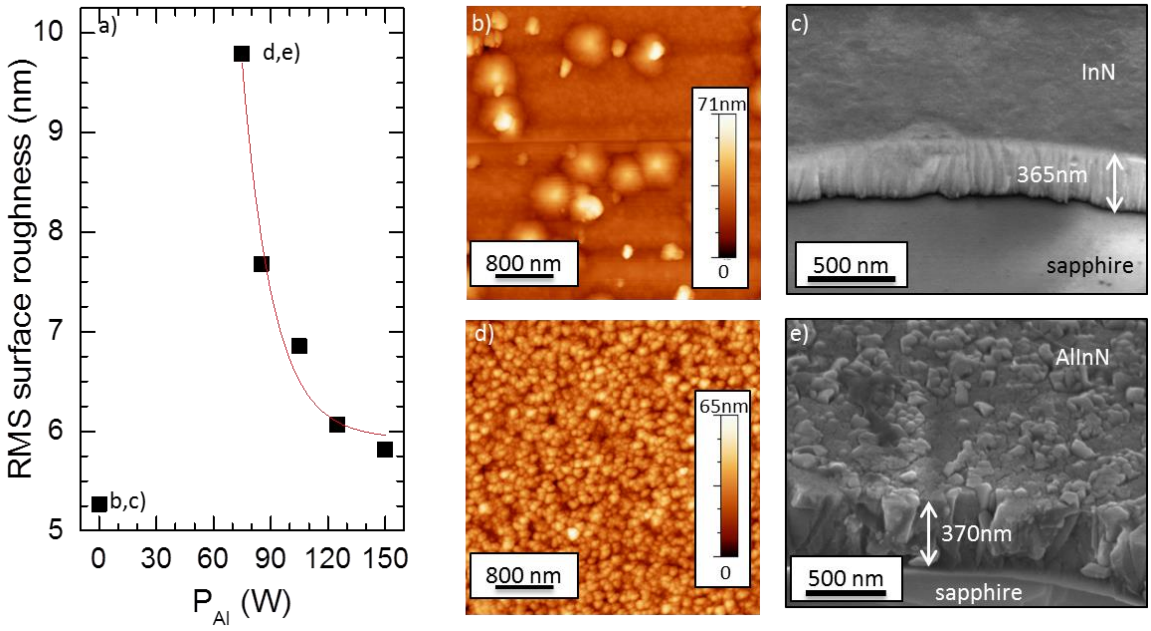

Figure 5.2. a) RMS surface roughness evolution of the $Al_xIn_{1-x}N$ samples as a function of P_{Al}. The solid line is a guide to the eye. b) 4×4 μm² AFM and c) FESEM of the InN layer (S1, P_{Al} = 0); d) 4×4 μm² AFM and e) FESEM of the $Al_{0.13}In_{0.87}N$ layer (S2, P_{Al} = 75 W). The AFM and FESEM images of the sample grown at P_{Al} of 150 W (S5) are shown in Figure 5.3 (b-c).

The effect of the substrate temperature has been studied in set B. The increase of the substrate temperature improves the mobility of the adsorbed species. A slight increase of the aluminum content, from 0.36 to 0.39, with the T_s ranging from 300 to 550°C has been measured by WDX. The slight change in Al concentration in the layer is consistent with an enhanced desorption of physi-adsorbed In atoms.

When the growth temperature increases from 300°C to 550°C, the RMS surface roughness drops from 5.8 nm to 0.8 nm (comparable to best values for sputtered AlN on sapphire [MVNG13]) (see Figure 5.3(a)). This reduction in the RMS surface

roughness in related with a change in the layer morphology, the layers evolve from closely-packed columnar structures (Figure 5.3(b, c), S5) to compact films (Figure 5.3(d, e), S9), with a reduction of the growth rate from 143 nm/h to 113 nm/h. This indicates that the increase in substrate temperature compensates the drop in surface mobility caused by the presence of Al.

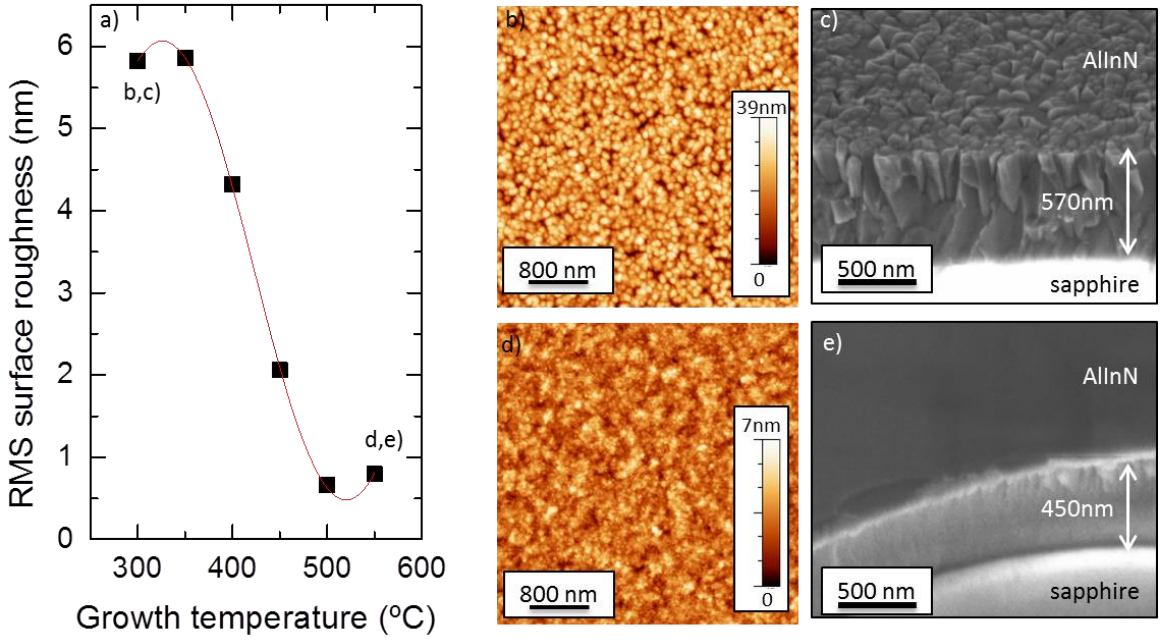

Figure 5.3. a) Estimated RMS surface roughness of $Al_xIn_{1-x}N$ samples as a function of T_s with P_{Al} of 150 W. The solid line is a guide to the eye. b) 4×4 μm² AFM and c) FESEM of the $Al_xIn_{1-x}N$ layer grown at 300°C (S5); d) 4×4 μm² AFM and e) FESEM of the $Al_xIn_{1-x}N$ layer grown at 550°C (S9).

5.3.2. Electrical characterization

The electrical properties of the layers were analyzed by Hall effect measurements in the Van der Pauw configuration as described in Chapter 4, the RT resistivity and free carrier concentration of the $Al_xIn_{1-x}N$ layers as a function of the Al mole fraction is shown in Figure 5.4a). The Al mole fraction is the one extracted from WDX, except in the case of S2 where it is estimated from HRXRD measurements (in this case the Al mole fraction measured by HRXRD and WDX should be comparable because, as observed in Table 5.2, the differences between these measurements increase when increasing the Al composition (samples of set A)).

In this case the increase of Al composition leads to a drop of the carrier concentration by more than one order of magnitude. This high carrier concentration can be related with high oxygen present in the layers, it has been measured by WDX measurements to be ~7% for S5. For $Al_xIn_{1-x}N$ layers grown by sputtering with similar Al composition without oxygen impurity [YeWL08], the measured carrier concentration is in the range of $3 \cdot 10^{18}$ cm^{-3} (for a 36% Al) to $3 \cdot 10^{20}$ cm^{-3} (for a 12% Al, which is lower than the one reported here. This means that the oxygen present in the layer can be responsible for the high carrier concentration. On the contrary, there is an increase of the resistivity from $\rho_s = 0.2$ m$\Omega \cdot$ cm for InN (S1) to 11.5 m$\Omega \cdot$ cm for $Al_{0.36}In_{0.64}N$ (S5). The results for InN are in agreement with previous literature [GSNO98, VNGL11]. The observed change in the electrical properties of the $Al_{0.13}In_{0.87}N$ layer in comparison to those of the InN might be related with several factors:

- The columnar morphology tends to increase the resistivity and to decrease the carrier concentration because of the scattering, carrier trapping and band bending at the boundaries.
- The increase of the band gap energy with the Al content should increase the activation energy of the impurities leading to a decrease of the carrier concentration [LONL02].

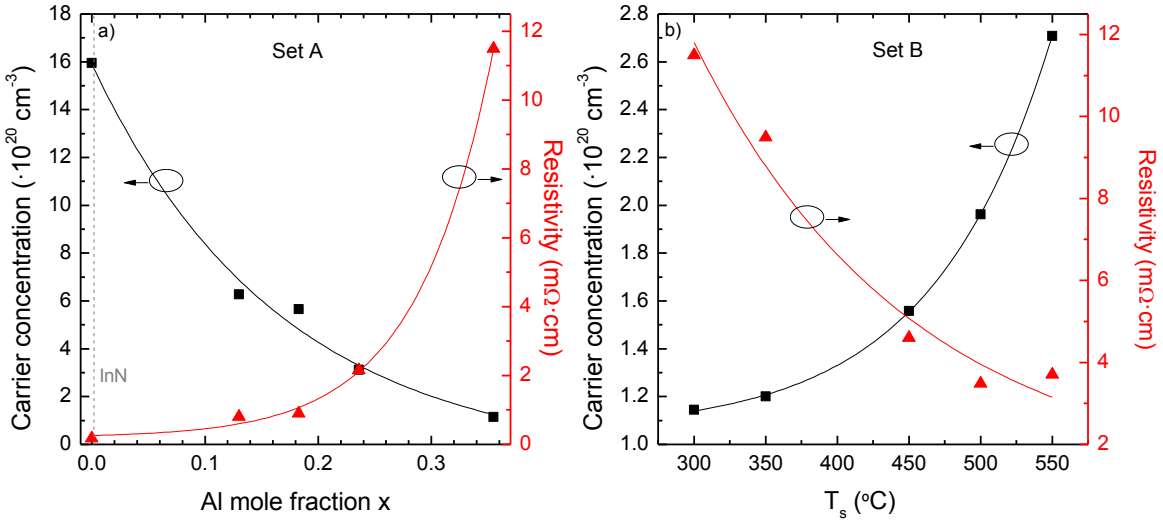

Figure 5.4. Dependence of the $Al_xIn_{1-x}N$ carrier concentration and resistivity on: a) the aluminum mole fraction (set A) and b) the substrate temperature (set B).

Figure 5.4b) shows the evolution of the carrier concentration and resistivity with the substrate temperature. The decrease in the carrier concentration with the growth temperature can be related with a decrease in the oxygen content of the layers, XPS measurements were performed on sample S9 to estimate the existence of oxygen in the $Al_xIn_{1-x}N$ sample. From these experiments, a homogeneously distributed O concentration of ~4% was detected within the sample depth, this oxygen concentration is also confirmed by WDX measurements. This result is in agreement with the reported one by Bhuiyan *et al.* [BSKH03] and Yoshimoto *et al.* [YYHH03], who observed a relationship between O concentration and the induced blue-shift of the emission of InN samples. In this case the increase of the surface adatom mobility when increasing the T_s barely changes the layer composition, but it affects significantly to the deposition mode. This increase in the adatom mobility and thus the change in the morphology from closely-packed nanocolumns (S5) to a compact layer (S9) leads to a drop of the resistivity from $\rho_s = 11.5\ \mathrm{m\Omega \cdot cm}$ to $3.7\ \mathrm{m\Omega \cdot cm}$, by a factor of ~3, which confirms that the enhancement observed in this set was indeed due to the morphology. The resistivity drop is also associated with an increase of the carrier concentration, which changes only by a factor of 2. During the growth of thin films different steps happen, namely the nucleation of small islands, then the growth and coalescence of the islands, and finally the two-dimensional growth [PBHG03]. The process of attaining two-dimensional growth relays on a high enough adatom mobility, which depends on the growth conditions and on the nature of the substrate. In this particular case, an enhancement of the adatom mobility is achieved by increasing the substrate temperature. For the compact $Al_{0.39}In_{0.61}N$ sample, S9, the values of resistivity and mobility ($\rho_s = 3.7\ \mathrm{m\Omega \cdot cm}$ and $\mu \cong 6.2\ \mathrm{cm^2/Vs}$) are similar to those reported by Liu *et al.* ($\rho_s = 1.2\ \mathrm{m\Omega \cdot cm}$ and $\mu = 11.4\ \mathrm{cm^2/Vs}$ for $Al_{0.28}In_{0.72}N$ layers grown by sputtering deposition by sputtering a Al/In target under a mixture of N_2 and Ar atmosphere [LTDC12]). The high resistivity of sample S9 can be related with conductivity through grain boundaries due to the low grain size of the sample as it has been described by other authors in ZnO layers [JoKh01].

5.3.3. Optical properties

The inset of Figure 5.5a) shows the transmission spectra of the samples of set A. As explained in Chapter 4, the absorption coefficient (α) of the layers is estimated

from the transmission spectra and then the apparent optical band gap energy (E_g) is obtained by a linear fit of the squared absorption coefficient as a function of the photon energy (dashed line in Figure 5.5a)).

Table 5.3. Room-temperature absorption edge (E_g); absorption band edge broadening (ΔE); linear absorption well above the band gap (α_0); and room-temperature PL emission energy (E_{PL}) of the samples under study.

Sample	**E_g (eV)**	**ΔE (meV)**	**α_0 ($\times 10^4$ cm^{-1})**	**E_{PL} (eV)**
S1	1.76	143	12	1.59
S2	1.85	144	13	-
S3	1.88	145	12	1.71
S4	1.94	150	11	-
S5	2.03	154	8.3	1.86
S6	2.04	180	9.2	-
S7	1.98	210	7.7	-
S8	1.99	210	8.9	-
S9	2.00	220	9.1	1.65

A blue shift of the E_g from $E_g = 1.76$ eV ($\lambda_g = 704$ nm) for InN (S1) to $E_g \sim 2.0$ eV ($\lambda_g = 610$ nm) for $Al_{0.39}In_{0.61}N$ (S9) can be observed in the summary of Table 5.3. These values of E_g are related to the high carrier concentration measured in the layers (in the range of 10^{20} cm^{-3}) and the Burstein-Moss effect.

The absorption spectrum of the layers was modeled by using a sigmoidal approximation given by Eq. (4.7). An average value of $\alpha_0 = (1.1 \pm 0.2) \times 10^5$ cm^{-1} is obtained, with ΔE increasing from 143 meV to 220 meV with the Al incorporation maybe due to alloy inhomogeneities, as summarized in Table 5.3.

The band gap energy as a function of the aluminum mole fraction calculated from WDX is depicted in Figure 5.5b), This graph also includes a comparison between the experimental data of this work and the experimental data from layers grown by MBE. The difference between both curves is explained by the Burstein-Moss effect. This difference decreases when increasing the aluminum content of the $Al_xIn_{1-x}N$ layer because of the measured reduction of carrier concentration with the Al content (blue shadow in Figure 5.5b) as a guide to the reader).

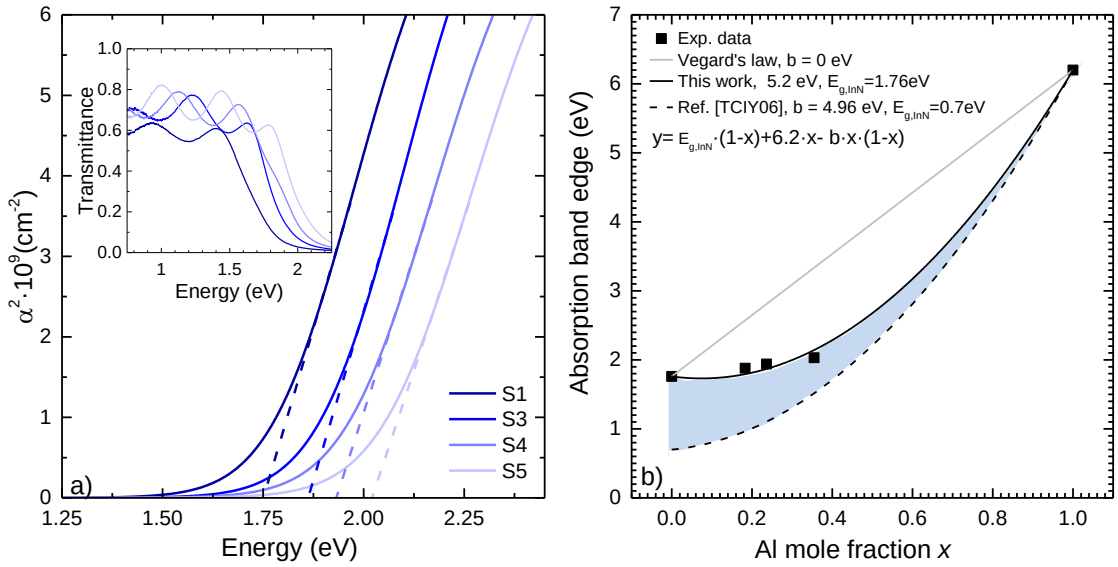

Figure 5.5. a) Square of the absorption coefficient as a function of the photon energy of $Al_xIn_{1-x}N$ layers with different composition. The inset shows the room-temperature transmittance spectra of the same layers. b) The band gap energy of $Al_xIn_{1-x}N$ as a function of Al composition (from WDX), including a parabolic guide to the eye and an indication (shaded) of the difference from a bowing parameter expression using the band-gap of pure InN.

Figure 5.6 shows the RT PL emission of the samples of set A, the FWHM of the PL ranges from 370 – 490 meV. The Stokes shift between the PL emission and the absorption edge energy calculated is about ~170 meV for all the samples of set A. This value is similar to the one presented by other authors for InN films grown by sputtering [PSZO06]. However, in set B, the Stokes shift increases from ~170 meV for S5 to ~350 meV for S9. This high Stokes shift is in agreement with the calculations of Jiang *et al.* [JiSG09] who relates it with fluctuations in the In distribution, or with deep defects or impurities acting as preferential recombination centers. It should be pointed out that the PL peak emission energy of the sample S9 recovers the value obtained for the InN sample (1.65 eV versus 1.59 eV, as summarized in Table 5.3).

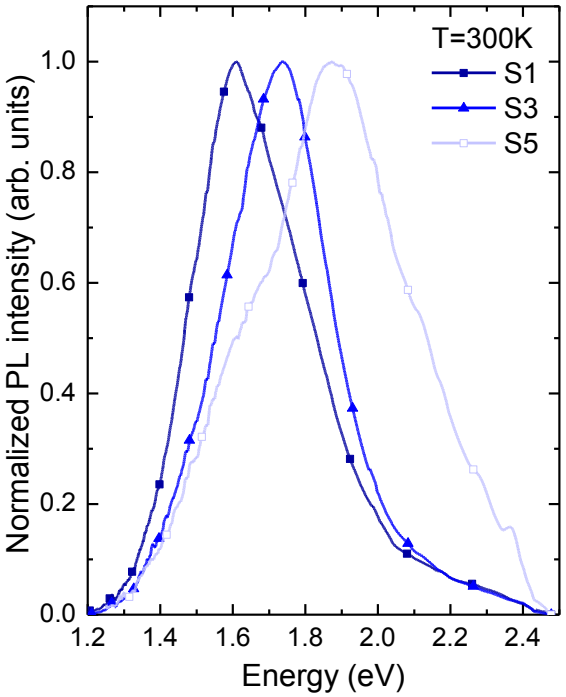

Figure 5.6. Normalized room-temperature PL emission spectra of the samples grown with different P_{Al}. The peak that appears at ~1.3 eV is an artifact of the PL setup.

Figure 5.7a-c) show the evolution of the PL emission as a function of the temperature of the InN layer (S1) and of layers with the same Al content for samples S5 (columnar) and S9 (compact), respectively. The PL intensity of the InN layer (S1) drops a factor of ×1.2 when increasing the temperature from T = 5 K to RT, however the columnar $Al_{0.36}In_{0.64}N$ sample (S5) presents a ×1.6 drop of the PL intensity, whereas for the compact $Al_{0.39}In_{0.61}N$ sample (S9) the drop is by a factor of ×5 when increasing the temperature measurement. The thermal stability of samples S1 and S5 is tentatively attributed to carrier localization in high In-content fluctuations or impurities. The integrated PL emission as a function of the temperature is shown in Figure 5.7d). The thermal evolution of the PL is characterized by a quenching of the intensity due to the activation of non-radiative recombination processes, together with a red shift and broadening of the emission. The evolution of the integrated PL emission ($I(T)$) can be described considering a single nonradiative recombination channel by Eq. (4.8) [LGBN99]. The solid lines in Figure 5.7(d) display the fit of the experimental data to Eq. (4.8) $\left(I(T) = \frac{I_0}{1 + a \cdot e^{\frac{E_a}{k_b T}}} \right)$. $E_a = 51 \pm 18$ meV, $a = 2.93$ for S1, $E_a = 19 \pm 7$ meV, $a = 0.96$

and $E_a = 28 \pm 5$ meV, $a = 8.6$ values of activation energy and a are obtained for S5 and S9 samples, respectively. The PL emission energy of samples S1 and S9 is very similar which is attributed to a similar defect or impurity originating the emission. However, the different activation energies can be due to the different grain size of the layers (36 nm for S1 and 25 nm for S9). In the case of S5, a different PL emission energy is measured, it being tentatively addressed to other impurity which may be related to the different morphology presented in this sample. The defects that can be related with the emissions are mainly: oxygen, hydrogen, indium fluctuations or nitrogen-related impurities [BSKH03, BWCT04, DLBA10, Wu09].

The Varshni equation (2.12) $\left(E_{PL}(T) = E_{PL}(0) - \frac{\gamma T^2}{\beta + T} \right)$ has been used to describe the evolution of the PL emission energy with the temperature, in this particular case the Vegard's law [Vega21] has been used for estimating the γ and β constants taking into account the composition of samples S5 and S9. These values are estimated to be $\gamma = 0.2$ meV/K and $\beta = 624$ K for S1, $\gamma = 0.74$ meV/K and $\beta = 890$ K for S5, and $\gamma = 0.8$ meV/K and $\beta = 920$ K for S9. The evolution of the PL emission energy as a function of the temperature is shown in Figure 5.7d) and the solid lines drawn on it show the agreement of the experimental data to Eq. (2.12).

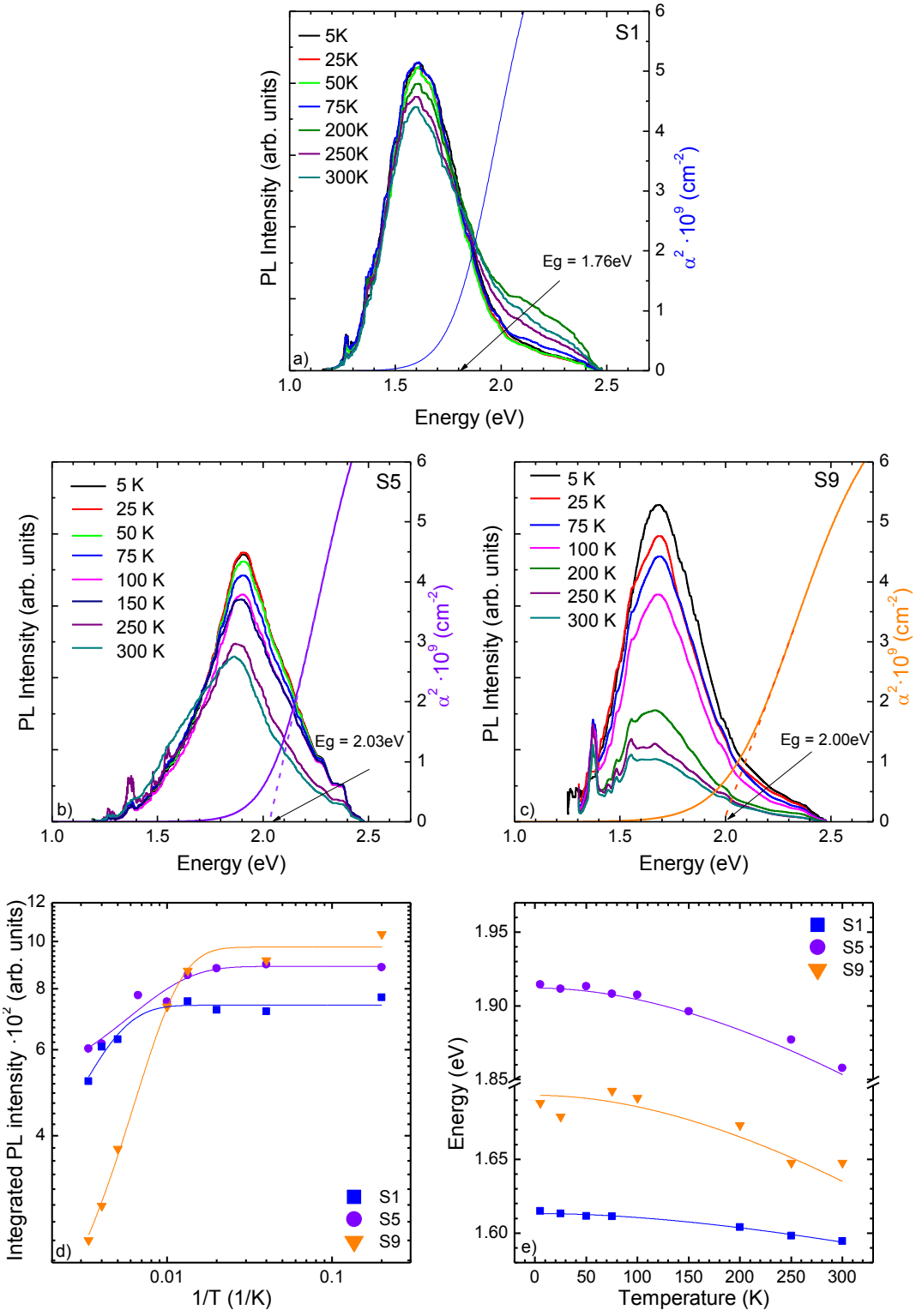

Figure 5.7. Temperature-dependent PL spectra of a) InN (S1), b) $Al_{0.36}In_{0.64}N$ (S5) and b) $Al_{0.39}In_{0.61}N$ (S9). The peak that appears at ~1.3 eV is an artifact of the PL setup. c) Thermal evolution of the integrated PL emission intensity of the analyzed InN and $Al_xIn_{1-x}N$ layers. The solid lines show the fit of the experimental data to Eq. (4.8). d) Temperature dependence of the PL emission peak energy. The solid lines indicate the agreement of the experimental data to Varshni Eq (2.12).

5.4. Conclusions

In this Chapter the properties of the $Al_xIn_{1-x}N$ layers grown on sapphire by RF sputtering are studied as a function of the growth conditions, mainly the effect of the power applied to the aluminum target (0-150 W) and substrate temperature (300-550°C).

- It is possible to grow $Al_xIn_{1-x}N$ layers by RF sputtering on sapphire substrates by co-sputtering pure In (40 W) and Al (0-150 W) targets in a nitrogen rich ambient.
- For the growth conditions under study, polycrystalline layers highly oriented in the *c*-axis and with wurtzite structure are achieved.
- The layers grow under compressive strain in sapphire substrate as it is expected but they are almost fully relaxed.
- The Al content of the alloy is varied between 0 and 0.36 when increasing the power applied to the aluminum target from 0 to 150 W at a fixed temperature of 300°C. The achieved layers present closely-packed columnar morphologies with surface roughness between 10—6 nm.
- The layer morphology evolves from columnar to compact layers when increasing the substrate temperature from 300 to 550°C while keeping constant the power applied to the Al target to 150 W. The surface roughness is reduced with the change in layer morphology.
- All the $Al_xIn_{1-x}N$ layers present high carrier concentration (in the range of 10^{20} cm^{-3}), this leads to a high Burstein-Moss effect in the band gap energy.
- The increase in Al content increases the band gap energy and a bowing parameter of 5.2 eV has been calculated.
- The layers present RT photoluminescence, a blue shift of the PL emission peak is observed when increasing the Al content.
- The best properties obtained for the analyzed conditions are achieved for samples grown over 450°C and at 150 W of P_{Al} (x=0.39), i.e. compact morphology with high surface quality (roughness below 2 nm) and a band

gap energy of ~2 eV, making them appropriate for their application to photoconductors and high reflectivity mirrors in the visible wavelength range.

Chapter 6

Growth of $Al_xIn_{1-x}N$ on *p*-Silicon (111) by RF sputtering

6.1. Introduction

The unique properties of III-nitrides, presented previously in Chapter 2, make these semiconductors interesting for different applications as described in Chapter 1. In particular, the III-nitride layers grown on silicon substrate have application in solar cells [YIKH10] or energy harvesting [GCGG14]. As for layers grown on sapphire (Chapter 5), $Al_xIn_{1-x}N$ layers have been grown on silicon substrates by different techniques [CWPH14, CWTY14, DXCL09, HBDD07, HDDS10, LTDC12].

The band gap tunability of the $Al_xIn_{1-x}N$ alloy offers large possibilities to engineer the electronic structure for each specific application. For example, In-rich $Al_xIn_{1-x}N$ thin films have potential application in multijunction solar cells since the band gap energy in the range from 0.7 to 2.4 eV covers most part of the solar spectrum [YIKH10].

This Chapter focuses on the development of $Al_xIn_{1-x}N$ layers on p-Si (111) by RF sputtering specially for its application as solar cells. The structural, morphological, chemical and optical properties of the layers are investigated as a function of the growth conditions. The first part of this Chapter, presents a systematic study of

the growth of In-rich $Al_xIn_{1-x}N$ layers deposited by reactive radio-frequency magnetron sputtering directly on p-doped silicon (111) substrates. Then we study the growth of AlN on p-Si (111) and its use as a buffer layer for $Al_xIn_{1-x}N$ layers.

Part of this Chapter (section 6.2) has been reported as a journal paper in Japanese Journal of Applied Physics [NMVN16].

6.2. Growth of $Al_xIn_{1-x}N$ directly on p-Si (111)

6.2.1. Deposition conditions

$Al_xIn_{1-x}N$ samples were deposited on p-doped Si (111) substrates using the reactive sputtering described in Chapter 3. The growth procedure for all the samples presented in this section was the following: the substrates were chemically cleaned in organic solvents and once they were loaded to the sputtering chamber, they were outgassed for 30 min at 550°C and then cooled down to the growth temperature. The targets and substrate were pre-sputtered with pure Ar (5N) plasma to remove surface contaminants. Pure In (4N5) and pure Al (5N) cathodes were co-sputtered using pure nitrogen (6N) as reactive gas. The nitrogen flow rate and, sputtering pressure were kept at 14 sccm, and 0.47 Pa, respectively, these parameters were previously optimized by our group growing InN on p-Si (111) [VNGL10]. The RF power applied to the indium target was kept constant at 40 W. The layer thickness is around 500 nm for all layers.

The effect of the RF power applied to the Al target (P_{Al}) and the substrate temperature (T_s) on the properties of the $Al_xIn_{1-x}N$ layers have been studied by growing two set of samples. In the first set of samples (set A, samples M1-M6 in Table 6.1) the P_{Al} was varied from 0 to 150 W while keeping the substrate temperature at $T_s = 300$°C. The second set of samples (set B, samples M6-M9 in Table 6.1) was grown at a constant P_{Al} of 150 W and various T_s values from 300 to 550°C.

Table 6.1. Summary of the growth conditions of the $Al_xIn_{1-x}N$ samples from sets A (M1-M6) and B (M6-M9).

	Sample	P_{Al} (W)	T_s (°C)
Set A	**M1**	0	300
	M2	75	300
	M3	85	300
	M4	105	300
	M5	125	300
Set B	**M6**	150	300
	M7	150	350
	M8	150	450
	M9	150	550

6.2.2. Experimental results

6.2.2.1. Structural, chemical and morphological characterization

The 2θ/ω scans measured by HRXRD of the $Al_xIn_{1-x}N$ layers grown with different P_{Al} are shown in Figure 6.1. In the analyzed 2θ range only the diffraction peaks of the $Al_xIn_{1-x}N$ (0002) and Si (111) are observed. This indicates that the layers present wurtzite structure oriented with the *c*-axis perpendicular to the sample surface. The increase of P_{Al} shifts the (0002) reflection peak towards high diffraction angles, which means that there is a reduction of the c lattice parameter from 5.714 Å for InN (M1) to 5.446 Å for $Al_xIn_{1-x}N$ deposited with P_{Al} = 150 W (M6). The layer composition can be estimated using Eq. (2.2) and assuming fully relaxed layers. It ranges from $x = 0$ to 0.36 for the P_{Al} range under study (see Table 6.2, samples M1 to M6).

The Al content was further studied by WDX measurements and a difference <1.5% has been found between both measurements (see table 6.2) which means that the layers are almost fully relaxed achieving values of ε_{zz} below 0.25% without a clear tendency. On the other hand, the FWHM of the rocking curve around the (0002)

reflection of the $Al_xIn_{1-x}N$ ranges between 2.2 to 5.3° without a clear tendency for the samples of set A.

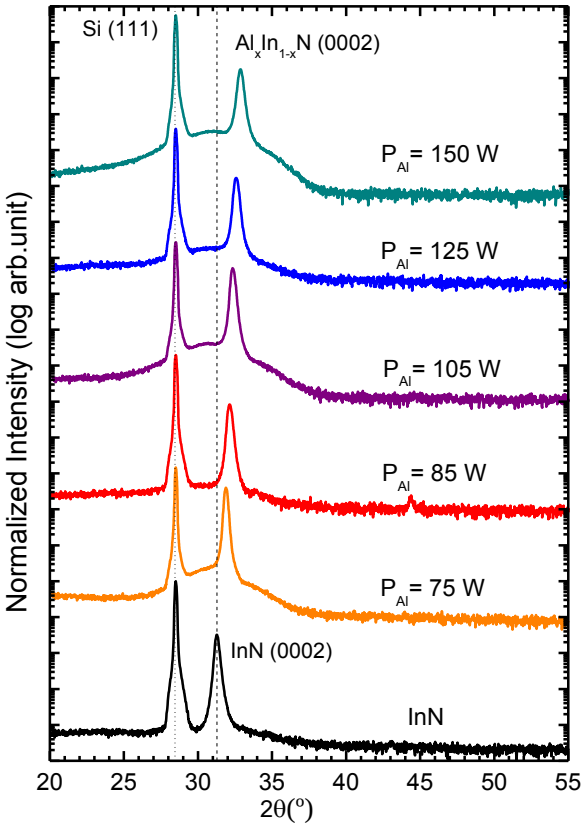

Figure 6.1. HRXRD 2θ/ω scans of the $Al_xIn_{1-x}N$ samples grown on p-Si (111) at different RF powers applied to the Al target (set A).

Table 6.2. Summary of the Al content and *c*-axis parameter estimated by HRXRD and WDX measurements.

Sample	Al content x_{HRXRD}	c_{HRXRD} (Å)	Al content x_{WDX}	c_{WDX} (Å)	RMS (nm)
M1	-	5.714	0	5.703	11.3
M2	0.13	5.609	-	-	6.7
M3	0.19	5.565	019	5.570	5.6
M4	0.24	5.530	0.22	5.544	6.3
M5	0.29	5.492	0.30	5.488	5.3
M6	0.36	5.446	0.37	5.438	3.1
M7	0.37	5.433	-	-	3.4
M8	0.37	5.437	0.37	5.440	3.5
M9	0.36	5.442	0.39	5.427	3.5

The dependence of the RMS surface roughness with the P_{Al} is shown in Figure 6.2a). The RMS surface roughness is extracted from 2×2 μm^2 scanning area AFM micrographs. The RMS surface roughness of InN sample (M1, with $P_{Al} = 0$) is of 11.3 nm and it exhibits a close-packed morphology, as shown in the cross-sectional FESEM and AFM images in Figure 6.2b) and Figure 6.2c), respectively. In the case of the $Al_{0.13}In_{0.87}N$ grown at $P_{Al} = 75$ W (M2) the RMS surface roughness decreases to 6.7 nm, which is attributed to the incorporation of Al to the layer. Nevertheless, when increasing the P_{Al} from 75 to 150 W (and thus the Al concentration from $x = 0.13$ to 0.36) there is a change in the layer morphology, from close-packed to compact. The RMS surface roughness decreases by almost a factor of ×2. Figure 6.2d, e) show the cross-sectional FESEM and AFM images of the $Al_{0.36}In_{0.64}N$ sample (M6), respectively. No metal droplets appear in the surface of the sample even with increasing Al layer content meaning that the deposition of the $Al_xIn_{1-x}N$ layers is done in N-rich conditions. Not only the higher Al concentration can explain the change in the RMS surface roughness, it has to be also taken into account that the increase in P_{Al} is related with an increase in the kinetic energy available for the deposition process.

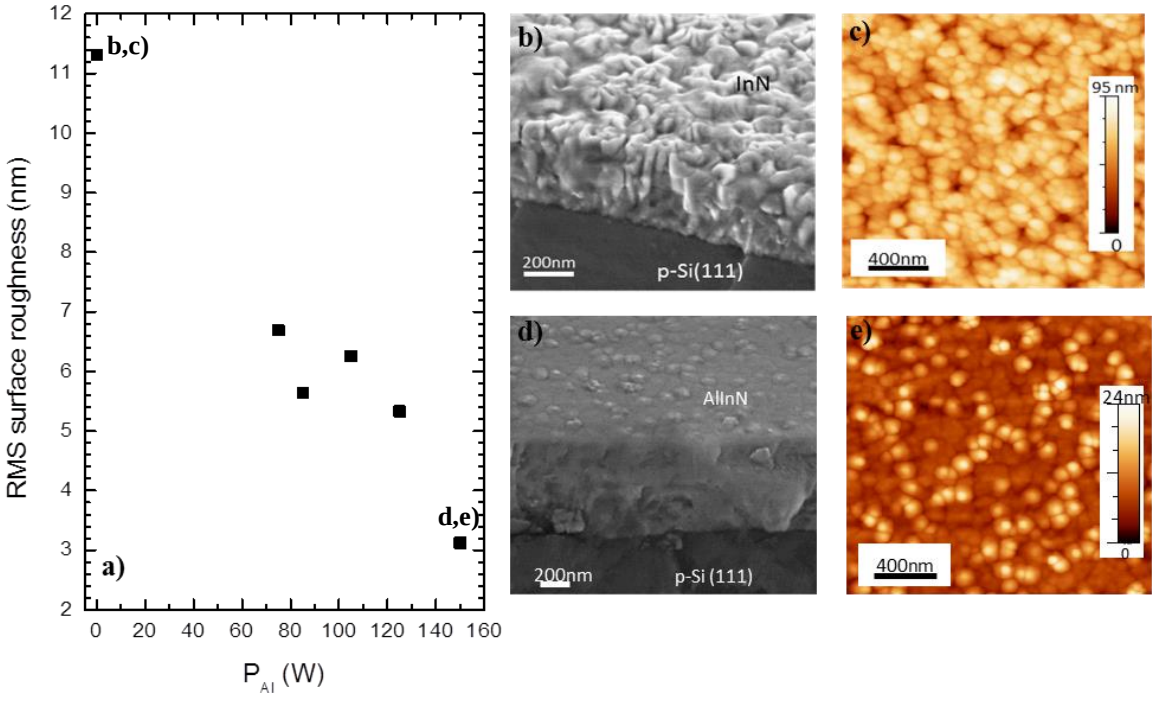

Figure 6.2. (a) Evolution of the RMS surface roughness of $Al_xIn_{1-x}N$ samples as a function of P_{Al}, with T_s = 300°C. AFM (2×2 μm^2) and FESEM images of two samples grown at 300°C and various P_{Al} values: (b) FESEM and (c) AFM images of an InN layer (M1); (d) FESEM and (e) AFM images of $Al_{0.36}In_{0.64}N$ (M6).

The second set of samples (set B, samples M6-M9) was grown at a constant P_{Al} of 150 W and the substrate temperature was varied from 300 to 550°C. Figure 6.3 shows the 2θ/ω X-ray scans of samples in set B. The $Al_xIn_{1-x}N$ (0002) diffraction peak barely changes its position, implying that there is almost no change in the alloy composition estimated assuming fully relaxed layers ($x \sim 0.36$), this has been confirmed by WDX measurements where the Al composition ranges from 0.37 to 0.39 (see Table 6.2).

The FWHM of the rocking curve of the samples under study in set B ranges from 2.9 to 4.8° without a clear tendency with the substrate temperature.

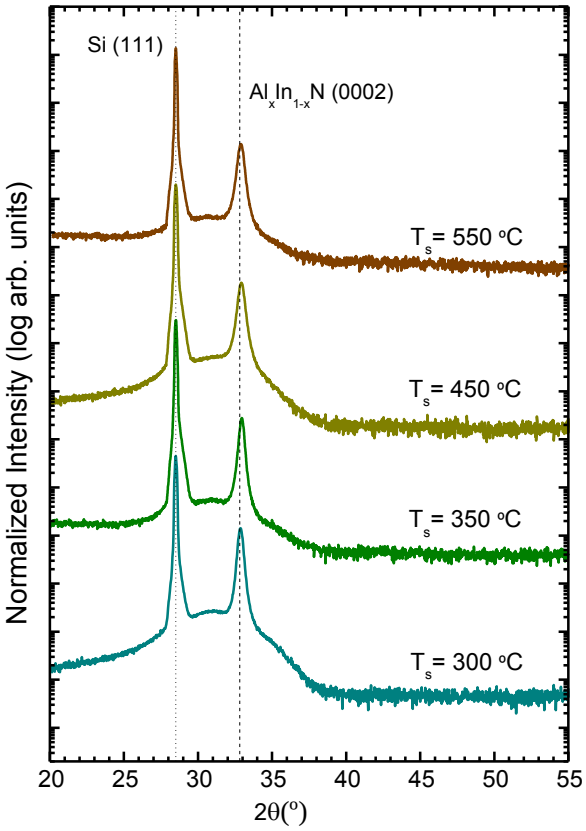

Figure 6.3. HRXRD 2θ/ω scans of the $Al_xIn_{1-x}N$ samples grown on p-Si (111) at different substrate temperatures (set B).

Table 6.2 summarizes the evolution of the RMS surface roughness of the $Al_{0.36}In_{0.64}N$ layers vs substrate temperature at $P_{Al} = 150$ W. The obtained RMS surface roughness can be considered constant, ranging between 3.1 and 3.5 nm. The FESEM and AFM images point out to a similar layer morphology for all the

samples grown within the T_s range under study (see Figure 6.4(a) and Figure 6.4(b), respectively, corresponding to sample M9).

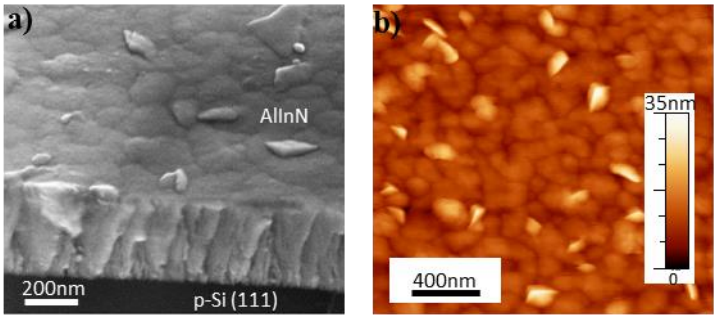

Figure 6.4. (a) FESEM and (b) AFM (2×2 μm^2) images of an $Al_{0.36}In_{0.64}N$ layer grown at 550°C (M9).

6.2.2.2. Optical properties

The optical properties of the $Al_{0.36}In_{0.64}N$ layer grown at 550°C (M9) were studied by PL measurements. The evolution of PL intensity with temperature in the 5 K - 300 K range is shown in Figure 6.5a), it displays the 30 meV red shift of the PL emission peak when increasing the measurement temperature. Besides, a strong RT PL emission is observed indicating a high optical quality.

Figure 6.5b) shows the integrated PL intensity as a function of temperature. There is a drop of a factor of ×1.5 when increasing the temperature from 5 to 300 K. This thermal stability is tentatively attributed to carrier localization in high In-content fluctuations or impurities. The thermal quenching of PL intensity can be described considering one nonradiative recombination channel as it is explained in Chapter 4, the agreement of experimental data to Eq. (4.8) is illustrated by the solid line in Figure 6.5b) obtaining an activation energy $E_a = 24.2 \pm 1.4$ meV with an a value of 1.4. This activation energy is very similar to the one achieved for the sample grown on sapphire under the same growth conditions (S9) (see Chapter 5) meaning that the related impurities are similar. Also the grain size of both samples is very similar it being 21 nm for M9 and 25 nm for S9 as reported in the previous Chapter.

The obtained PL emission energy is 1.75 eV, approximately 0.5 eV higher than that expected in samples with low carrier concentration [KKIK07], which is attributed to the Burstein-Moss effect [HCFG10] induced by the high residual carrier concentration of the layers, which has been estimated by Hall effect

measurements to be of 2.7×10^{20} cm^{-3} on a similar sample grown on sapphire (S9). The band gap energy of the sample grown on sapphire is of 2 eV.

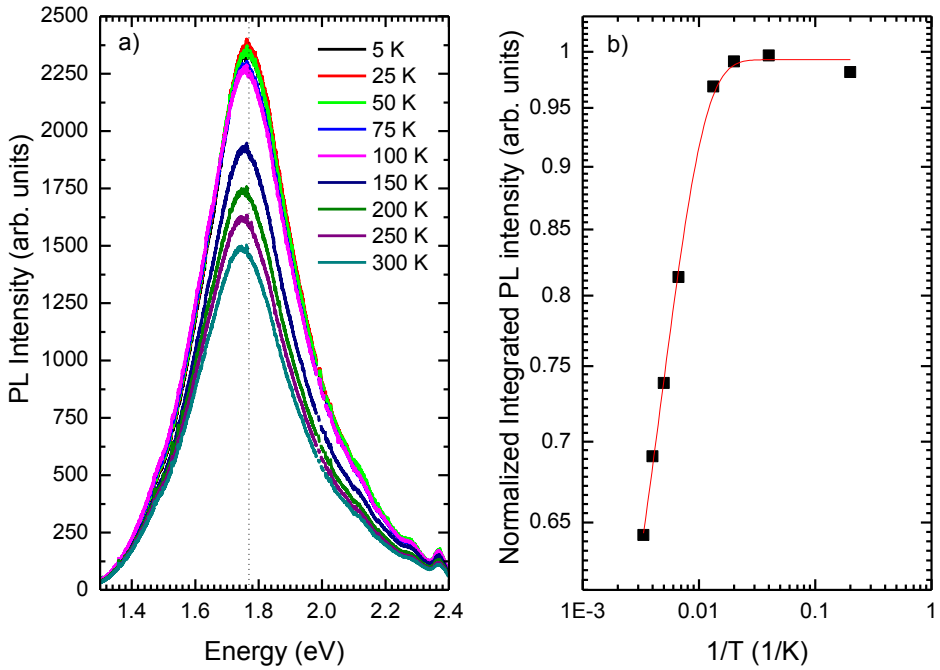

Figure 6.5. a) Variation of the PL emission spectrum with temperature, the dotted line is a guide to the eye and b) thermal evolution of the integrated PL intensity of the $Al_{0.36}In_{0.64}N$ layer grown at 550°C (M9). The solid line is the fit to Eq. (4.8).

The high carrier concentration of In-rich $Al_xIn_{1-x}N$ alloys has been attributed to different sources, such as, nitrogen vacancies (V_N), and hydrogen and oxygen impurities [BSKH03, DLBA10, Wu09]. To estimate the existence of oxygen in the $Al_xIn_{1-x}N$ samples, WDX measurements of sample M9 were performed and a ~4% of oxygen was detected.

6.2.3. Conclusions

In this part of the Chapter the structural, chemical, morphological, and optical properties of the $Al_xIn_{1-x}N$ layers grown on p-Si (111) by RF sputtering are studied as a function of the power applied to the aluminum target (0 – 150 W) and substrate temperature (300 – 550°C):

- All the samples under study present wurtzite structure highly oriented in the *c*-axis.

- The aluminum composition is ranged from 0 to 36% by increasing the power applied to the aluminum target up to 150 W, this value was estimated by HRXRD and then confirmed by WDX measurements.
- The layer morphology changes from close-packed structure to compact layers when including Al to the InN layer. And the RMS surface roughness is reduced by a factor of ×1.7.
- The change in substrate temperature from 300 to 550°C leads to layers with similar Al content and layer morphology.
- In particular, the sample grown at 550°C and with a power applied to the aluminum target of 150 W (Al mole fraction ~0.36) shows a compact morphology with an RMS surface roughness of 3 nm and a high RT PL emission intensity centered at 1.75 eV.

For improving the layer properties, this is reducing the FWHM of the rocking curve and to achieve similar RMS values to the ones achieved in $Al_xIn_{1-x}N$ layers grown on sapphire substrates, a buffer layer is needed, this is explained in the next part of the Chapter.

6.3. Improvement of the $Al_xIn_{1-x}N$ growth with a buffer layer

The film deposition is usually improved by inserting a suitable buffer layer, this buffer layer will reduce the stress of the layer caused by the lack of substrates for homoepitaxial growth. Different III- and IV-nitrides have been used as buffer layers to improve the properties of $Al_xIn_{1-x}N$ layer [FIWO04, LDTD13, SDKK09, SPHB05, TCIY06, YeWL09, YKNT00]. Among III-nitride buffer layers, GaN and AlN are frequently used.

In particular we are going to use AlN as buffer layer because our group has previously reported the improvement of InN material using it [MVNR16].

6.3.1. Optimization of the AlN buffer layer

The AlN growth on p-Si (111) by RF sputtering has been optimized in two steps. Firstly the effect of increasing the growth temperature from 450°C to 750°C was studied, secondly the effect of the power applied to the aluminum target was considered. The AlN growth on sapphire was previously optimized by our group and the growth details can be found elsewhere [Mont15, MVNG13].

6.3.1.1. Deposition conditions

The AlN samples were deposited on p-doped Si (111) substrates by sputtering 2" confocal magnetron cathode of pure Al (5N) using pure nitrogen (6N) as reactive gas. During the deposition, the nitrogen flow rate and, sputtering pressure were kept at 6 sccm, and 0.47 Pa, respectively, these parameters were previously optimized by our group [MVNG13].

Two set of samples were deposited in order to study the influence of the substrate temperature and the power applied to the aluminum target. In the first set of samples the RF power applied to the aluminum target was kept constant at 150 W while the substrate temperature was ranged from 450°C to 750°C. In the second set of samples the power applied to the aluminum target was varied from 150 W to 225 W while the substrate temperature was kept constant at 450°C. In both sets of samples a study of the introduction of an Al intermediate layer is done. The sputtering time has been fixed to 2 h for all the AlN samples under study in this section.

6.3.1.2. Effect of the substrate temperature on AlN growth

A set of 7 samples have been grown ranging the substrate temperature from 450°C to 750°C while keeping fixed the P_{Al} to 150 W.

6.3.1.2.1. Experimental results: Structural and morphological properties

Figure 6.6 shows the 2θ/ω HRXRD scans of the samples grown with different substrate temperatures. Only the Si (111) and the AlN (0002) diffraction peaks are

observed, which implies crystalline AlN layers highly oriented in the *c*-axis with wurtzite structure. The intensity of the AlN (0002) diffraction peak decreases when increasing the substrate temperature, this can be related with Al desorption.

The strain state of the layers can be estimated relating the *c*-lattice parameter obtained by HRXRD with the theoretical AlN lattice parameter by Eq. (2.6), values of ε_{zz}, in the range of –0.42 to -0.02%. This strain corresponds to a ε_{xx} of 0.53 to 0.04%, which indicate that the AlN layers are under tensile strain as expected for III-nitrides grown on silicon substrate.

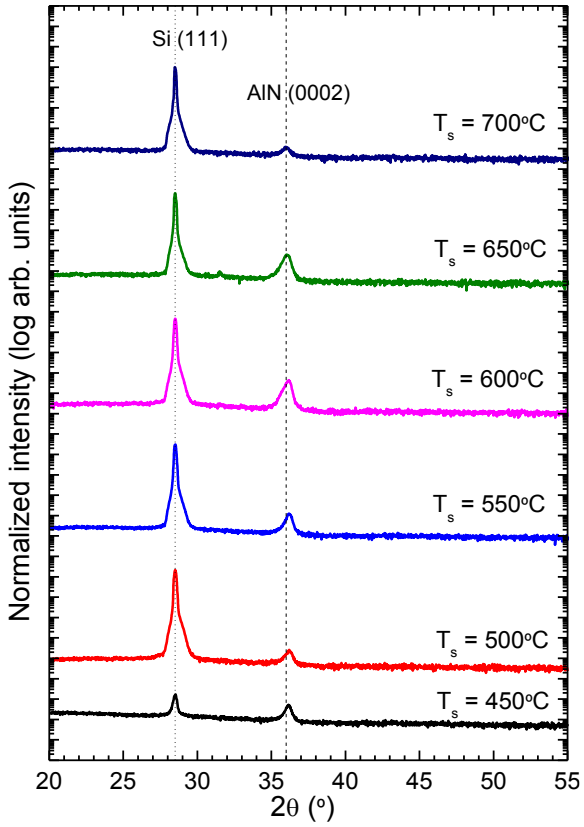

Figure 6.6. 2θ/ω scans of the AlN samples grown at different temperatures on p-Si (111), the dash line corresponds to the AlN theoretical diffraction angle.

Further analysis of the rocking curve around the (0002) AlN diffraction peak (Figure 6.7) reveals that the FWHM of this rocking curve shows its minimum value for AlN layer grown at 600°C. This means that the crystalline quality of the sample grown at 600°C is better than at other temperatures.

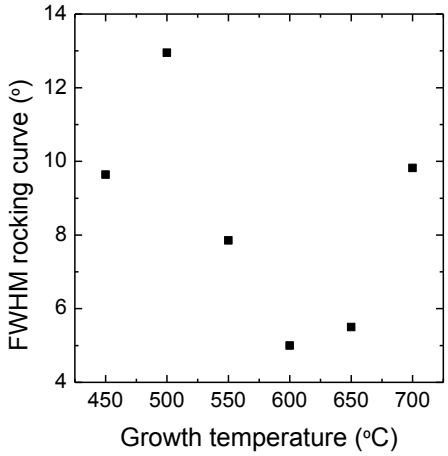

Figure 6.7. FWHM of the rocking curve of the AlN samples grown at different temperatures on p-Si (111).

Some chemical reaction with the substrate holder during growth was observed for substrate temperatures above 700°C, this implies a practical limit in the study.

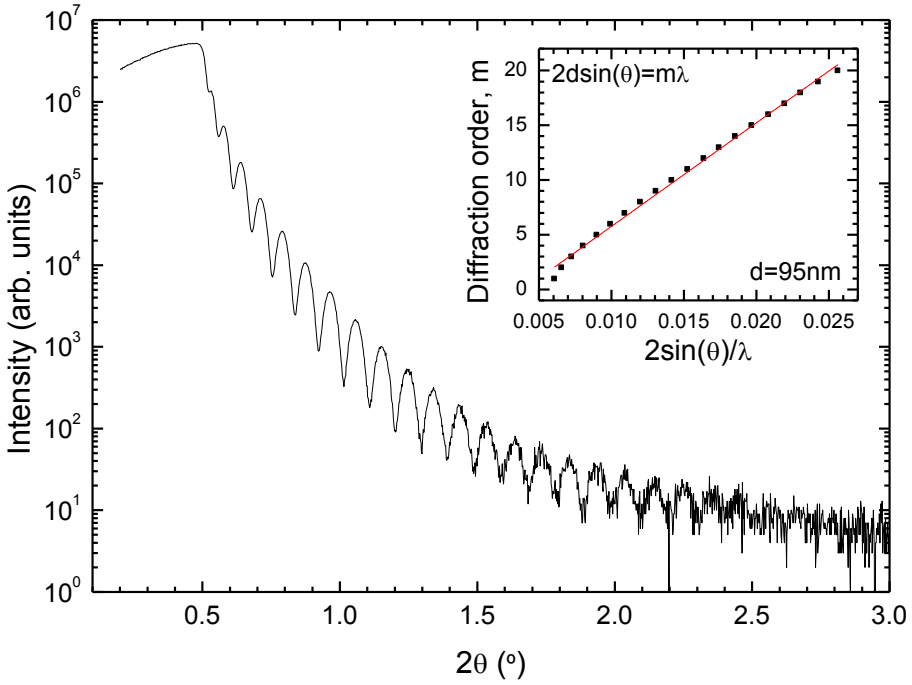

Figure 6.8. Typical XRR scan of an AlN thin film under, the inset shows the estimation of the layer thickness.

The layer thickness has been estimated through XRR measurements, through the spacing between maximums of the reflectivity together with the Bragg's equation as shown in the inset of Figure 6.8. The layer thickness for the samples under study

is of ~95 nm for samples grown at substrate temperatures up to 600°C and then it decreases to 90 nm for the one grown at 650°C and to 80 nm for the grown at 700°C. This reduction of the layer thickness with the substrate temperature is related with some desorption of the impinging species during the deposition of AlN for high growth temperatures.

Additionally, the surface morphology of the layers was analyzed by AFM. The evolution of the RMS surface roughness calculated from 1×1μm² images is depicted in Figure 6.9. The minimum RMS value is achieved at 600°C which agrees with the improvement of the crystalline quality observed by the reduction of the FWHM of the rocking curve.

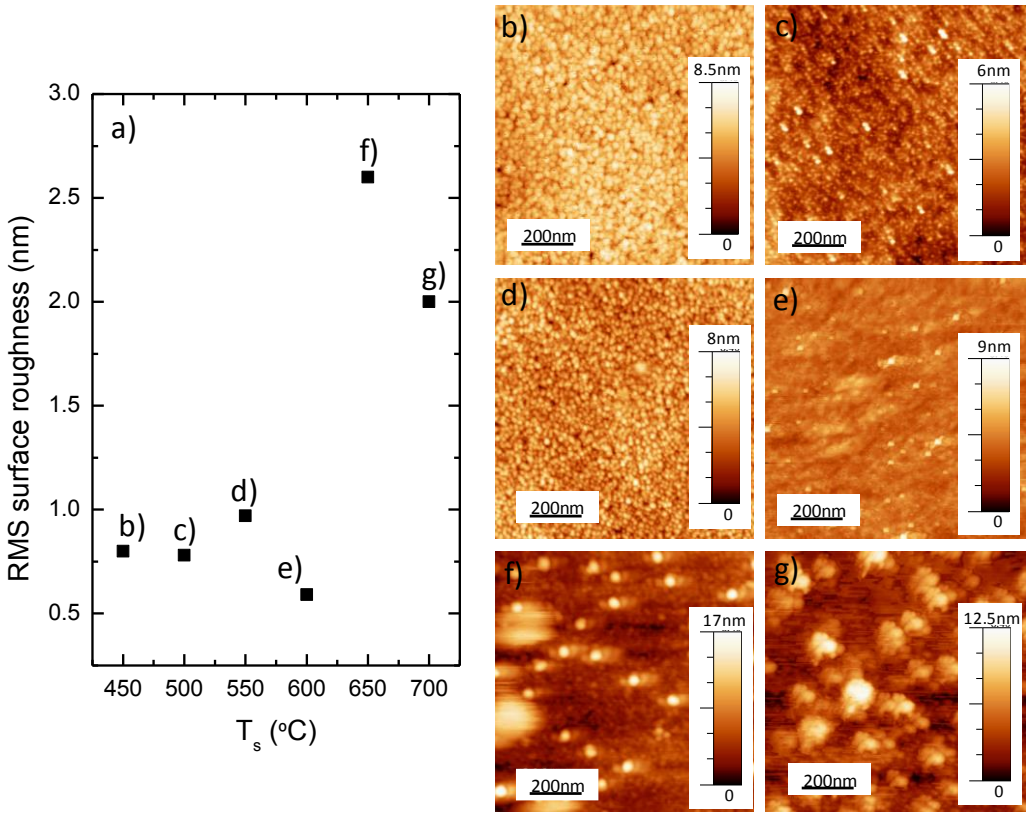

Figure 6.9. a) Evolution of the RMS surface roughness of the AlN samples grown at different T_s. 1×1 μm² AFM images: b) 450°C, c) 500°C, d) 550°C, e) 600°C, f) 650°C, g) 700°C.

6.3.1.2.2. Study of an Al intermediate layer on AlN growth

From the previous study, it was extracted that the better crystal quality (FWHM of the rocking of 5°) and the smoothest surface roughness (RMS of 0.6 nm) is

achieved for the sample grown at 600°C. This growth conditions are used to grow an AlN layer on top of different layer thicknesses of Al. The Al as intermediate layer was previously used in MBE growth to reduce the formation of a SiN in the interface of the AlN/p-Si (111) and thus to enhance the growth of AlN on p-Si (111) substrates [Sánc00]. In this report an Al intermediate layer of 3 nm is used.

A set of samples was grown in order to study the effect of the thickness of an Al buffer layer on the structural and morphological properties of the AlN layer grown on p-Si (111) by RF sputtering. The Al layer thickness was varied from 0 to 14 nm, it was grown at the same temperature as the AlN layer and using a DC power of 75 W.

Experimental results: Structural and morphological properties

Figure 6.10 shows the 2θ/ω HRXRD scans for the samples under study. For a thickness of 2 nm of Al the (0002) AlN diffraction peak is not clear, pointing out a non-crystalline layer. Also, a decrease in the intensity of the diffraction peak of AlN is observed when introducing the Al intermediate layer.

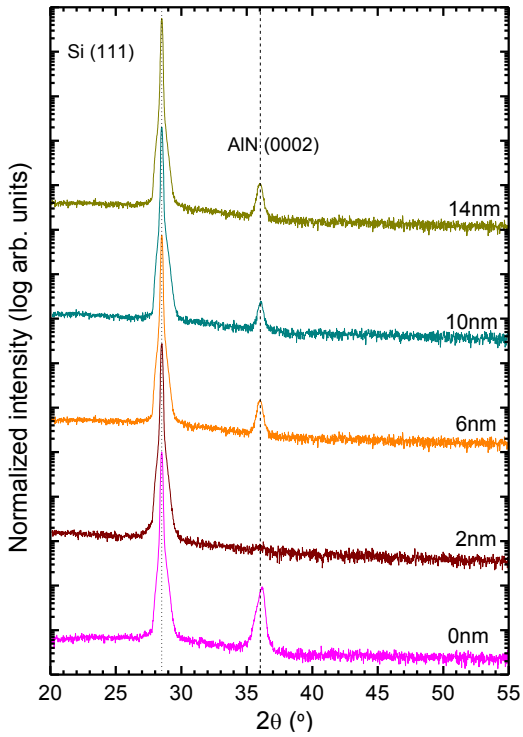

Figure 6.10. 2θ/ω scans of the AlN layers grown on p-Si (111) at 600°C and with different Al intermediate layer thickness, the dash line corresponds to the AlN theoretical diffraction angle.

The study of the crystal quality with the FWHM of the rocking curve of the (0002) AlN diffraction peak, reveals that an increase of the Al layer thickness induces a decrease of the FWHM of the AlN rocking curve, from 5.4° to 4.7° when increasing the Al layer thickness from 6 to 14 nm (see Figure 6.11).

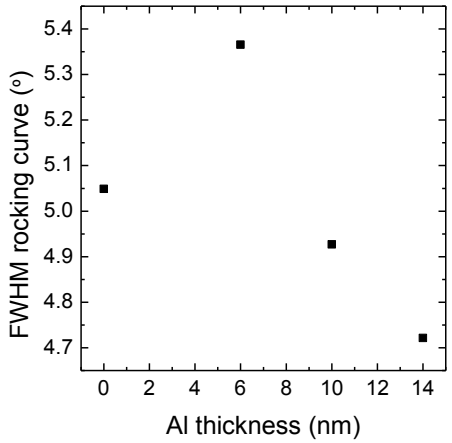

Figure 6.11. FWHM of the rocking curve of the AlN samples grown with different Al thicknesses.

The RMS surface roughness of the layers increases with the Al layer thickness (see Figure 6.12). A change in the surface morphology is shown in the AFM images, for samples with Al layer thicknesses above 6 nm. In these cases, grainy-like surfaces are observed, with an increase in the RMS related to the enlargement of the size of the surface defects. These defects are tentatively related to the formation of a continuous aluminum layer covering the substrate during the growth of the intermediate layer. This excess of Al could lead to the formation of nucleation centers for the growth of AlN upon the activation of the N plasma.

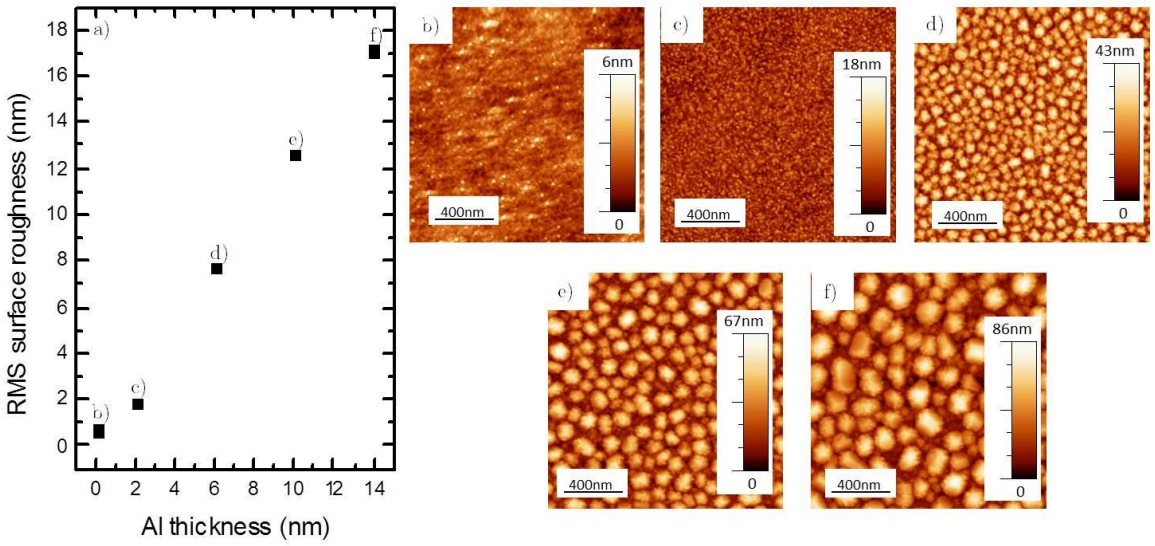

Figure 6.12. a) RMS surface roughness evolution as a function of the Al layer thickness. 2×2 μm² AFM images of the AlN samples with different Al buffer layer thicknesses b) 0 nm, c) 2 nm, d) 6 nm, e) 10 nm, f) 14 nm.

6.3.1.3. Effect of the power applied to the Al target on AlN growth

In this section a set of 4 samples have been grown ranging the P_{Al} from 150 W to 225 W while keeping fixed the substrate temperature to 450°C. This substrate temperature was chosen to avoid the change in growth temperature from the buffer layer to layer in order to reduce the impurity incorporation into the interface buffer/ $Al_xIn_{1-x}N$ layer, also the time between the growth of the buffer layer and the growth of the $Al_xIn_{1-x}N$ layer is minimized.

6.3.1.3.1. Experimental results: Structural and morphological properties

As shown in Figure 6.13, all the layers present crystalline wurtzite structure highly oriented in the *c*-axis independently of the P_{Al}.

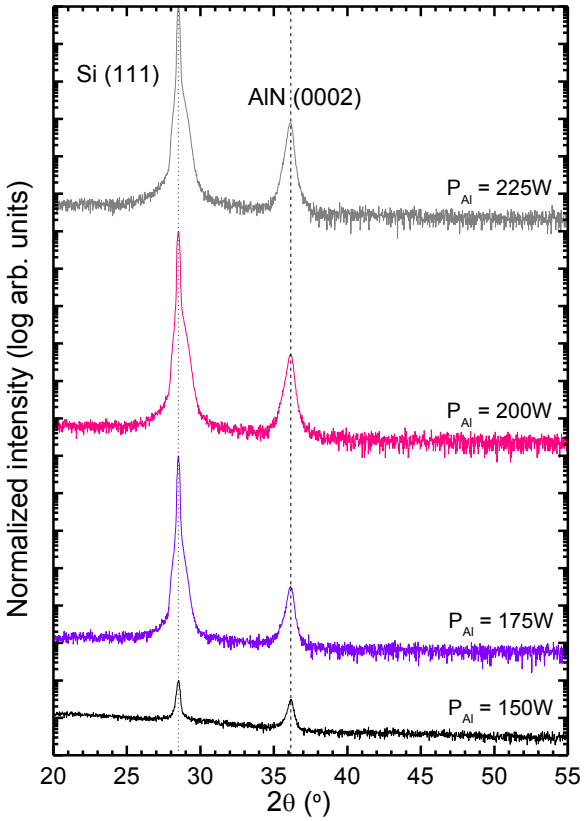

Figure 6.13. 2θ/ω scans of the AlN layers grown on p-Si (111) applying different power to the aluminum target, the dash line corresponds with the AlN theoretical diffraction angle.

The strain state (ε_{zz}) can be estimated by Eq. (2.6), the obtained values in the range of –0.31 to –0.21% decreases when increasing the power applied to the aluminum target. The ε_{xx} estimated by Eq. (2.8) points out that the layers grow under tensile strain, and it decreases from 0.53 to 0.37% when increasing P_{Al} from 150 to 225 W. The growth under tensile strain is the expected one for III-nitrides grown on Si (111) substrates.

The grain size estimated from HRXRD measurements increases when increasing the P_{Al} from 19 to 22 nm for 150 and 225 W, respectively.

Figure 6.14 shows the evolution of the FWHM of the rocking curve of the (0002) AlN diffraction peak as a function of the P_{Al}, and gives an idea of the layer crystallinity. The increase of the P_{Al} leads to a decrease of the FWHM of the rocking curve, this means that the crystal quality is improved when growing the AlN with higher powers, the FWHM decreases from 10 to 4.9° for P_{Al} of 150 to 225 W, respectively.

This result recovers the value obtained in AlN grown at higher T_s (600°C) and lower P_{Al} (150 W) indicating that the kinetic energy of adatoms can be increased by both T_s and P_{Al}.

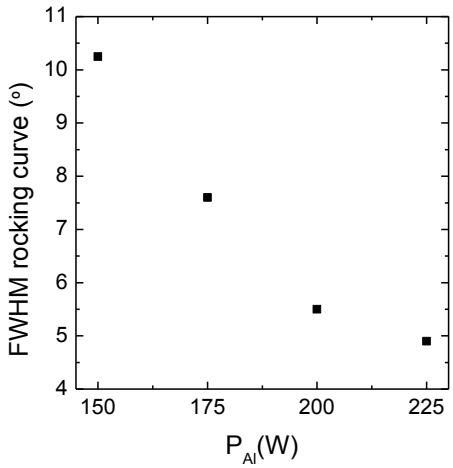

Figure 6.14. Evolution of the FWHM of the rocking curve as a function of the P_{Al} for the AlN layers.

The layer thickness of the set of samples under study has been estimated by XRR measurements. It increases from 95 nm to 180 nm when increasing the P_{Al} from 150 to 225 W. This clear trend is shown in Figure 6.15 where the AlN growth rate is evaluated as a function of the power applied to the aluminum target.

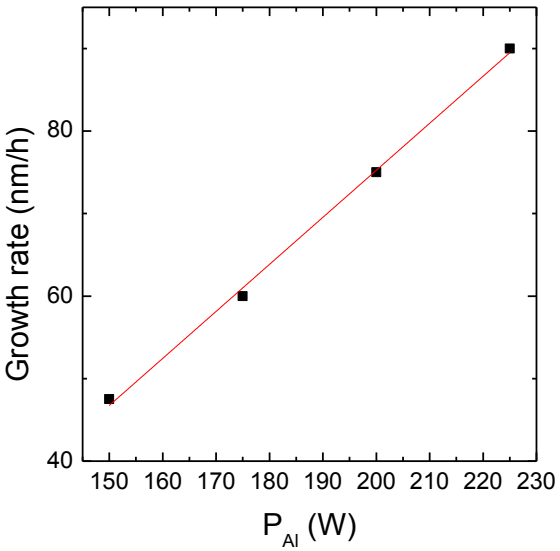

Figure 6.15. Evolution of the AlN growth rate with the power applied to the aluminum target.

Figure 6.16 shows the decrease of the RMS surface roughness when increasing the power applied to the aluminum target from 175 to 225 W, obtaining the minor (0.64 nm) RMS for the sample grown at 225 W.

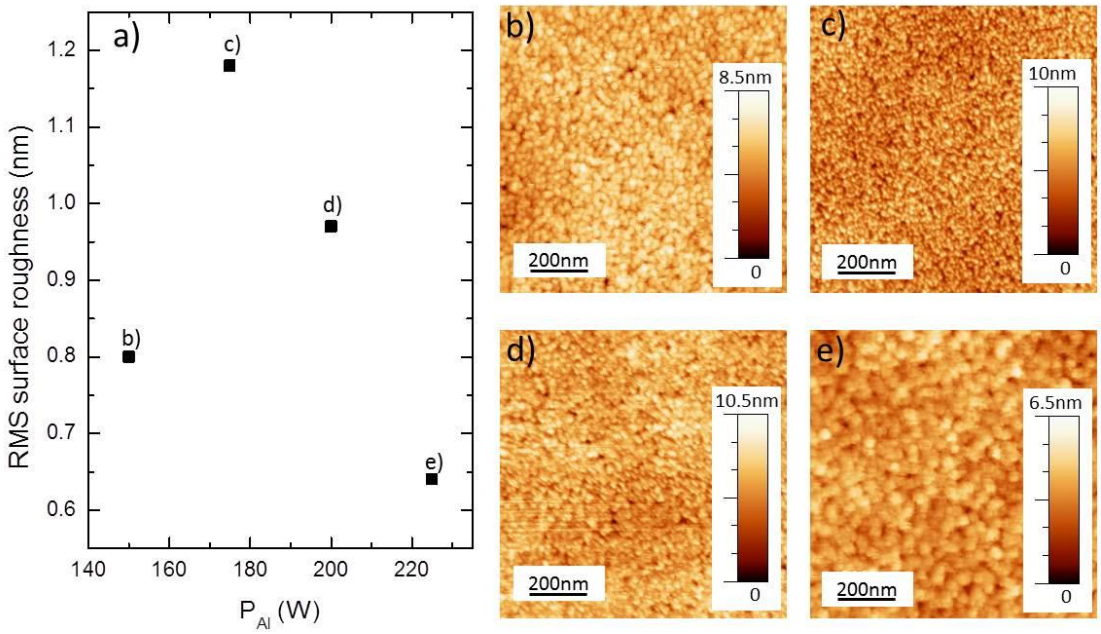

Figure 6.16. a) RMS surface roughness evolution as a function of the power applied to the aluminum target. 1×1 μm² AFM images of the AlN samples with different P_{Al} b) 150 W, c) 175 W, d) 200 W, e) 225 W.

6.3.1.3.2. Study of including an Al intermediate layer on the AlN properties

The effect of incorporating an Al intermediate layer has been studied by a set of four samples with different intermediate layer thicknesses. Higher Al thicknesses were discorded to be considered for this study taking into account the results obtained for AlN layers deposited at 600°C (see section 6.3.1.2.2). The Al and AlN layers were grown at T_s 450°C by using a DC voltage of 75 W and P_{Al} 225 W, respectively. The P_{Al} chosen for growing the AlN layer was 225 W because it presents the lowest FWHM of the rocking curve and the smallest RMS surface roughness, being the one with the best crystal quality.

Experimental results. Structural and morphological properties

Figure 6.17 shows the 2θ/ω HRXRD scans of the AlN samples grown at 225 W and 450°C with different Al intermediate layer thicknesses.

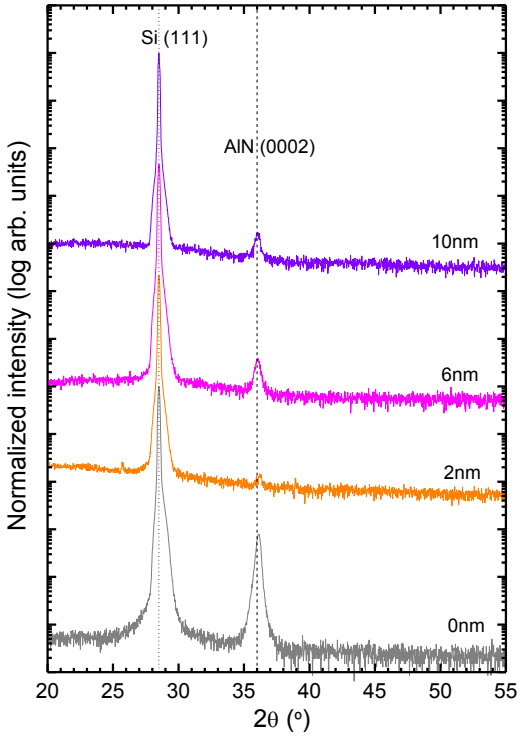

Figure 6.17. 2θ/ω scans of the AlN layers grown on p-Si (111) at 225 W with different Al intermediate layer thicknesses, the dash line corresponds to the AlN theoretical diffraction angle.

When including an Al intermediate layer of 2 nm the AlN peak is not clear, revealing a non-crystalline layer. But when increasing the intermediate layer thickness the AlN recovers the crystallinity. As in the previous case, a decrease in the diffraction peak intensity is shown.

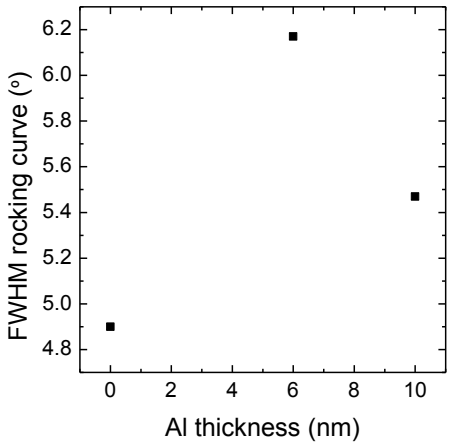

Figure 6.18. Evolution of the FWHM of the AlN rocking curve as a function of the Al intermediate layer thickness.

The FWHM of the rocking curve around the AlN (0002) diffraction peak increases when introducing the Al intermediate layer (see Figure 6.18).

Conclusions

There is no significant improvement of the AlN crystal quality with the introduction of an Al intermediate layer. The better crystal quality is achieved for the sample without intermediate layer which is the one with the lowest FWHM of the rocking curve.

From now on the AlN growth conditions for its use as buffer layer for $Al_xIn_{1-x}N$ growth on p-Si (111) are the following: T_s of 450°C and P_{Al} of 225 W.

6.3.2. Effect of an AlN buffer layer on the $Al_xIn_{1-x}N$ growth

Once the AlN buffer layer and the $Al_xIn_{1-x}N$ layer growth on p-Si (111) were optimized. The effect of the AlN layer thickness on the growth of the $Al_xIn_{1-x}N$ layer has been studied.

6.3.2.1. Deposition conditions

Five samples with different buffer layer thicknesses (0 – 25 nm) were grown. The AlN buffer layer and the $Al_xIn_{1-x}N$ layer were grown under the previous optimized conditions: the nitrogen flow rate and, sputtering pressure were kept at 6 sccm, and 0.47 Pa, respectively. The substrate temperature was fixed at 450°C. Particularly, for the growth of the AlN buffer layer the radiofrequency power applied to the aluminum target was of 225 W. And in the case of the $Al_xIn_{1-x}N$, the radiofrequency power applied to the aluminum target was of 150 W and the power applied to the indium target was of 40 W. A thickness of 80 nm for the $Al_xIn_{1-x}N$ layer was fixed in this study. This thickness was fixed taking into account further application of the structures to photovoltaic devices.

6.3.2.2. Experimental results

6.3.2.2.1. Structural and morphological properties

The structural properties of the samples were analyzed by HRXRD, 2θ/ω scans were performed and the results can be found in Figure 6.19. All the layers are crystalline and present wurtzite structure. Only the Si (111) and the $Al_xIn_{1-x}N$ (0002) and (0004) diffraction peaks appear in the scan pointing out that there is no phase separation in spite of the low thickness of the $Al_xIn_{1-x}N$. In addition, the appearance of the (0004) $Al_xIn_{1-x}N$ diffraction peak indicates higher layer quality. Also in the samples with higher AlN buffer layer thickness (15 and 25 nm) the AlN (0002) diffraction peak is clearly observed. The layer crystallinity was further analyzed by the rocking curve of the $Al_xIn_{1-x}N$ (0002) diffraction peak.

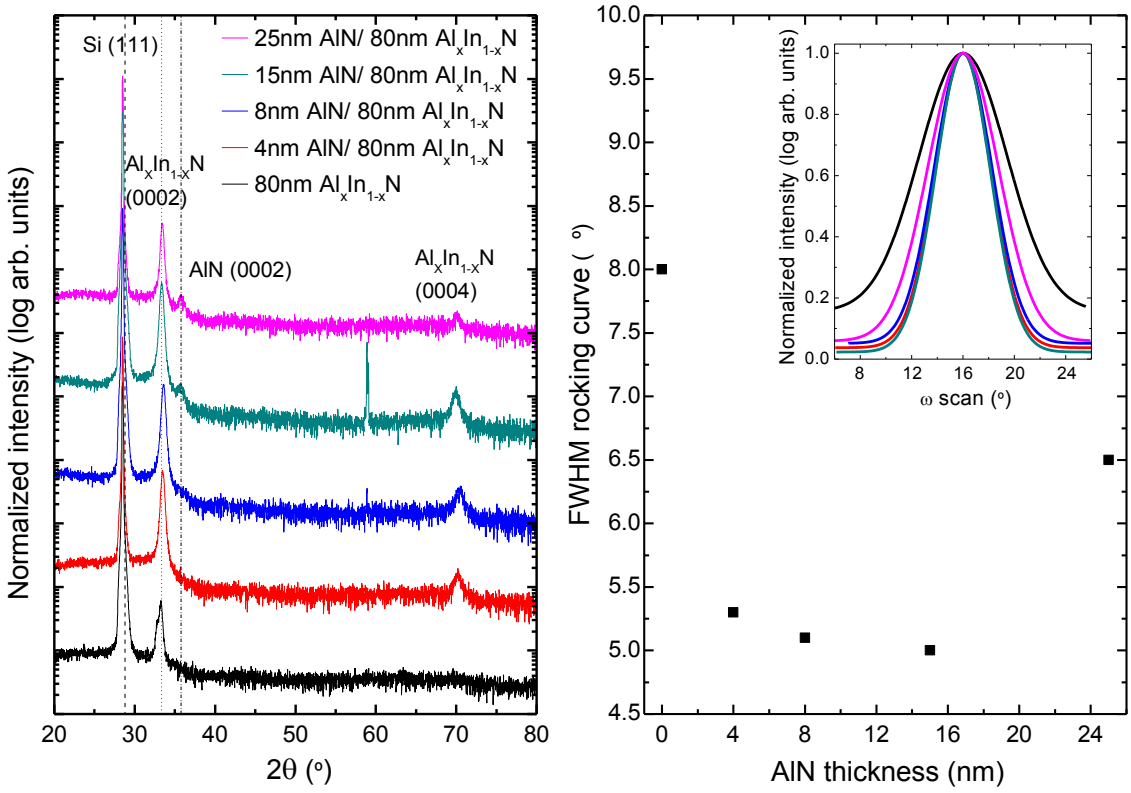

Figure 6.19. Left: 2θ/ω scans of the samples under study. Right: FWHM of the rocking curve as a function of the AlN thickness, inset: rocking curve of the samples under study.

The FWHM of the rocking curve decreases when increasing the buffer layer thickness up to 15 nm but it increases for higher buffer layer thicknesses (see

Figure 6.19 right). This reduction of the FWHM of the rocking curve is related with an increase of the crystalline quality of the layer.

The morphological properties of the layers were studied by AFM and FESEM. The evolution of the RMS surface roughness as a function of the AlN buffer layer thickness is shown in Figure 6.20. The RMS surface roughness is below 1.6 nm for all cases, although it increases when introducing AlN buffer layer up to 8 nm and then it tends to decrease. FESEM images reveals compact layers in all cases.

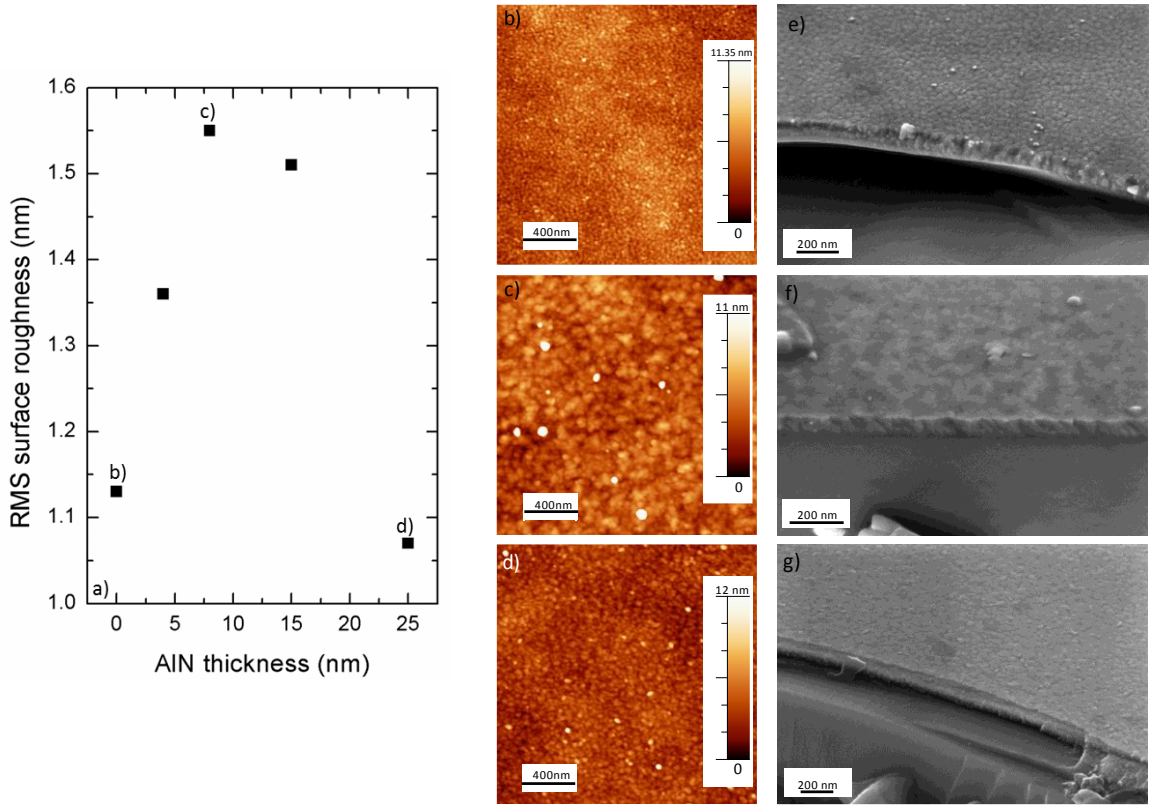

Figure 6.20. a) Evolution of the RMS surface roughness as a function of the AlN buffer layer thickness. AFM (2×2μm²) and FESEM images: b), e) $Al_xIn_{1-x}N$ layer without AlN buffer layer; c), f) 8 nm AlN buffer layer; d), g) 25 nm AlN buffer layer.

6.3.2.2.2. Optical properties

Low temperature PL measurements of the samples under study are shown in Figure 6.21 left, the PL energy peak is located at 1.8 eV for all the samples, this value is very similar to the obtained for thick layers without buffer layer under similar growth conditions (see Figure 6.5). Figure 6.21 right shows the evolution of the FWHM of the PL with the AlN buffer layer thickness, which decreases when

increasing the AlN layer thickness in good agreement with the enhancement in layer crystallinity shown by structural measurements.

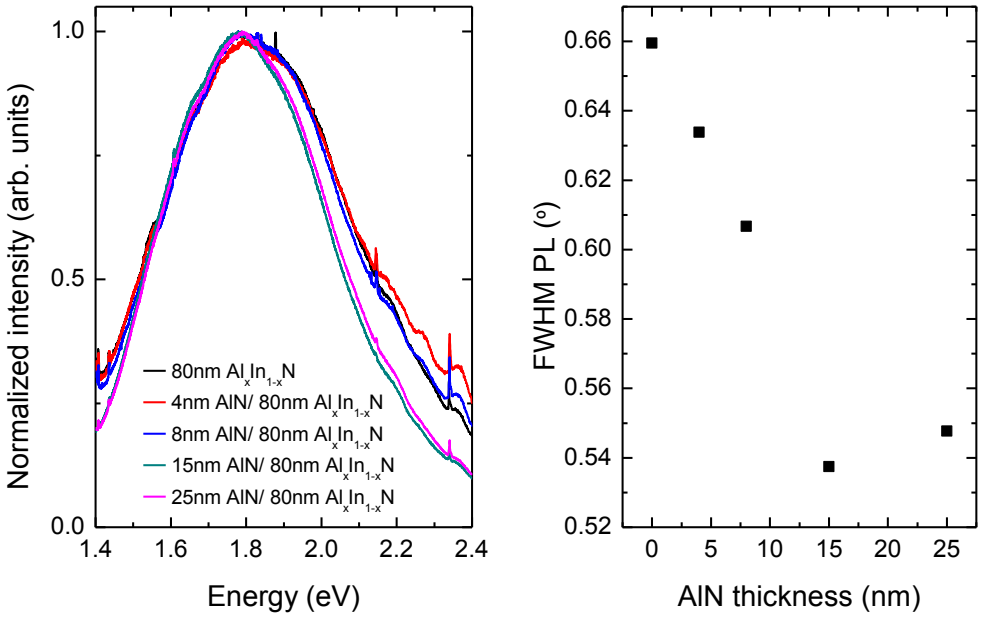

Figure 6.21. Left: low temperature PL measurements of the samples with different AlN buffer layer thickness. Right: Evolution of the FWHM of the PL with the AlN buffer layer thickness.

6.3.2.3. Conclusions

In this section, we have demonstrated that it is possible to grow high crystal quality $Al_xIn_{1-x}N$ on AlN buffer layer on p-Si (111) by RF sputtering.

- Crystalline layers with wurtzite structure highly oriented in the *c*-axis are obtained independently of the buffer layer thickness.
- The crystal quality is improved when the AlN buffer layer is in the 4 to 15 nm range.
- A minimum (5°) FWHM of the rocking curve of the $Al_xIn_{1-x}N$ (0002) diffraction peak is achieved for layers grown with 15 nm AlN buffer layer.
- All the samples present compact morphology with a RMS surface roughness around 1.3 nm.
- Low temperature PL emission at 1.8 eV is obtained, similar to the presented in thicker $Al_xIn_{1-x}N$ layers indicating homogeneous layers.

The layer that presents better crystal quality is the one grown with 15 nm of AlN buffer, it presents a FWHM of the (0002) AlN rocking curve of 5° and a FWHM of the PL of 0.54 eV with an RMS surface roughness of 1.5 nm.

Chapter 7

Growth of $Al_xIn_{1-x}N$ by RF sputtering at low temperature

7.1. Introduction

In this Chapter, it is described the growth of $Al_xIn_{1-x}N$ layers on different substrates (sapphire, p-Si (111) and glass) at low temperature, in the range of room temperature to 100°C.

The enhanced kinetic energy of the constituent ions given by the power applied to the targets allows the growth at low temperature deposition by the sputtering technique. This advantage of sputtering over other growth techniques was explained in Chapter 3. As explained in previous Chapters the $Al_xIn_{1-x}N$ layers present a wide range of applications and the possibility of growing them at low substrate temperatures makes feasible the use of flexible substrates such as plastics, which increases the applicability of this material.

A few works related to the growth of $Al_xIn_{1-x}N$ layers at low substrate temperatures (< 300°C) have been previously reported [AfDI16a, BGMM14, GOKT07, HDDS10, YeWL09]. In particular, Afzal *et al.* studied the influence of the substrate temperature (from RT to 300°C) on the properties of $Al_xIn_{1-x}N$ layers grown on p-Si (111) under a mixture of Ar and N_2 plasma. It should be remarked that for the

$Al_xIn_{1-x}N$ grown at RT they do not achieve crystalline $Al_xIn_{1-x}N$ layers, in this Chapter we demonstrate the possibility of growing crystalline $Al_xIn_{1-x}N$ layers on sapphire, p-silicon (111) and glass substrates even at RT.

7.2. Deposition conditions

In this Chapter, $Al_xIn_{1-x}N$ samples were deposited on sapphire, p-doped Si (111) and glass substrates using the reactive sputtering described in Chapter 3. 2" confocal magnetron cathodes of pure In (4N5) and pure Al (5N) were co-sputtered using pure nitrogen (6N) as reactive gas for the formation of the $Al_xIn_{1-x}N$ layer.

The substrates were chemically cleaned in organic solvents and once they were loaded to the sputtering chamber, they were outgassed for 30 min at 100°C above the growth temperature, then they were cooled down to the growth temperature. The targets and substrate were pre-sputtered with pure Ar (5N) plasma to remove surface contaminants. During the deposition of $Al_xIn_{1-x}N$, the nitrogen flow rate and sputtering pressure were kept at 14 sccm, and 0.47 Pa, respectively. The RF power applied to the indium and aluminum target was kept constant at 40 W and 150 W, respectively. The sputtering time for all the samples is of 4 h.

The $Al_xIn_{1-x}N$ samples were grown at room temperature and at 100°C to study the growth at low temperature.

7.3. Experimental results

7.3.1. Structural and morphological properties

The structural properties of the $Al_xIn_{1-x}N$ layers grown on the different substrates at RT and 100°C were studied by HRXRD, this analysis confirms that in all the substrates and at both growth temperatures the $Al_xIn_{1-x}N$ layers are crystalline. A comparison of the HRXRD patterns of the $Al_xIn_{1-x}N$ films deposited on different substrates is shown in Figure 7.1. Only the (0002) and (0004) diffraction peak of the $Al_xIn_{1-x}N$ layer, the (0006) diffraction peak of sapphire, the (111) diffraction peak of silicon, depending on the substrate, are detected. The peak that appears at

~60° in the sample grown at 100°C on silicon corresponds to the silicon (222) diffraction peak.

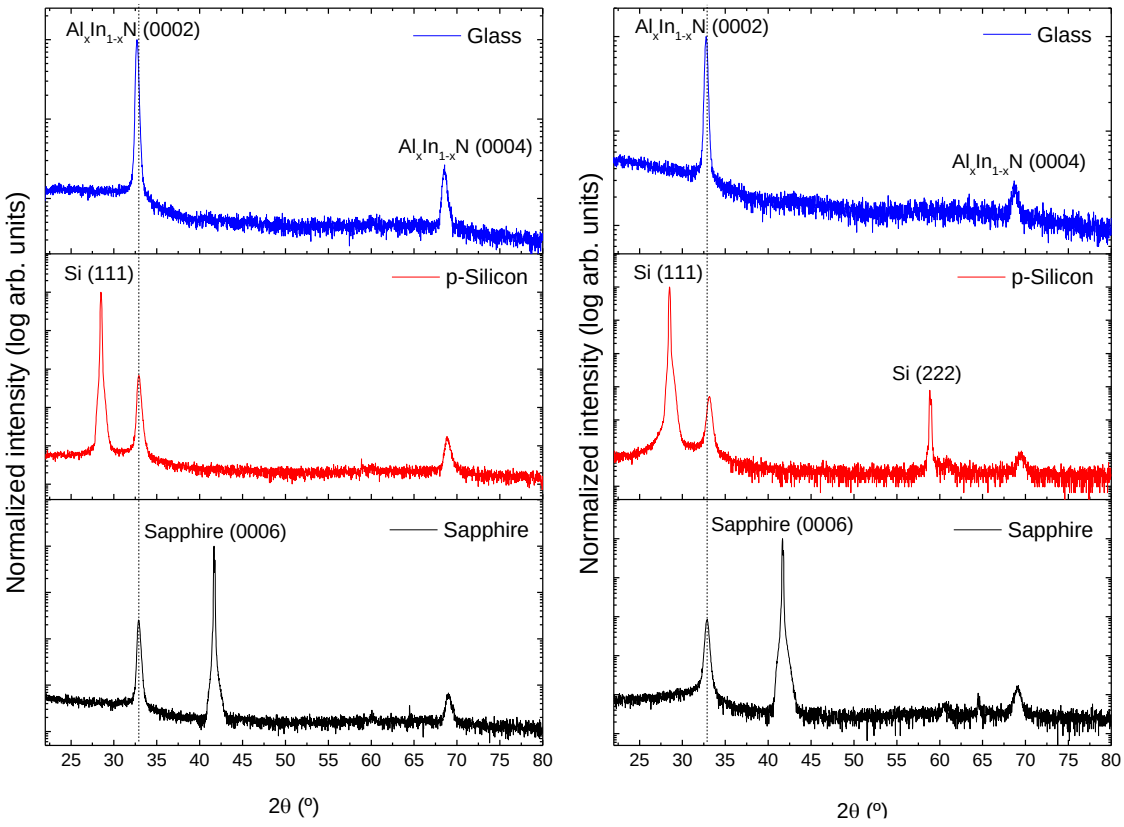

Figure 7.1. 2θ/ω scans of the Left: Room temperature and Right: 100°C $Al_xIn_{1-x}N$ layers grown on different substrates

The layer composition can be extracted from these measurements by using the Vegard's law (Eq. (2.2)) and assuming fully relaxed layers, a 37% of Al is obtained for all $Al_xIn_{1-x}N$ layers grown on sapphire and silicon at low temperature, this value is similar to the one obtained for $Al_xIn_{1-x}N$ layers grown at 300°C by WDX measurements pointing out to almost fully relaxed layers when growing at low temperatures. However, the Al composition obtained for glass substrates is around a 33% (see Table 7.1), the difference observed in the alloy composition is attributable to the lack of diffraction peak related to the substrate that leads to higher errors.

A variation in the intensities of $Al_xIn_{1-x}N$ diffraction peaks on different substrates can be noticed in Figure 7.1. The grain size estimated by Eq. (4.2) lies in the range between 20 and 25 nm for all the studied substrates at low growth temperature. Particularly, in the case of sapphire substrate it increases from 25 to 53 nm when

increasing the growth temperature from RT to 300°C, the increase of the grain size with the temperature is related with an increase of the adatom mobility that facilitates the growth and coalescence of the islands as reported by Afzal *et al.* for $Al_{0.14}In_{0.86}N$ layers grown on p-Si (111) [AfDI16a].

Table 7.1. Growth conditions, structural and morphological properties of the layers grown at low temperature: Aluminum content (x) extracted from HRXRD for samples L1-L6 and from WDX for S5 and M6, FWHM of the rocking curve of the (0002) $Al_xIn_{1-x}N$ diffraction peak, RMS surface roughness extracted from AFM measurements and layer thickness extracted from FESEM measurements.

	Substrate	**T_s (°C)**	**Al content x**	**FWHM rocking curve (°)**	**RMS (nm)**	**Thickness (nm)**
L1	Sapphire	RT	0.37	6.5	2.5	510
L2	p-Silicon		0.37	6.4	1.6	485
L3	Glass		0.32	5.8	2.0	-
L4	Sapphire	100	0.36	6.0	2.7	345
L5	p-Silicon		0.39	6.7	2.9	446
L6	Glass		0.34	5.2	2.4	-
S5[1]	Sapphire	300	0.36	1.4	5.8	530
M6[2]	p-Silicon		0.37	3.3	3.1	840

A further analysis of the rocking curve of the (0002) $Al_xIn_{1-x}N$ diffraction peak revealed that the increase in the substrate temperature from RT to 300°C leads to a decrease of the FWHM of the rocking curve, the extra energy supplied to the adatoms by the substrate temperature allows the enhancement of the crystal quality that cannot be achieved just with the kinetic energy supplied by the sputtering of the targets. The FWHM of the rocking curve drops by a factor of ×4.6 in the case of sapphire and ×2 in the case of silicon when increasing the growth temperature from RT to 300°C. On the other hand, for low substrate temperature, the $Al_xIn_{1-x}N$ layer grown on glass presents the lowest FWHM of the rocking curve among all the substrates used. This fact can maybe be due to the amorphous nature of the glass substrate, so that the $Al_xIn_{1-x}N$ layer does not have to compensate the difference in lattice parameter (see Table 7.1).

[1] See Chapter 5
[2] See Chapter 6

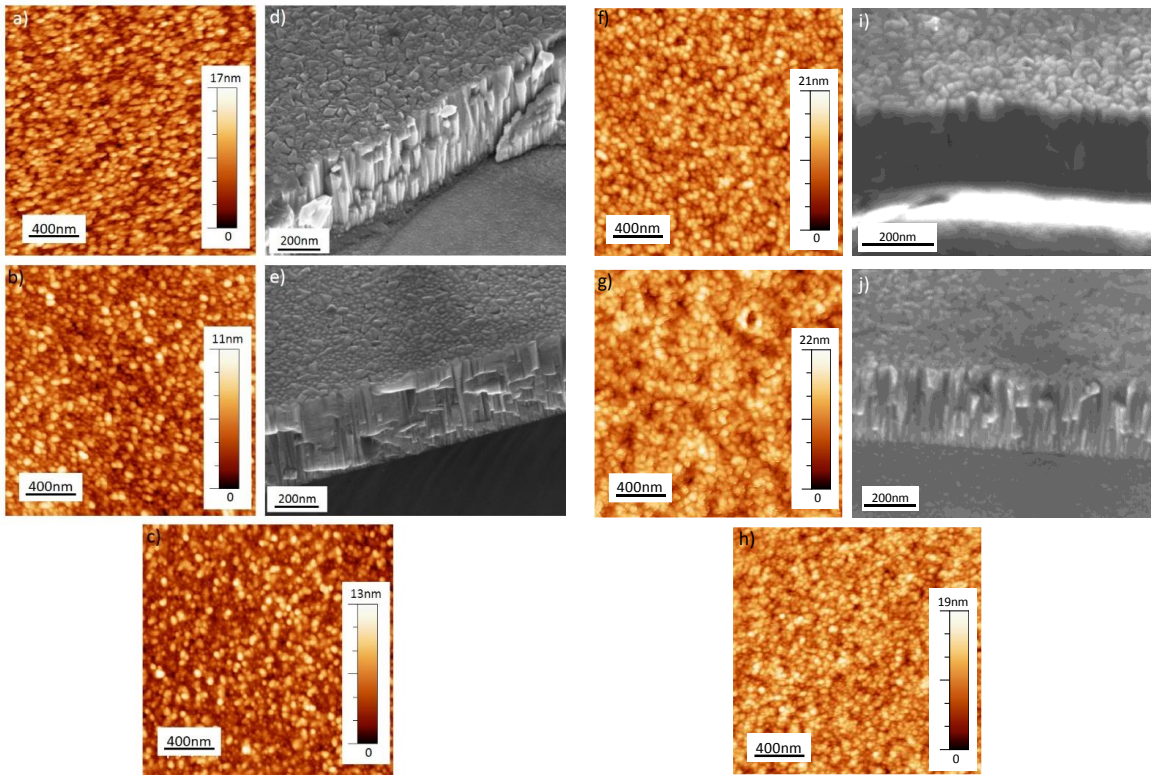

Figure 7.2. 2×2 μm² AFM and FESEM images of: a) and d) RT $Al_xIn_{1-x}N$ layer grown on sapphire; b) and e) RT $Al_xIn_{1-x}N$ layer grown on p-silicon; c) RT $Al_xIn_{1-x}N$ layer grown on glass; f) and i) 100°C $Al_xIn_{1-x}N$ layer grown on sapphire; g) and j) 100°C $Al_xIn_{1-x}N$ layer grown on p-silicon; h) 100°C $Al_xIn_{1-x}N$ layer grown on glass.

The morphological properties of the layers were studied by AFM and FESEM techniques. The surface roughness of the $Al_xIn_{1-x}N$ layers increases when increasing the substrate temperature for all substrates, due to the increase in the kinetic energy, and thus the mobility, of the sputter atoms which leads to more compact layers with higher surface roughness, this has been also observed by [AfDI16a]. When comparing the RMS of the $Al_xIn_{1-x}N$ layers grown on the different substrates at room temperature, the highest RMS is achieved for the $Al_xIn_{1-x}N$ layer grown on sapphire and the lower for the one grown on silicon. However, at 100°C, the highest RMS is the one of silicon and the lowest the one of glass. The RMS surface roughness values appear in Table 7.1. Figure 7.2 (a, b, c, f, g, h) show the 2×2 μm² AFM images of the $Al_xIn_{1-x}N$ layers grown on sapphire, p-silicon and glass at RT and 100°C, respectively.

Figure 7.2 (d, e, i, j) show the FESEM images of the layers grown on sapphire and p-silicon at RT and at 100°C, respectively. The layers grown on sapphire and

p-silicon show a closely-packed columnar morphology for both temperatures (RT and 100°C), as it has been pointed out in previous Chapters, to improve the layer morphology and achieve compact layers it is needed to increase the growth temperature up to 450°C for $Al_xIn_{1-x}N$ grown on sapphire (see Chapter 5) and to 300°C for layers grown on p-Si (111) (see Chapter 6). The $Al_xIn_{1-x}N$ layers grown on glass were difficult to observe by FESEM because it was hard to cleavage the sample due to the low thickness of the substrate that makes the sample very fragile.

7.3.2. Optical properties

Figure 7.3 left shows the square of the absorption coefficient estimated by Eq. (4.7) as a function of the photon energy and in the inset RT optical transmittance of the $Al_xIn_{1-x}N$ layer grown on sapphire and glass substrates at room temperature. The band gap energy has been estimated to be 2.34 and 2.37 eV for the $Al_xIn_{1-x}N$ grown on sapphire and glass respectively. In the case of the layers grown at 100°C (see Figure 7.3 right) the band gap energy has been estimated to be 2.44 and 2.46 eV for sapphire and glass substrates, respectively. In the case of 300°C a band gap energy of 2.03 eV has been calculated.

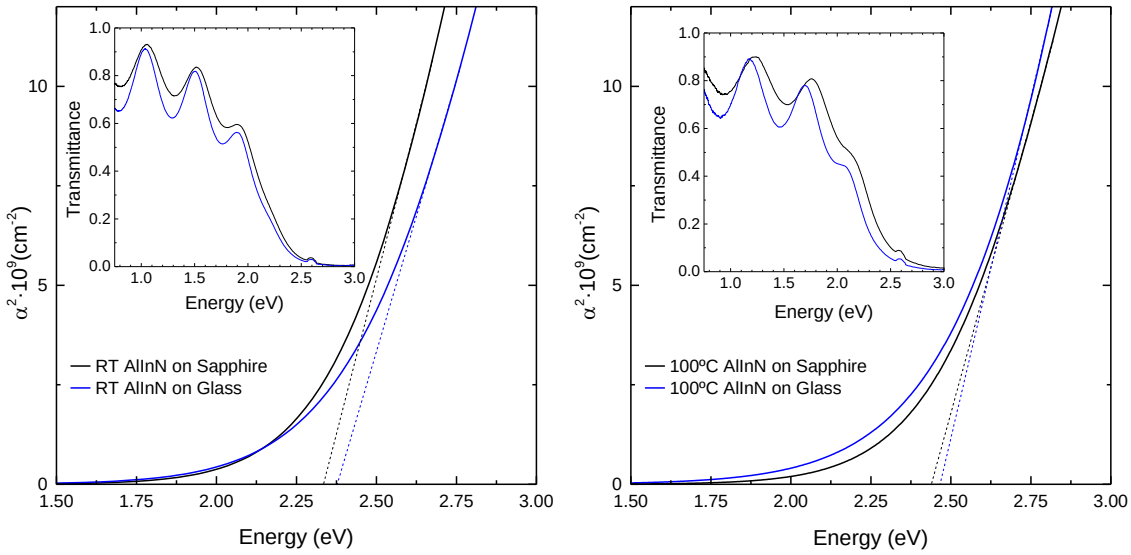

Figure 7.3. Square of the absorption coefficient as a function of the photon energy and inset RT transmittance of the $Al_xIn_{1-x}N$ layers grown on sapphire and glass: left) at RT, right) at 100°C.

The obtained band gap difference between the samples deposited at low (RT and 100°C) and high (300°C) substrate temperature can be mainly attributed to the Burstein-Moss effect, which establishes a strong dependence of the band gap energy and the carrier concentration, specially for the range of residual carrier concentration expected in the layers, in the range of 10^{20} cm^{-3}. The strain state of the layers (relaxed at low T_s but under compressive strain at high T_s) can reinforce the band gap energy shift induced by Burstein-Moss effect. It has been calculated the band gap dependence with the strain ($\Delta E_g/\Delta\varepsilon_{zz}$) for the sample S5, by using the Hamiltonian equation [SASC97] and the deformation potentials for InN reported in [VuMe03]. For sample S5 the ΔE_g has been calculated to be 70 meV.

The absorption broadening (ΔE) decreases when increasing the T_s it being of 288 and 154 meV for the layers grown on sapphire at RT and 300°C, respectively (see Table 7.2). This can be due to a reduction in alloy inhomogeneities for layers grown at higher temperatures.

Table 7.2. Optical properties of the layers grown at low temperature.

	Substrate	**T_s (°C)**	**Al content x_{HRXRD}**	**E_g (eV)**	**ΔE (meV)**
L1	Sapphire	RT	0.37	2.33	288
L3	Glass		0.32	2.37	345
L4	Sapphire	100	0.36	2.44	289
L6	Glass		0.34	2.46	388
S5[1]	Sapphire	300	0.36	2.03	154

7.4. Conclusions

In this Chapter we have shown the possibility of growing polycrystalline $Al_xIn_{1-x}N$ at low growth temperatures, this makes possible the growth on flexible substrates and on structures that require low temperature processing.

- Polycrystalline layers oriented in the *c*-axis and with wurtzite structure even at RT have been achieved. The FWHM of the rocking curve is reduced when increasing the growth temperature. The Al content estimated for the

[1] See Chapter 5

layers grown at low temperature is similar to the one obtained by WDX measurements for $Al_xIn_{1-x}N$ layers grown at 300°C (37%) which points out that $Al_xIn_{1-x}N$ layers grown at low growth temperature are almost fully relaxed.

- The layers grown on sapphire and p-Si (111) at low temperatures show a closely-packed columnar like morphology with low RMS surface roughness (<3 nm). This morphology evolves to compact at growth temperatures of 450°C for $Al_xIn_{1-x}N$ grown on sapphire (see Chapter 5) and 300°C for layers grown on p-Si (111) (see Chapter 6). Nevertheless, a higher RMS surface roughness is obtained for layers grown at high temperature, probably due to an increase of the grain size with the temperature.

- The layers present a band gap energy of around 2.4 eV for glass and sapphire substrates and for both growth temperatures (RT and 100°C). However, there is a red shift of the band gap energy when increasing the growth temperature from RT to 300°C, which can be mainly attributed to the Burstein-Moss effect that has a strong influence on the band gap energy for residual carrier concentrations in the range of 10^{20} cm^{-3}, as is in this case.

Chapter 8

Applications of $Al_xIn_{1-x}N$ semiconductor

This Chapter focuses on the applications that we have studied for the developed $Al_xIn_{1-x}N$ layers on different substrates.

As explained in the introduction (Chapter 1), $Al_xIn_{1-x}N$ is a wide range direct band gap semiconductor, its band gap energy can be tuned with the composition. This in addition with the unique properties of III-nitrides make them interesting for its application in a wide range of fields.

The use of sputtering for the development of this kind of devices is interesting because it is a low cost technique that allows the deposition at low temperatures and thus makes possible the use of flexible substrates. However, this technique presents disadvantages such as the polycrystalline nature of the layers and their high residual impurity concentration.

$Al_xIn_{1-x}N$ layers deposited on sapphire have been processed into photoconductors, while the $Al_xIn_{1-x}N$ layers grown on p-Si have been processed into solar cells. Finally, $Al_xIn_{1-x}N$ layers grown at low temperature on optical fiber have been used as surface plasmon resonance (SPR) sensors.

The first part of this Chapter (section 8.1) has been reported as a journal paper in Physica Status Solidi (a) [NJMG17], while the last part (section 8.3) has been published in Sensor and Actuators, B: Chemical [NEMG16].

8.1. $Al_xIn_{1-x}N$ photoconductors

This section describes the processing of $Al_xIn_{1-x}N$ layers grown on sapphire into photoconductors. First, a brief introduction of photoconductors is done, then it is described the device processing and finally the photoconductors are analyzed.

8.1.1. Introduction

8.1.1.1. Photoconductors

A photodetector is an optoelectronic device that converts the absorbed optical energy into electrical energy. Photoconductors are the simplest semiconductor photodetectors; their operation is related to a change in the device conductivity induced by light due to the absorption of electromagnetic radiation [YuMa03]. When light is absorbed the electrical conductivity is increased due to an increase of the number of free electrons and electron-hole pairs. The light that reaches the semiconductor must have enough energy to produce a band to band transition or to excite the impurities within the band gap. When a bias voltage and a load resistance are used in series with the semiconductor, a voltage drop across the load resistance can be measured. This voltage varies with the change in electrical conductivity of the material as the current through the circuit is modified [SaTe91].

8.1.1.2. Responsivity, gain and response time

Some important parameters of photoconductors are the responsivity (R), the gain and the response time [SaTe91].

The responsivity, for a specific wavelength, relates the output photo generated current (I_{ph}) to the optical incident power (P_{opt}) and it is measured in A/W.

When a photoconductor generates more than an electron-hole pair per incident electron, they present internal gain, this is due to the difference between the carrier

recombination lifetime and the transit time. When the recombination lifetime is higher than the transit time the gain is greater than one, leading to amplification.

The response time of a photoconductor is the time that the photoconductor needs to change its resistivity as a response to an optical input. The transit time spread and resistance-capacitance time constant are limiting factors for the speed of operation of the semiconductor photodetectors. The transit time spread, is the time that takes a carrier to move from one side to another in the photodetector. While the resistance and capacitance time constant serves to integrate the current at the output of the detector, this is to lengthen the impulse-response function.

There is extensive work on photoconductors based on (Al)GaN materials [LGWC08, MMGI97, PMSC02, StKB95, WHMS97, WZKS96, YuMa03], but, as far as we know, there is no report on $Al_xIn_{1-x}N$ photoconductors.

In this section, the performance of low cost $Al_{0.39}In_{0.61}N$ photoconductors fabricated on RF-sputtered layers is described.

8.1.2. Device fabrication

The optimization of the $Al_xIn_{1-x}N$ layers deposited on sapphire by RF sputtering is described in Chapter 5. The layers under study were grown at 450°C due to the good properties shown in Chapter 5 such as the compact structure and low RMS surface roughness (~2 nm), the relatively low carrier concentration ($1.5 \cdot 10^{20}$ cm^{-3}) and its high electron mobility (μ=8.8 cm^2/Vs). The power applied to the In and Al targets was 40 W and 150 W, respectively, and the layers were grown using pure nitrogen plasma. The deposition time was set to 42 and 150 minutes to achieve samples with thickness of 80 and 350 nm, respectively.

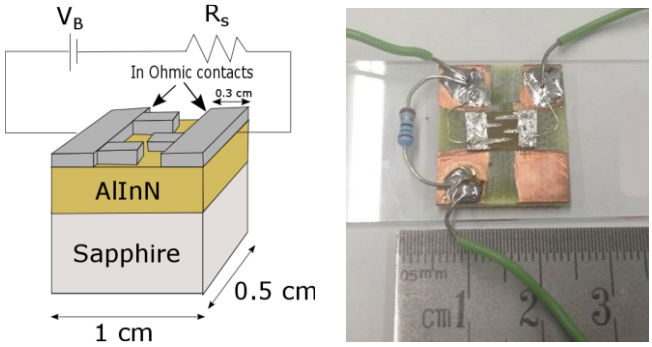

Figure 8.1. Left: $Al_xIn_{1-x}N$ photoconductor structure. Right: Real device, example of an $Al_xIn_{1-x}N$ photoconductor.

Once the layers were grown, they were structurally, morphologically and optically characterized with the techniques described in Chapter 4. Then they were cut into 1×0.5 cm^2 bars, and they were processed into devices using indium contacts with an interdigitated pattern as ohmic contact. A soldering iron was used to form the contacts with molten indium. The distance between fingers and the finger thickness was 1 mm in both cases. Figure 8.1 shows a scheme and a real image of the developed photoconductor.

The ohmicity of the contacts was analyzed by current-voltage (I-V) characteristics. Resistances of 1.0 kΩ and 120 Ω were measured for devices fabricated on 80 and 350 nm thick layers, respectively. The I-V characteristic measured under dark conditions are shown in Figure 8.2. The linearity of the I-V curve confirms the ohmic behavior of the contacts for all samples.

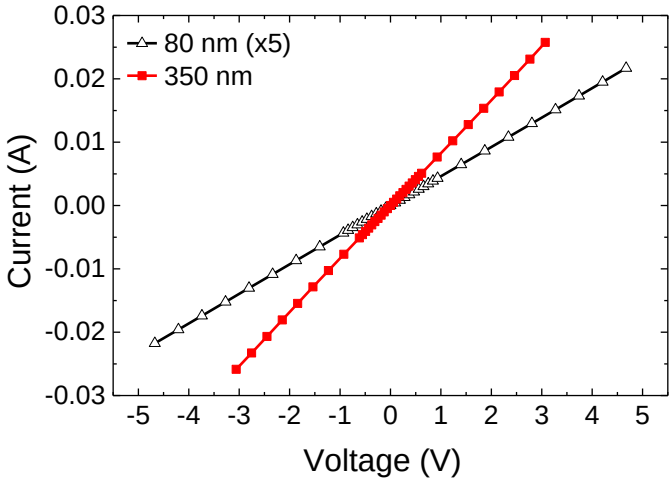

Figure 8.2. I-V characteristics of the samples under study showing the linear relationship between applied voltage and the measured current. The data of the 80 nm-thick sample appears multiplied by 5.

8.1.3. Experimental setups

The photoconductor characterization was made by connecting the photoconductor with a 5 V bias source and in series with a load resistance (R_s) which was chosen to be significantly smaller than the device resistance (see Figure 8.1). The change in resistivity of the device under illumination was probed by measuring the variation of the voltage drop across the load resistance. The spectral response was measured

using a 20 W halogen lamp and an Oriel Instruments Cornerstone 130 1/8m monochromator (see Figure 8.3).

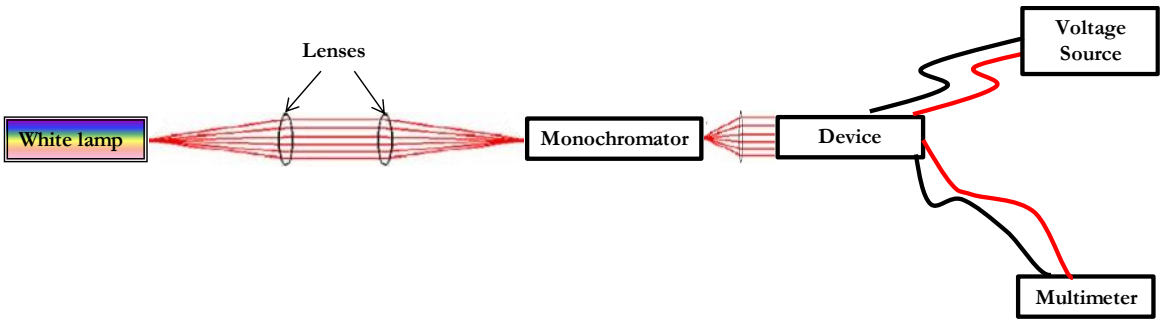

Figure 8.3. Experimental setup for measuring the change in resistivity as a function of the incident wavelength.

Figure 8.4 shows the experimental setup used for measuring the variation of responsivity as a function of the impinging optical power. Two different laser sources (GaN laser diode emitting at 405 nm and HeNe laser emitting at 633 nm) focused sequencially on the device were used as the excitation source.

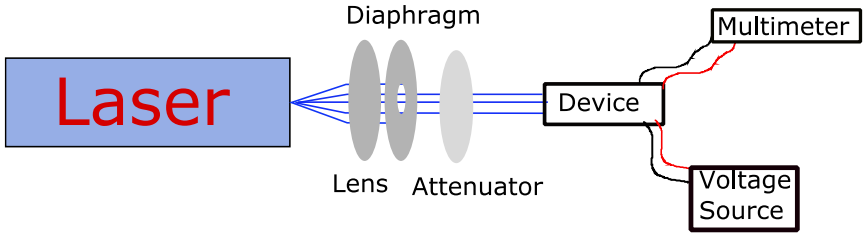

Figure 8.4. Experimental setup for measuring the responsivity as a function of the impinging optical power.

In all cases the photocurrent was recorded after keeping the samples in the dark for a long time (>12 h), and always from low optical power to high optical power and from long wavelengths to short wavelengths, to minimize persistent photoconductivity effects. The photocurrent measurement was corrected by the spectral response of the lamp taking the dependence of the responsivity on the optical power into account.

8.1.4. Experimental results

8.1.4.1. Layer properties

Prior to the device fabrication the structural, morphological and optical properties of the $Al_xIn_{1-x}N$ layers were measured. Figure 8.5 shows the HRXRD measurements of the layers. In the analyzed $2\theta/\omega$ range, only the (0002) and (0004) diffraction peaks of $Al_xIn_{1-x}N$ and the (0006) line of the sapphire substrate are observed, which implies that phase separation is negligible. The layers present (0001)-oriented wurtzite structure. The shoulders that appear around the $Al_xIn_{1-x}N$ diffraction peaks are maybe related with In_2O_3 formed in the surface of the layer. The aluminum mole fraction can be calculated using Vegard's law (Eq. (2.2)) and assuming fully relaxed layers from the HRXRD measurements, the calculated aluminum composition is 0.39.

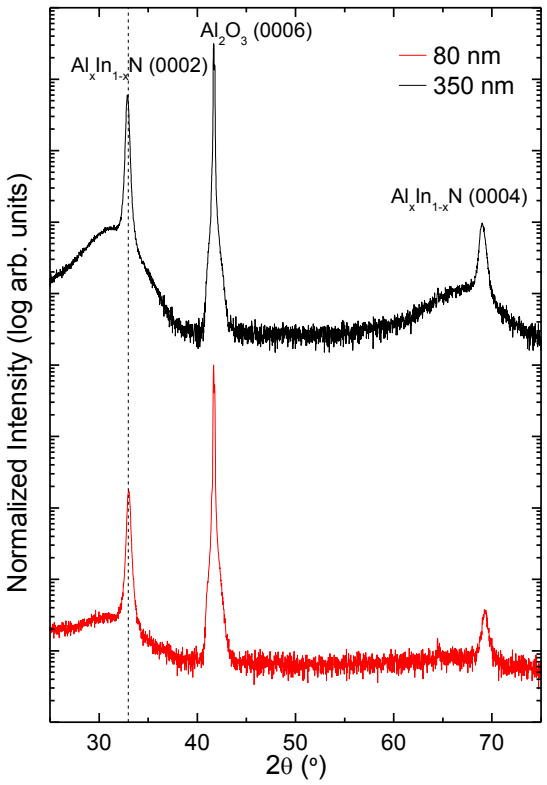

Figure 8.5. XRD $2\theta/\omega$ scan of the 80 and 350 nm thick $Al_xIn_{1-x}N$ samples deposited on c-sapphire.

AFM measurements were used for studying the surface morphology. A RMS surface roughness of 0.4 ± 0.1 nm was measured in 2×2 μm^2 images for both samples, with a slight increase of the grain size for the thicker layer (see Figure 8.6).

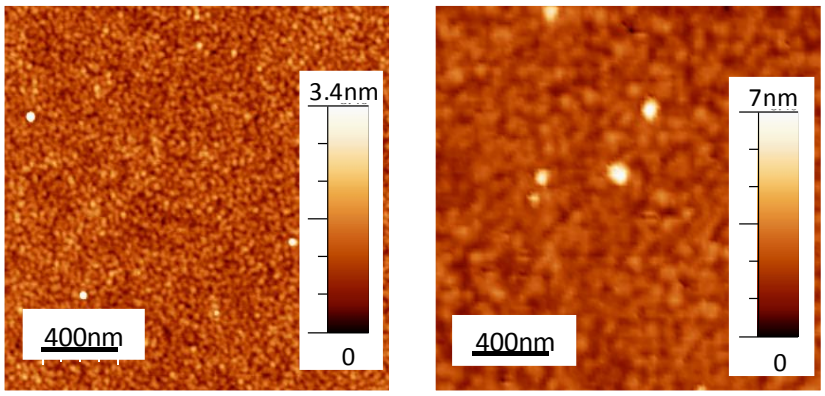

Figure 8.6. AFM images of the: left) 80 nm thick and right) 350 nm thick $Al_xIn_{1-x}N$ layers.

Figure 8.7 shows the optical transmittance spectrum of the thickest layer (350 nm). The band gap energy has been estimated as explained in Chapter 4 by the sigmoidal approximation shown in Eq. (4.7). The value obtained for the band gap energy is of ~ 2.15 eV (576 nm), which is consistent with a blue-shift of the expected band gap due to a Burstein-Moss effect, as the expected carrier concentration in the layers is in the range of $1.6 \cdot 10^{20}$ cm^{-3} [NVMM16]. This band gap energy is in agreement with other results in $Al_xIn_{1-x}N$ layers grown by magnetron sputtering and presenting similar alloy composition [HCFG10]. An absorption band edge broadening of 0.3 eV has been estimated, broader than the 0.1 eV typically obtained for InN [NVMM16].

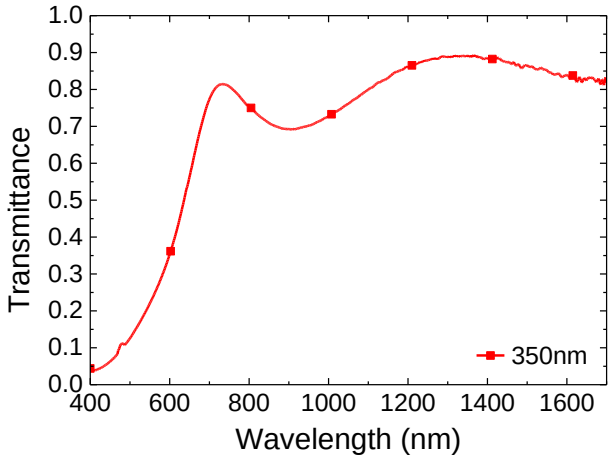

Figure 8.7. Room temperature transmittance spectra of the 350 nm thick sample.

8.1.4.2. Device characterization

Once the layers have been characterized, they were processed into devices and the device properties were studied.

The responsivity as a function of the impinging optical power was measured. The results are shown in Figure 8.8. The dependence of the responsivity on the optical power can be described by $R \propto P_{opt}^{-\gamma}$ both for excitation at 405 nm (above the band gap) and at 633 nm (below the band gap). The γ parameter is in the range of 0.79 to 0.96, depending on the sample, in agreement with data in AlGaN-based photoconductors [MMGI97].

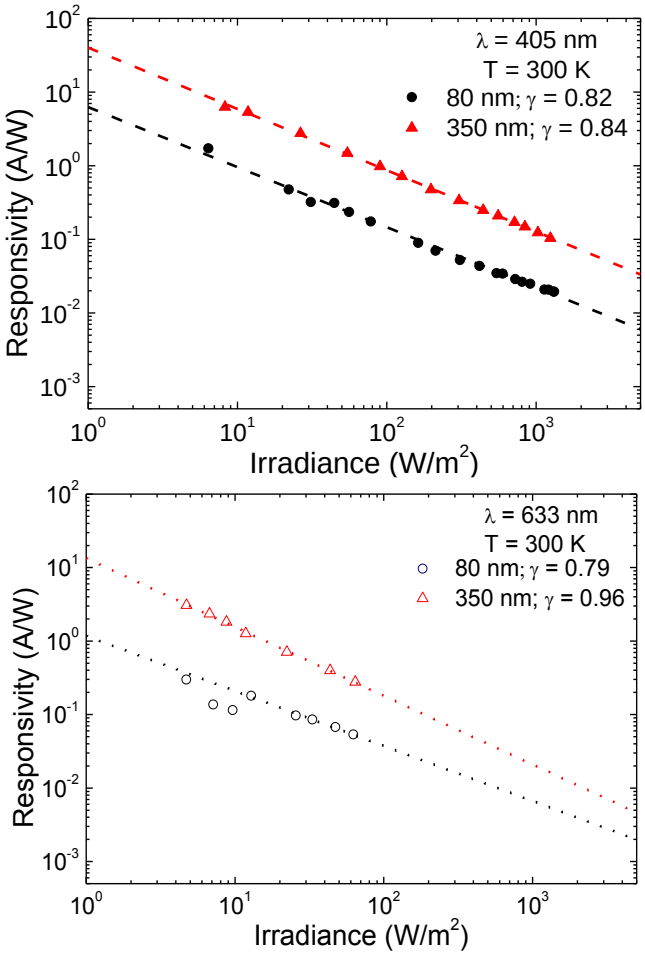

Figure 8.8. Responsivity as a function of the optical power for all the samples under study: Top: using a 405 nm incident wavelength and down: using a 633 nm incident wavelength.

For low irradiance, the devices present gain even for excitation energy below the band gap. When the incident wavelength is of 405 nm, at an irradiance of 10 W/m^2 the gain is of 3.1 and 22 for the 80 and 350 nm thick layers, respectively. These values of gain are lower than the ones obtained for MOVPE GaN photodetectors, Muñoz *et al.* achieved gain values of 100 for irradiances at energies below the band gap and with an optical incident power of 10 W/m^2 [MMGI97]. This difference can be attributed to the lower grain size and higher defect concentration expected in the $Al_xIn_{1-x}N$, leading to a reduction in the carrier recombination lifetime. The distance between contacts has to be also taken into account in this comparison.

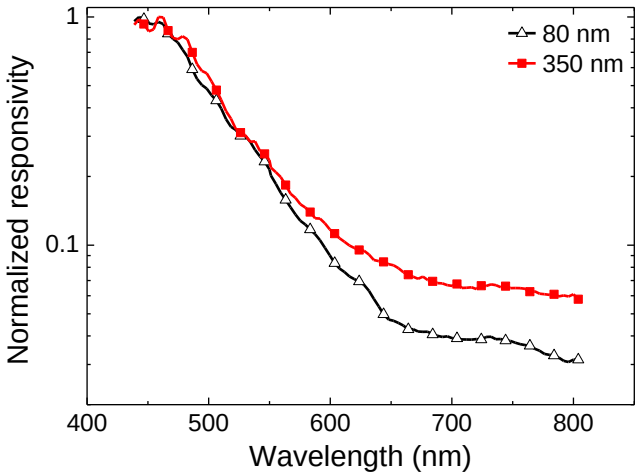

Figure 8.9. Spectral response of photoconductors fabricated on $Al_xIn_{1-x}N$ layers with different thicknesses.

The spectral response of the devices is shown in Figure 8.9. The responsivity decays smoothly below the band gap. This is explained by the presence of alloy inhomogeneities [PMSC02] and traps associated to the grain boundaries [BPGH99]. The contrast between the responsivity at wavelengths above and below band gap can be larger than one order of magnitude, which compares favorably with AlGaN photoconductors [MoOC03]. In addition, it is observed that the absorption maximum is well above the band gap. This blue shift of the photoresponse might be related with the high carrier concentration, due to the Burstein-Moss effect [LGWC08].

Finally, the evolution of the sample conductivity in the dark after being illuminated (photoconductivity decay time) has been studied, this is shown in Figure 8.10. At time = 0 the illumination is switched off. The decay is slow (hours)

and strongly non-exponential. This phenomenon is known as persistent photoconductivity and it is generally associated to carrier trapping at the grain boundaries [MMGI97, MoOC03].

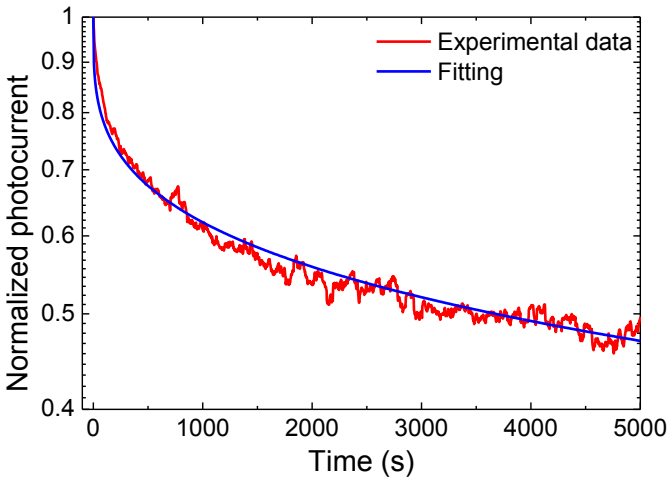

Figure 8.10. Photoresponse decay of the 350 nm-thick $Al_xIn_{1-x}N$ photoconductor at room temperature. The blue line is a fit of the experimental data to Eq. (8.1).

The experimental values can be fitted to a stretched exponential function, Eq. (8.1):

$$I_{ph}\ t\ = I_{ph}\ 0\ \cdot e^{\left(\frac{-t}{\tau}\right)^{\beta}} \tag{8.1}$$

where $I_{ph}(0)$ is the value of the photocurrent when the light is switched off, τ is the decay time constant and β is the decay exponent. The obtained values of the fitting parameters ($\tau = 13400$ s and $\beta = 0.28$) are in agreement with values obtained for AlGaN photoconductors grown by MBE [LGWC08].

8.1.5. Conclusions

In this section, it has been demonstrated the possibility of processing the $Al_xIn_{1-x}N$ layers grown on sapphire by RF sputtering into photoconductors.

- Two devices with different layer thickness have been studied. The layers present similar properties with the same layer composition, keeping a similar RMS surface roughness and band gap energy.

- The developed devices present high responsivity at low irradiance for wavelengths above the band gap, reaching 7 A/W for an irradiance of 10 W/m^2 for the device done with the $Al_xIn_{1-x}N$ N layer of 350 nm thick.
- The responsivity relationship with the optical power is strongly sublinear, achieving a γ parameter in the range of 0.79 to 0.96 depending on the layer and wavelength.
- The spectral response decreases smoothly for below-the-band gap excitation, dropping by more than an order of magnitude at 633 nm.
- The devices present persistent photoconductivity effects, with a decay time constant of 13400 s, in the range of similar devices based on nitrides. This strong persistent photoconductivity effect is related to carrier trapping in grain boundaries and dislocations.
- The general performance of these low cost devices is comparable to AlGaN photoconductors fabricated by MBE or MOVPE.

8.2. $Al_xIn_{1-x}N$ solar cells

This section describes the processing of $Al_xIn_{1-x}N$ layers grown on p-Si (111) into solar cells. First, a brief introduction of solar energy and solar cells is done, then it is described the device processing. Finally, the devices are analyzed.

8.2.1. Introduction

8.2.1.1. Solar energy

The consumption of electric energy in the world is around 13 TW. Different techniques are used to produce that electric energy. They are divided in three groups: fossil, nuclear and renewable. Due to the lack of fossils and the danger of nuclear power it is important to focus efforts in renewable energies. In particular, the solar energy that receives the earth in one hour is more than the energy used in one year, but as its incidence is quite dilute, a vast area of energy converters would be required to meet the world's energy consumption. Hence, high efficiency solar energy conversion is crucial.

8.2.1.2. p-n junctions

The interface between a p-type and a n-type semiconductor material is known as p-n junction. When both materials are placed in contact, electrons diffuse from the region with high electron concentration (n-type) to the region with low electron concentration (p-type). The diffusion of electrons across the p-n junction produces the electron-hole recombination in the p-type side. In the p-n interface zone a built-in electric field is formed. It points from the positively charged zone created in the n-zone to the negatively charged zone created in the p-zone. This built-in electric field causes the movement of some electrons and holes in the opposite direction indicated by the flow caused by diffusion (see Figure 8.11).

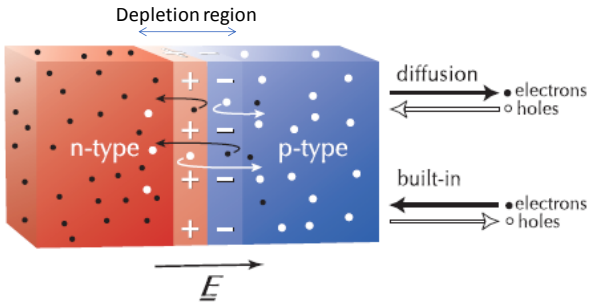

Figure 8.11. p-n junction showing the depletion region and the motion of the electrons and holes due to the built-in electric field [Spro00].

The region where electrons and holes have diffused across the junction is called the depletion region because it contains practically no mobile charge carriers.

The width of the depletion region can be changed by applying an external voltage. When a forward bias is applied, this is, when a positive external voltage is applied to the p-type side and a negative voltage to the n-type side (see Figure 8.12), diffusion current can flow because the built-in electric field and the applied electric field are in opposite directions. The holes in the p-type region and the electrons in the n-type region are pushed toward the junction and start to neutralize the depletion zone, reducing its width. The positive potential applied to the p-type material repels the holes, while the negative potential applied to the n-type material repels the electrons. The change in potential between the p-side and the n-side decreases. With increasing forward-bias voltage, the depletion zone becomes thin enough that the zone's electric field cannot counteract charge carrier motion across the p–n junction, which as a consequence reduces electrical resistance.

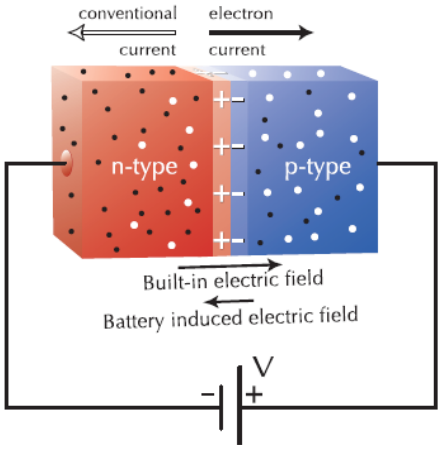

Figure 8.12. Forward bias scheme of a p-n junction [Spro00].

However, when applying a reverse bias, this is when a negative voltage is applied to the p-type side and a positive voltage to the n-type side, no current flows because the built-in electric field and the applied electric field are in the same direction. As the p-type material is now connected to the negative terminal of the power supply, the holes in the p-type material are pulled away from the junction, leaving behind charged ions and causing the width of the depletion region to increase. Likewise, as the n-type region is connected to the positive terminal, the electrons will also be pulled away from the junction, with similar effect (see Figure 8.13). This increases the voltage barrier causing a high resistance to the flow of charge carriers, thus allowing minimal electric current to cross the p–n junction. The increase in resistance of the p–n junction results in the junction behaving as an insulator.

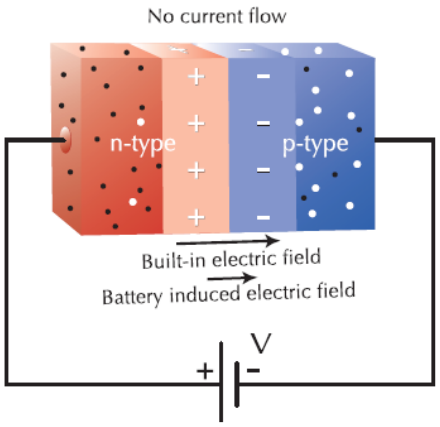

Figure 8.13. Reverse bias scheme of a p-n junction [Spro00].

These changes can be observed in the IV characteristics of the p-n junction as shown in Figure 8.14.

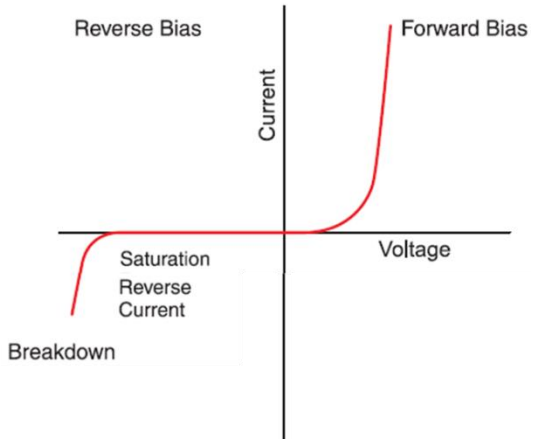

Figure 8.14. IV characteristic of a p-n junction.

8.2.1.3. Solar cells

A solar cell is configured as a large area p-n junction, it converts sunlight energy into electricity by the photovoltaic effect. Incident photons with enough energy to overcome the band gap energy of the material generate electron-hole pairs, the electron-hole pairs that do not recombine generate a current flow related to the built-in potential of the material.

The IV curve of a solar cell under dark and illumination conditions is shown in Figure 8.15. Some important values that define a solar cell under illumination are shown in the figure, the short circuit current (I_{sc}) is the current intensity generated by the device at 0 V and the open circuit voltage (V_{oc}) is the voltage drop at the device for 0 A.

The diode equation (see Eq. (8.2)) relates the current intensity with the voltage through the initial current (I_0) and the ideality factor (n), which represents the difference between the behavior of the ideal diode and that of the real diode. For an ideal diode with no recombination, n = 1.

$$I = I_0 \cdot \left[exp\left(\frac{qV}{nkT}\right) - 1 \right] \tag{8.2}$$

The fill factor (FF) is defined as the relation between the maximum power that is obtained from the solar cell ($P_{max}=I_{mp} \cdot V_{mp}$) and the product of V_{oc} and I_{sc}. The fill factor measures the degree of "rectangularity" of the characteristics.

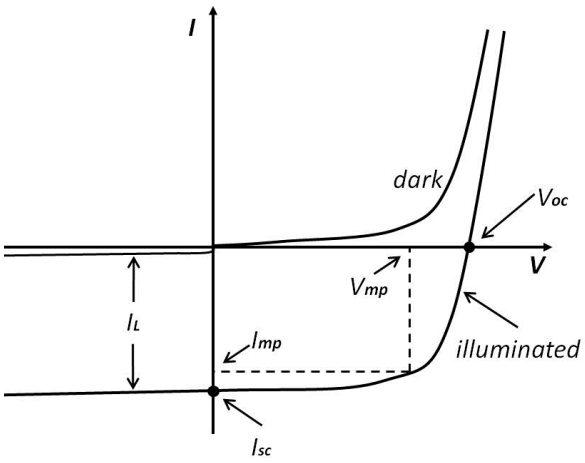

Figure 8.15. IV curve of a solar cell under dark and illumination conditions [PSPS13].

The equivalent circuit of a solar cell involves series resistance (R_s) and shunt resistance (R_{sh}) (see Figure 8.16), which represent the losses of the input optical power due to parasitic resistances. To avoid the current losses and maximize the output power, it is necessary to increase R_{sh} and decrease R_s. Normally, the origin of the R_s comes from the resistance of the contacts (resistance between the metal and semiconductor and resistance of contacts itself). The shunt resistance comes from leakage current through the cell and surface recombination.

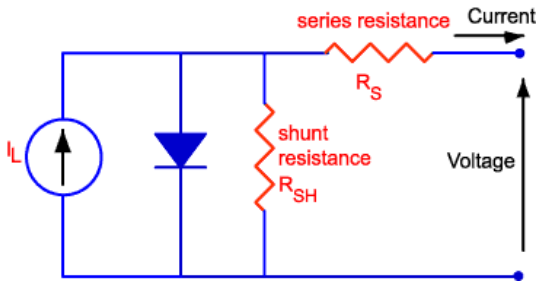

Figure 8.16. Diode equivalent circuit scheme of a solar cell [HoBo00].

The energy conversion efficiency of a solar cell is defined as the ratio of the electric power generated by the solar cell to the incident sunlight energy into the solar cell per time.

The sunlight spectrum has been standardized so that all efficiencies refer to the same incident energy. Figure 8.17 shows the standardized spectrum at AM1.5G (Air Mass 1.5 Global) which is the most common standard used for terrestrial solar cells. The solar spectrum ranges from 300 nm to 2000 nm, it presents a peak at ~500–600 nm with high contribution from the visible range. The dips observed at around 1100 nm and 1400 nm are due to absorption in the atmosphere by CO_2 and H_2O. As the main part of the solar energy is in the visible range, it is important to search for materials with band gap energies in that range so that the energy efficiency is increased.

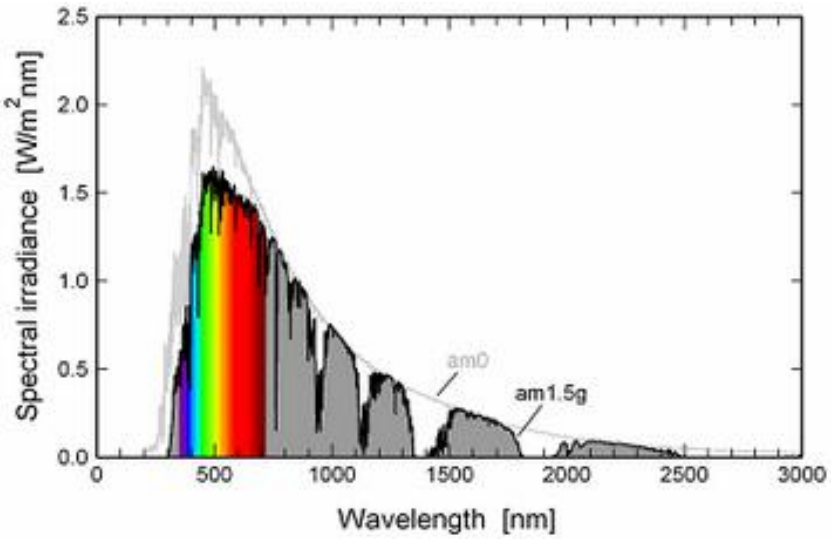

Figure 8.17. Sunlight standardized spectrum at AM1.5G [Pvli00].

III-V semiconductor solar cells have exhibited high energy conversion efficiencies [GEHW16]. Other advantages of these materials are: the capability of changing the band gap energy by changing the composition, the high photon absorption due to the direct band gap energy, the high resistivity against high-energy rays in space, and the small degradation by heat. The energy conversion efficiencies of III-V multijunction solar cells have been steadily increasing year-to-year and are approaching 45% for laboratory-scale cells (see Figure 8.18). In particular, the $Al_xIn_{1-x}N$ alloy ranges its band gap energy from 0.7 eV to 6.2 eV depending on the composition, a multi-junction solar cell with different alloy compositions will cover most part of the solar spectrum.

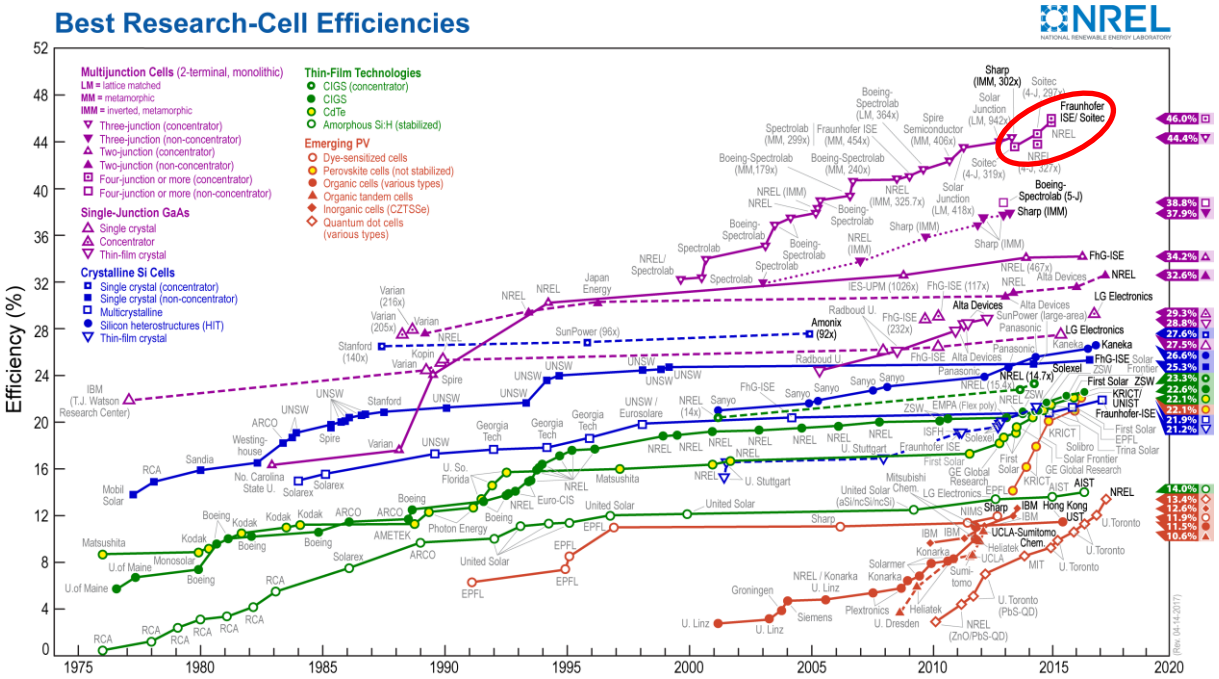

Figure 8.18. Chronological record energy-conversion efficiencies of solar cells [Nati16].

A lot of efforts have been made to improve the cell performance for the development of space activities and as a solution for the global environmental issues.

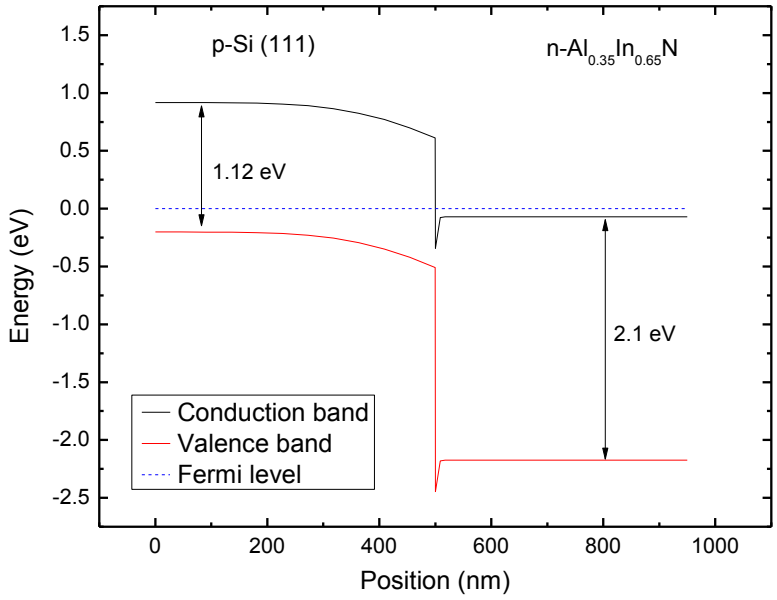

Figure 8.19. Band diagram of a n-$Al_{0.35}In_{0.65}N$ / p-Si (111) structure simulated with Nextnano[3].

In this section, $Al_xIn_{1-x}N$ is proposed as the active layer for a solar cell. Simulations of a n-$Al_{0.35}In_{0.65}N$ / p-Si (111) heterostructure performed with Nextnano^3 points to a rectifying behavior with an expected built in voltage of around 0.9 eV (see Figure 8.19). These results are in agreement with the one reported by Liu *et al.* [LDTD13]. This behavior will be tested experimentally. The developed n-$Al_{0.35}In_{0.65}N$ / p-Si (111) layers have been processed as devices and they have been characterized. The effect of including an AlN buffer layer has been studied on the device properties.

8.2.2. Growth conditions and layer characterization

A set of samples with 80 nm thick $Al_xIn_{1-x}N$ and different buffer layer thickness of AlN is used to study the solar cell response (see Figure 8.20). The $Al_xIn_{1-x}N$ layer thickness was fixed thanks to simulations with Pc1d software [BNMN16]. This thickness is good enough to present solar cell response and sufficient to study the layer properties before the solar cell performance.

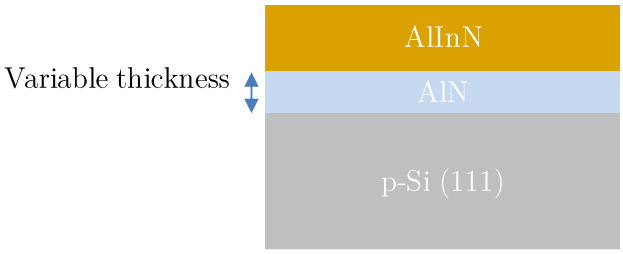

Figure 8.20. Scheme of the set of samples under study in this section to study the effect of the AlN buffer layer thickness on the properties of the solar cell device.

In Chapter 6 the AlN buffer layer and the $Al_xIn_{1-x}N$ layer grown on p-Si (111) were optimized separately. Also in that Chapter a description of the growth conditions and properties of the $Al_xIn_{1-x}N$ /AlN layers is done. As a summary, it can be pointed out some important properties of these layers: the AlN buffer layer does not affect to the $Al_xIn_{1-x}N$ composition, but the crystal quality is improved when the AlN buffer layer is in the 4 to 15 nm range. The layer morphology is not affected obtaining in all cases compact samples with an RMS surface roughness of ~1.3 nm. The band gap energy of ~2 eV and low temperature PL emission at 1.8 eV of the layers are suitable for photovoltaic applications.

8.2.3. Device fabrication

The device fabrication of the layers was performed mainly in the clean room of INAC CEA-Grenoble, except the mesa formation: the photolithography was done in the Complutense University of Madrid and the sputtering etching with Ar in the sputtering chamber described in Chapter 3.

The first step in the device processing is surface cleaning. This step must be done just before starting the device processing, so that the contamination of the surface that can occur during the storage of the sample is avoided. It is carried out submerging the sample in acetone in an ultrasonic bath so that the organic contaminants are removed. Then the sample is introduced in methanol and finally it is blown with nitrogen.

Then the size of the device is determined by a mesa structure (see Figure 8.21). A photolithography process is done to transfer the pattern of a mask to the sample and then a physical etching, in the sputtering chamber described in Chapter 3, by applying a 40 W RF power to the substrate in an Ar ambient (Ar flow: 2 sccm) under a 5 mTorr pressure, is used for removing the $Al_xIn_{1-x}N$ layer of a part of the sample that is not covered with the photoresist and reach the substrate. It is a low selectivity process and produces high surface roughness.

Once the sputtering etching is finished the photoresist has to be removed. For this purpose, we use hot acetone, then it is submerged in dimethyl sulfoxide solvent in an ultrasonic bath and in methanol, and finally it is blown with nitrogen.

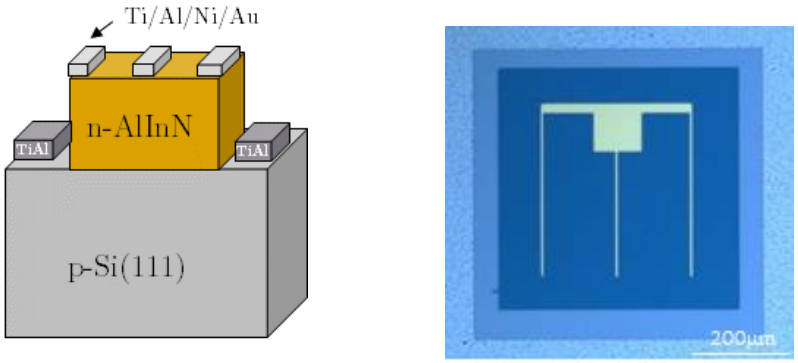

Figure 8.21. Left: Scheme of the processed device as solar cell with mesa structure. Right: Top view of the 1×1 mm² processed devices.

The next step is the metallization of the sample for doing the electrical contact of the device. Previously, photolithography is used for transferring the pattern that is going to be used for the contacts. The metallization is done by evaporation, in this technique the metals are heated and evaporated so that a thin film of metal is formed in the surface of the sample. The metals must be chosen in order to obtain ohmic contacts, so that the carriers can easily move between the contacts and the semiconductor.

The contacts grown on the substrate are a 50 nm Ti/ 100 nm Al contact. To improve the ohmicity of the contact, it is necessary to make an annealing process at 550°C under nitrogen atmosphere during 5 minutes.

However, the contacts grown on the top of the $Al_xIn_{1-x}N$ layers are formed by consecutive layers of 30 nm Ti, 70 nm Al, 20 nm Ni, 100 nm Au. They are made in a finger pattern structure with a width of 5 µm and a distance between fingers of 150 µm.

A schematic drawing of the device is shown in Figure 8.21 left. The n- and p-contacts can be seen at the top and bottom of the mesa structure, respectively. While Figure 8.21 right shows a top view of the 1×1 mm^2 processed device.

The last step in the device processing is the lift-off. This process removes the photoresist and thus leaves the contrary pattern of metal. For the removal of the photoresist, the samples are submerged in acetone and they are shaken manually to accelerate the removal of the photoresist. If this is not sufficient they are introduced in an ultrasonic bath. Then they are rinsed in methanol and dried with nitrogen.

8.2.4. Experimental setups

8.2.4.1. IV characteristics

The current-voltage measurements were carried out under dark and illumination conditions. The measurements done under dark conditions are recorded with an Agilent 4155C parameter analyzer, while the measurements done under illumination are done in a solar simulator. The solar simulator used is a Spectra-Nova's CT Series Solar Cell Tester (Class AAA) which is used to perform current-voltage measurements under simulated AM1.5G spectrum (100 mW/cm^2).

All IV measurements are performed at 25°C (the substrate holder temperature is controlled) in a four-point probe configuration. The solar simulator is located at the CEA-Grenoble and these measurements were carried out by Dr. Sirona Valdueza-Felip under the supervision of Dr. Louis Grenet.

8.2.4.2. Responsivity

The responsivity of the devices as a function of the incident light is measured with the setup shown in Figure 8.22.

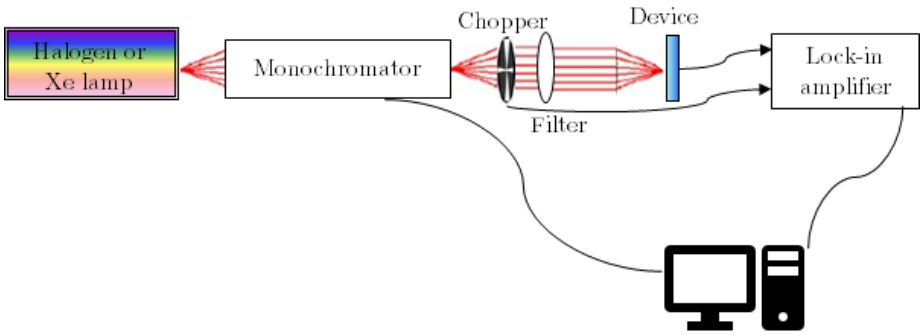

Figure 8.22. Scheme of the responsivity setup used for characterizing the solar cell devices.

A 250 W halogen lamp coupled with a Oriel Instruments Cornerstone 130 1/8m monochromator is used for measuring the spectral response of the devices in the 380-1200 nm range. The voltage of the sample as a function of the incident light is measured with a lock-in amplifier. These results give a relative idea of the shape of the photoresponsivity.

To obtain quantitative data it is necessary to measure the responsivity of the sample at a certain incident light. For this purpose, a GaN laser diode emitting at 405 nm is used as incident light. The relationship between the incident intensity (P_{opt}) and the output current (I_{405nm}) of the sample gives an idea of the responsivity (R) of the sample for that wavelength ($R = I_{405nm}/P_{opt}$). Once the responsivity is known at the value of 405 nm, it is possible to normalize the rest of the curve to that point.

The external quantum efficiency (EQE) can be estimated from the responsivity values taking into account Eq. (8.3) that relates EQE with the responsivity (R),

the wavelength (λ), the speed of light (c), the electron charge (q) and Planck's constant (h).

$$\mathrm{EQE} = \mathrm{R}\frac{hc}{q\lambda} \tag{8.3}$$

8.2.5. Experimental results

Figure 8.23 shows the IV characteristics of the devices under dark conditions. All the samples under dark conditions present a good rectifying behavior. The threshold voltage (V_{Th}) increases when increasing the buffer layer thickness (see Table 8.1) except for the one with 4 nm buffer layer that presents the minimum one (~0.65 V). The short circuit current (I_{sc}) is the intensity of the device at 0 V. All the samples show a I_{sc} of 0 mA under dark conditions. This is important since it means that, when no voltage is applied and there is no incident radiation, there is also no current in the cell.

It is also possible to estimate the series resistance (R_s) and the shunt resistance (R_{sh}) from the IV curve measured under dark conditions. These resistances simulate the internal resistances that reduce the solar cell efficiency by power dissipation. The R_s is the inverse of the slope at high voltage values while R_{sh} is the inverse of the slope at I_{sc}.

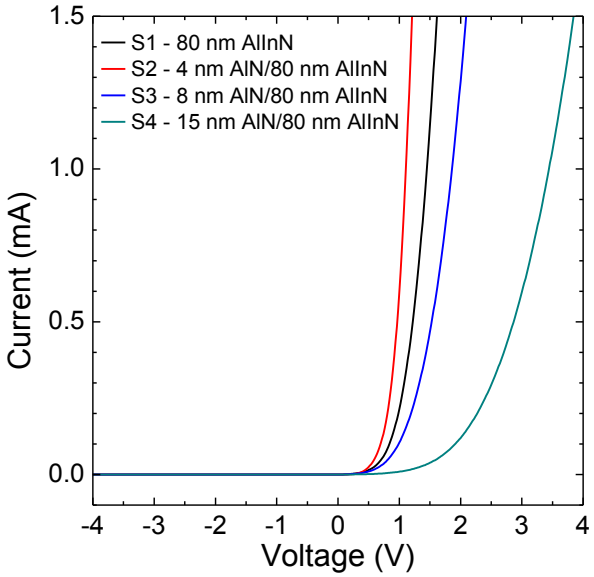

Figure 8.23. IV characteristics of the samples grown with different buffer layer thickness under dark conditions.

A further investigation of the IV characteristics under dark condition allows the estimation of the initial current (I_0) and the ideality factor (n) which indicates how closely the diode follows the ideal diode equation. Eq. (8.4) is a modification of Eq. (8.2) for taking into account the shunt and series resistance:

$$I = I_0 \cdot \left[exp\left(\frac{V_d}{n \cdot V_T}\right) - 1 \right] + \frac{V_d}{R_{sh}} \tag{8.4}$$

where, V_d is the voltage diode which is estimated as $V_d = V - I \cdot R_s$, V_T is the thermal voltage and it is given by $V_T = \frac{k_B \cdot T}{e}$ and at RT it is 26 mV. To estimate these parameters the V_d has to be calculated and it has to be represented and fitted exponentially $I = I_0 e^{bV_d}$ for values not affected by R_s or R_{sh}, then the ideality factor is estimated as $n = \frac{1}{b \cdot k_B \cdot T}$.

Table 8.1. Summary of the threshold voltage (V_{Th}), series resistance (R_s), shunt resistance (R_{sh}), initial current (I_0) and ideality factor (n) extracted from the IV characteristics performed under dark conditions.

	V_{Th} (V)	R_s (Ω)	R_{sh} (MΩ)	I_0 (A)	n
S1	0.78	120	1	7e-7	7
S2	0.65	92	2	1e-7	4
S3	0.94	154	1	1e-6	10
S4	1.71	417	3	2e-6	19

The values extracted from these fittings are shown in Table 8.1, and they give the initial values for fitting the experimental values with Eq. (8.4). For a better fit of the experimental data, these values have to be modified and the values that best fit are shown in Table 8.2.

Table 8.2. Summary of the series resistance (R_s), shunt resistance (R_{sh}), initial current (I_0) and the ideality factor (n) used for the best fit to Eq. (8.4) of the IV characteristics performed under dark conditions.

	R_s (Ω)	R_{sh} (MΩ)	I_0 (A)	n
S1	100	100	2e-7	6.8
S2	88	20	4e-8	3.5
S3	130	20	1e-7	7
S4	360	25	8e-8	12

The device that presents the smallest internal resistance is the one done with 4 nm buffer layer thickness as shown in Table 8.2. This is also the one that presents the minimum ideality factor although this value is still high due to recombination at the interface of the heterojunction.

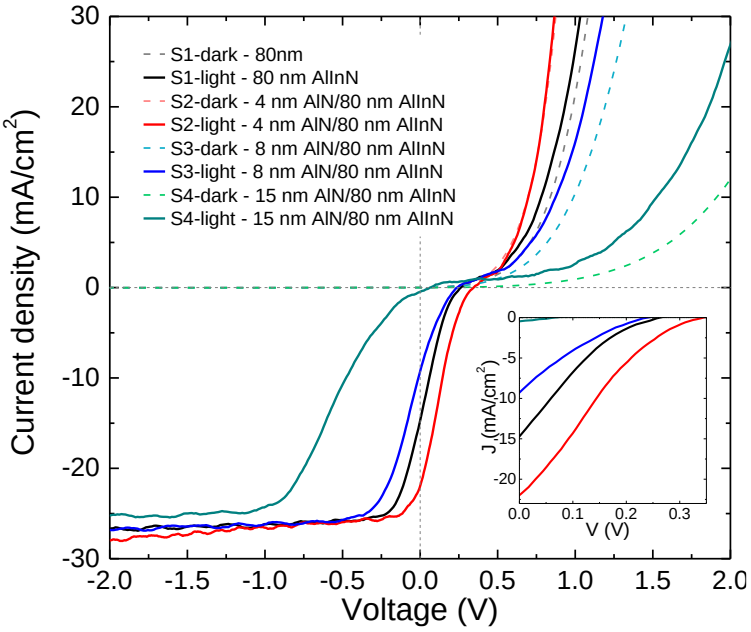

Figure 8.24. IV characteristics of the samples grown with different buffer layer thickness under dark and illumination.

When the light reaches the device (see Figure 8.24), the behavior of the IV characteristic is modified. This means that the device is affected by light. As mentioned previously, the illumination is done with a solar simulator.

Table 8.3. Summary of the short circuit current density (J_{sc}) and open circuit voltage (V_{oc}) for the samples with different AlN buffer layer thickness under illumination.

	J_{sc} (mA/cm²)	V_{oc} (V)	FF (%)
S1	14.9	0.26	17
S2	21.8	0.34	20
S3	9.2	0.24	17
S4	0.5	0.07	17

The short circuit current density (J_{sc}) and the open circuit voltage (V_{oc}, that is the voltage when the I=0 A) of the devices under illumination are estimated. The best

device will be the one that presents higher values of these two parameters. In this case the best device is the one performed with the $Al_xIn_{1-x}N$ layer grown with a 4 nm-thick AlN buffer layer (see Table 8.3). The fill factor (FF) has been calculated as the relationship between the maximum power and the product of $V_{oc} \cdot J_{sc}$, this value is in all cases <20% pointing out to a poor rectangular shape of the JV curve. Also, it confirms that the best device is the one with 4 nm of AlN buffer layer because it is the one with higher FF.

The plateau that is shown in the JV curves under illumination conditions is related to a non-linear photocurrent behavior. This effect has been previously observed in InGaN/GaN devices [JFHK07, NCFI11]. This non-linear photocurrent can be explained by two mechanisms. The first one is related with the formation of a Schottky barrier between the p-Si and the metal contact. This barrier opposes to the light-generated current [JFHK07]. The other explanation is related to suppressed carrier collection due to polarization charges localized at the interface of the p-n junction that avoid the movement of the carriers from one side to another [NCFI11]. We have studied with Pc1d simulations the IV characteristics of our devices. We have seen that for a good fitting of the IV curves, it is necessary to increase the surface recombination in the silicon and the silicon contacts should present a high resistivity. In summary, these effects should be related with the poor ohmicity of the contacts grown on p-Si (111). But it has to be taken into account that it can also be related with polarization charges, as it has been observed by Liu *et al.* in $Al_xIn_{1-x}N$ layers grown by RF sputtering [LDTD13].

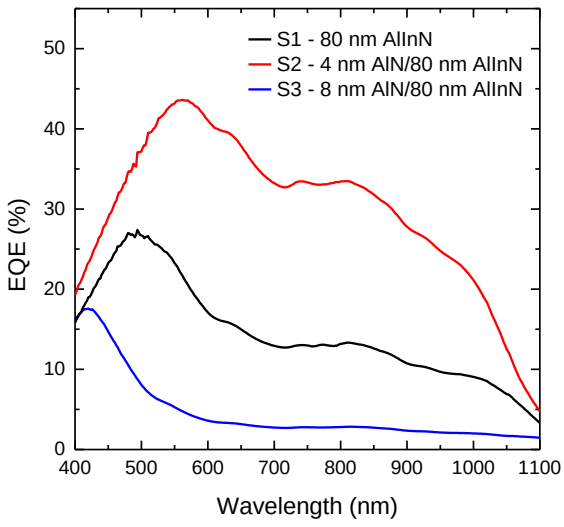

Figure 8.25. External quantum efficiency of the samples with different buffer layer thickness.

Finally, the external quantum efficiency of the samples under study is shown in Figure 8.25. In all samples there is a maximum of the EQE at low wavelengths (400-560 nm) which is related to the response of the $Al_xIn_{1-x}N$ layer. At ~900 nm, the cut off of the silicon is shown.

The sample without buffer layer present an acceptable value of EQE, but it is improved with the introduction of a 4 nm-thick AlN buffer layer, which is the device that presents a higher EQE. This was expected because it is the one that presents better results in the IV characteristics. The increase of the buffer layer thickness to 8 nm leads to lower EQE because this sample has a maximum of reflectance @490 nm, which means that ~40% of the incident light reaching the sample is reflected, so less quantity of light reaches the device (see Figure 8.26). Also an increase of the electric field at the heterointerface occurs, which means that the collected carriers are reduced because the transport through the AlN layer is inefficient.

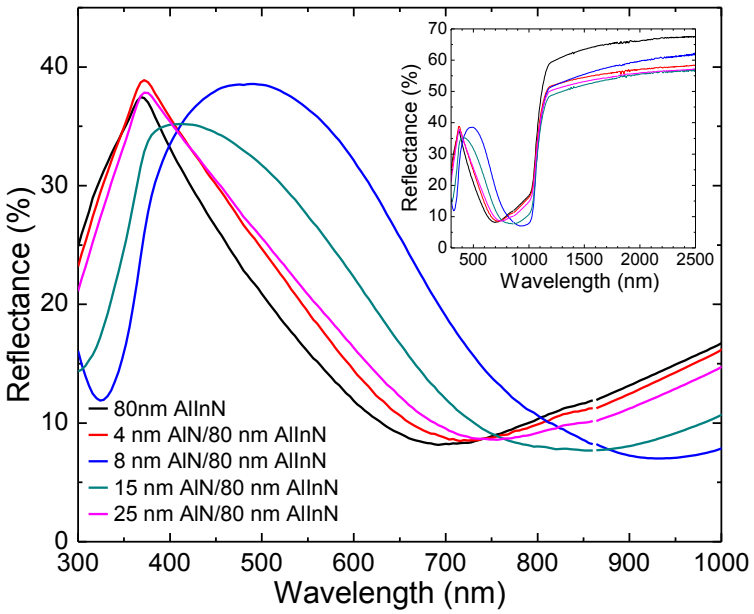

Figure 8.26. Zoom of the visible part of the reflectance measurements of the samples grown on p-Si (111), inset whole reflectance measurements.

8.2.6. Conclusions

In this section, it has been demonstrated the possibility of obtaining solar cells with $Al_xIn_{1-x}N$ layers grown on p-Si (111) by RF sputtering.

- It has been proved that the use of a thin AlN buffer layer improves the operation of the device due to the improvement of the $Al_xIn_{1-x}N$ material which was studied in Chapter 6.
- The values extracted from the IV characteristics under dark and illumination conditions show that the best device is the one formed by 4 nm AlN and 80 nm $Al_xIn_{1-x}N$ on p-Si (111). It is the one with lower internal resistance and ideality factor, and higher short circuit current and open circuit voltage.
- The device performed with the layer of 4 nm AlN and 80 nm $Al_xIn_{1-x}N$ is the one that presents higher EQE. For increasing the EQE, the layer thickness has still to be optimized.
- This was a first step for demonstrating that $Al_xIn_{1-x}N$ is a promising material for its application in solar cells. It is also required the improvement of the contacts in order to minimize the non-linear photocurrent shown in the IV characteristics under illumination.

8.3. $Al_xIn_{1-x}N$ surface plasmon resonance sensor

This section describes the use of $Al_xIn_{1-x}N$ layers as dielectric layer in surface plasmon resonance sensors. For it a tapered optical fiber is used as substrate and aluminum is used as the metal layer. First, a brief introduction of plasmons, surface plasmon resonance and surface plasmon resonance sensors is done. Then the device fabrication and the experimental measurements are described. Finally, the devices are analyzed.

8.3.1. Introduction

8.3.1.1. Plasmon

A plasmon is a quantum of plasma oscillation, that can be considered as a quasiparticle since it arises from the quantization of plasma oscillations. Plasmons are collective oscillations of the free electron gas density [PiBo52]. Since plasmons are the quantization of classical plasma oscillations, most of their properties can be derived directly from Maxwell's equations.

8.3.1.2. Surface plasmon resonance

Surface plasmons are coherent delocalized electron oscillations that exist at the interface between two materials with opposite real part dielectric constants, for instance, a metal and a dielectric [HoYG99]. The degree of light confinement and propagation distance is highly affected by the chosen materials due to losses. When the frequency of the incident photons is equal to the natural frequency of the electrons oscillating in the surface the resonance condition is established.

8.3.1.3. Surface plasmon resonance sensor

One of the most sensitive label-free and real time detection technique is the surface plasmon resonance. This technique is widely used in biosensing [AbLC11]. A large number of SPR-based devices have been developed for chemical, biomedical and environmental monitoring [Homo08]. SPR sensors present high sensitivity to small changes in the refractive index of the medium close to the sensor's surface. Therefore a functionalization of the sensor's surface can lead to specificity in the readout signal when a particular molecule is attached to a ligand fixed on such surface [SHTW15]. Several setups have been proposed to excite this kind of sensors, but among all of them the attenuated total internal reflection is the most reported one in literature [KrRa68]. The experimental arrangement can be simplified by using optical fibers. All-fiber systems intrinsically provide substantial advantages such as remote measurements, operation in harsh environments, easier handling, small size and weight [GNED14, PHMČ03, ShJG07]. Since the spectral interrogation of SPR-based sensors is the most robust technique, the tuning of the

sensor resonance has been an issue in order to use portable and low cost spectrometers based on silicon or InGaAs detectors.

Spectral tuning of SPR sensors is traditionally achieved by growing a dielectric overlay on top of a metallic layer. The dielectric is usually a metal-oxide [GBED05, UsMG15], but it is possible to use other dielectrics to achieve the desired operation point. Following this procedure, a specific resonance wavelength can be obtained for a fixed refractive index of the outer medium.

Previous studies demonstrated the possibility of using InN as the dielectric layer of the SPR sensor [ENDV11]. Now we propose the use of a ternary compound ($Al_xIn_{1-x}N$) for expanding the refractive index range of the sensor by tuning the Al composition [PPQO97]. The unique properties of III-nitrides such as its high thermal and chemical stability while being environmentally friendly, make them suitable for *in situ* environmental measurements. Besides, III-nitrides offer the possibility of surface functionalization which makes feasible their use in chemical and biological sensors where a high sensitivity to a specific molecule is needed [ChSo08].

As it has been demonstrated in Chapter 7, it is possible to grow crystalline $Al_xIn_{1-x}N$ layers at RT. This section describes the development of SPR sensors based on Al/ $Al_xIn_{1-x}N$ bilayer. The spectral response and sensitivity of the devices have been studied as a function of deposition conditions and bilayer dimensions. In particular, the effect of fiber rotation during the $Al_xIn_{1-x}N$ growth, its aluminum content and the Al metal layer thickness have been addressed.

8.3.2. Device fabrication

Two steps are involved in the fabrication procedure, the tapering of the optical fiber and the growth of the bilayer. The first one is the tapering of a standard optical fiber to achieve a single-mode uniform-waist tapered fiber (UWTFs). This is obtained by using the travelling burner technique [KeBO91]. In this technique, a flame heats in an oscillatory way the optical fiber around the length to be stretched; meanwhile the fiber is pulled in opposite directions with two step-by-step motors (see Figure 8.27). With this procedure, it is possible to have a precise control of the taper parameters, namely waist diameter, taper length and transition profile between the original fiber and the uniform waist section. The developed

UWTFs have 30 µm waist diameter, 18 mm waist length and a total taper length of around 50 mm. These values have been chosen considering the trade-off between evanescent field strength and mechanical robustness.

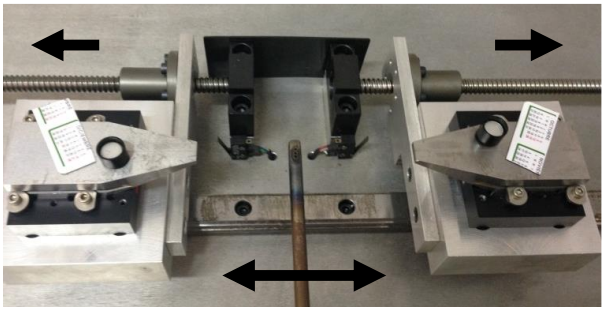

Figure 8.27. Experimental setup used to obtain UWTFs located in the GRIFO facilities at the University of Alcalá.

The second step is the deposition of a metal layer followed by the deposition of the dielectric one on the surface of the tapered optical fiber. In our case, the deposited layers are Al and $Al_xIn_{1-x}N$ respectively. This is done in the reactive sputtering system described in Chapter 3. The Al layer is deposited by sputtering a pure Al (99.999%) target in an Ar (99.999%) ambient and using a DC power of 75 W, without rotation of the substrate holder. The $Al_xIn_{1-x}N$ layers were deposited as described in Chapter 7, co-sputtering pure In and Al targets in a pure nitrogen ambient. The RF power applied to the indium target was set at 40 W, while the RF power applied to the Al target was set to 150 W for the AlN and the $Al_xIn_{1-x}N$ layers.

Using these deposition parameters, SPR sensors with Al layers of either 8 or 20 nm-thick and with (Al,In)N thickness of 60 nm were developed. Since the device holder inside the sputtering system keeps the fiber always in the parallel plane to the substrate holder without rotating the fiber around its longitudinal axis, the obtained devices are asymmetric, with only approximately half of the taper covered by the bilayer structure and expected non-uniform layers thickness, as seen in the zoomed view plotted in Figure 8.28.

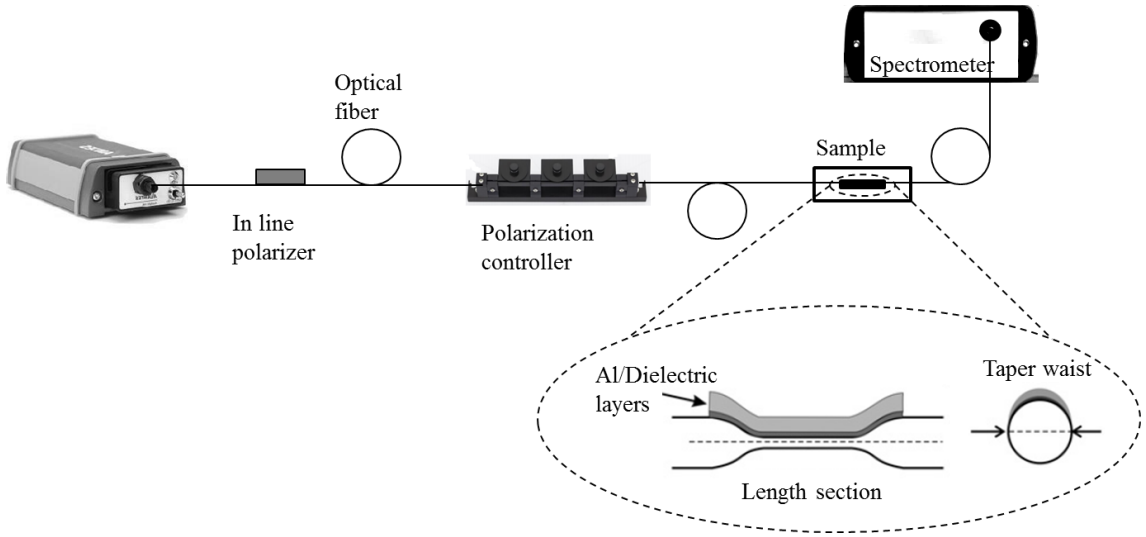

Figure 8.28. Experimental setup scheme for the SPR sensor transmittance characterization and detailed view of the fabricated transducer.

8.3.3. Experimental setup

The developed SPR sensors are characterized by measuring the spectral transmittance of the device for different refractive indices of the outer medium [ViMM03]. Figure 8.28 shows the setup used for the transmittance measurements. A halogen lamp is used as light source to take advantage of its wide emission spectrum. A CCD spectrometer Avantes AvaSpect NIR 256-1.7 is used for measuring the transducer transmittance as a function of the wavelength. Since the SPR phenomenon in asymmetric tapers is still polarization-dependent, a polarization-control system based on a linear polarizer and a set of Lefèvre loops has been included in the characterization setup [GBED05]. This system should give a sharp transmittance dip when the polarization plane of the light probe is aligned with the maximum thickness of the deposited layers.

Firstly, it is needed to measure the spectral transmittance of the device with air as surrounding medium. This is used as reference for the whole experiment. Then the outer refractive index is ranged from 1.3215 to 1.4216 (values at 1300 nm) using a mixture of pure water and ethylene glycol, respectively. The index of the different solutions is calculated considering the refractive index of the pure elements and the volume used of each one [SPPV07]. The specific refractive index value for a given wavelength is determined by the dispersion relationships of the individual components [Poly00].

8.3.4. Experimental results

8.3.4.1. Effect of rotation during the growth of ternary compounds

First, it has been studied the effect that the rotation of the fiber has during the growth of $Al_xIn_{1-x}N$ in the properties of the SPR sensor. This study will give an insight of the effect of sputtering chamber asymmetry on the sensor properties. The sputtering chamber has three confocal magnetron guns placed on the top system flange forming a triangle and only two of them are used simultaneously for the deposition of the $Al_xIn_{1-x}N$ ternary, thus, the sputtered Al and In species reach the deposition surface with a small angle while the whole deposition process suffers from the asymmetry.

Two SPR sensors of 20 nm of Al and 60 nm of $Al_xIn_{1-x}N$ were deposited. One of the SPR sensors was deposited while rotating the substrate at 20 rpm within the substrate holder plane during the growth of the ternary compound. The other one was grown keeping a fixed position of the tapered optical fiber placed perpendicular to the plane of symmetry between both used guns for the ternary deposition (Al and In).

The expected values of SPR resonance wavelength can be predicted by using simulation routines. In these routines the spectral transmittance is studied as a function of the different involved parameters, namely uniform waist diameter and length together with thicknesses and refractive indices of the deposited layers [ViMM03]. Therefore, a first approach of the expected transmittance for an Al/ $Al_xIn_{1-x}N$ bilayer device 20/60 nm-thick respectively was carried out, knowing the refractive indices of silica and aluminum [Poly00] and estimating the refractive index of the $Al_xIn_{1-x}N$ (2.2 @1300 nm) layer as an interpolation from the values of the InN [MNJP15] and AlN [Poly00], being them 2.3 and 2.15 @1300 nm, respectively. Since a strong dispersion is no expected in the investigated wavelength range, a constant value of around 2.2 has been used in the calculation procedure. The obtained result is shown in Figure 8.29a, where the transmittance for several outer refractive indices are plotted.

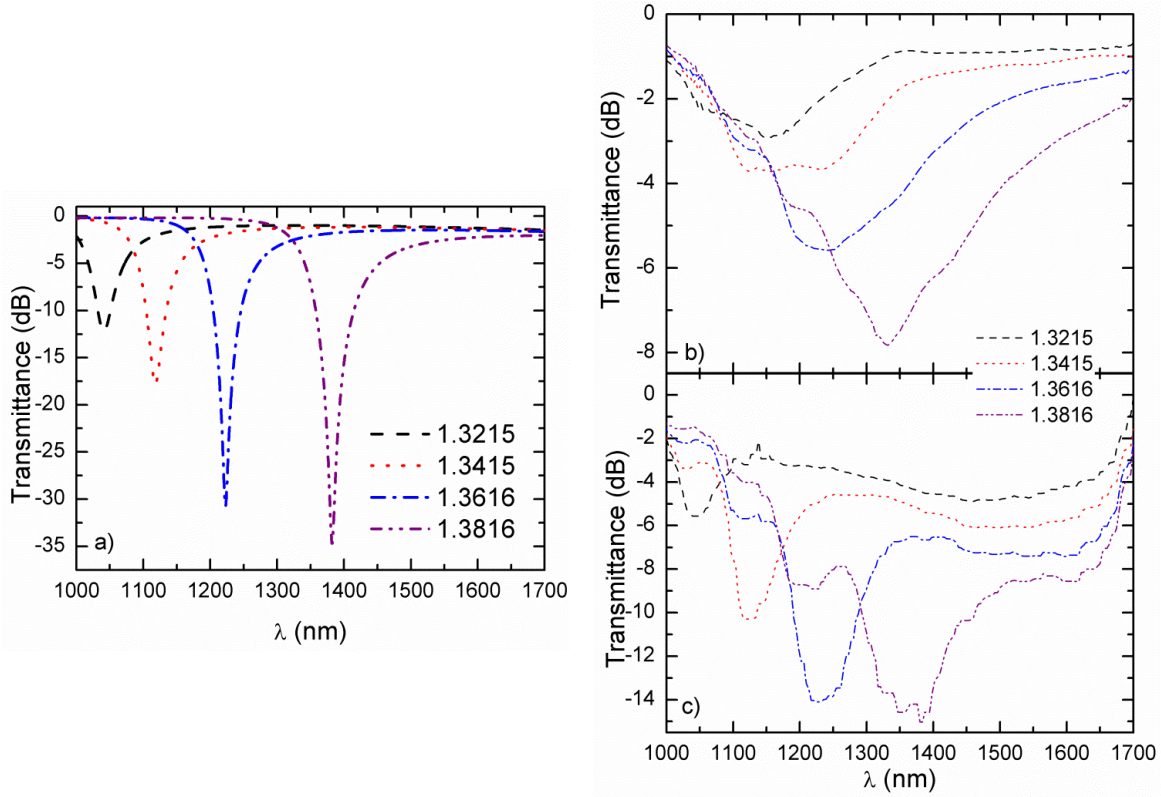

Figure 8.29. Transmittance of a device with a 20 nm Al/ 60 nm $Al_{0.36}In_{0.64}N$ bilayer for outer refractive indices ranging from 1.3215 to 1.3816 calculated for a central wavelength of 1300 nm. a) Simulation of the SPR devices assuming uniform dielectric layer in terms of layer thickness and alloy homogeneity. b) Dielectric layer grown without rotation. c) Dielectric layer grown with rotation.

Figure 8.29b and c show the measured transmittance spectra for both SPR sensors for different refractive indices of the outer medium. In these figures, the shortest resonance wavelength corresponds to pure water as outer medium, with a refractive index of 1.3215, while the largest one comes from an outer refractive index of 1.3816 which corresponds to a mixture of 60% volume ethylene-glycol in deionized water. The refractive index values have been calculated for the central wavelength of the investigated range, which is around 1300 nm. When increasing the outer refractive index, the transmittance dip shifts towards higher wavelengths. This occurs in both cases, as expected in UWTF-based SPR sensors. An increase by a factor of 2 in the coupling strength (measured as the dip contrast) is observed when the ternary dielectric layer is deposited rotating the UWTF (see Figure 8.29b, c). This is explained by the fact that the deposited layers with rotation have a much better homogeneity.

The resonant wavelength of the devices is, in both cases, in agreement with the theoretical estimations, however there are some differences in the transmittance profile due to alloy inhomogeneities, long-scale layer thickness fluctuations and surface and interface roughness.

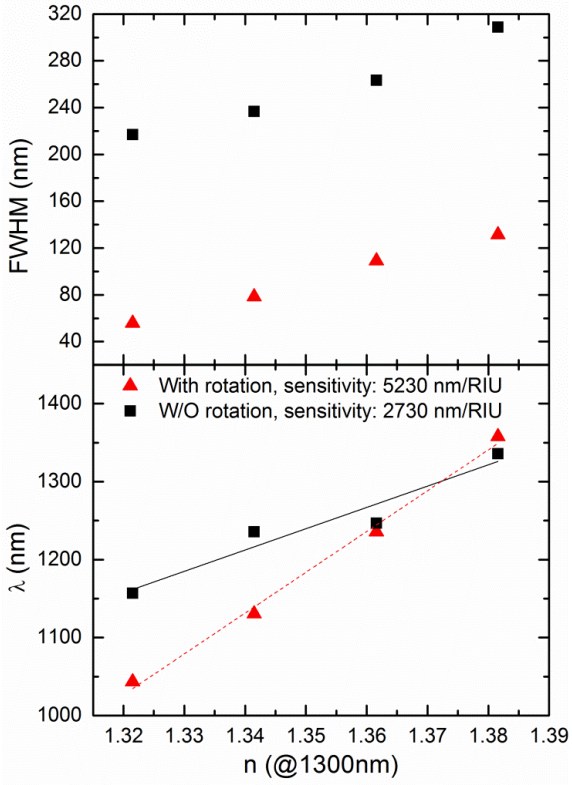

Figure 8.30. Top: Comparison of the FWHM of the transmittance dips of the 20 nm Al/ 60 nm $Al_{0.36}In_{0.64}N$ bilayer grown with and without rotation. Bottom: Change in the resonant wavelength with the outer refractive index for the devices of Figure 8.29 (20 nm Al/ 60 nm $Al_{0.36}In_{0.64}N$ bilayer grown with and without rotation), the slope of the curve gives the average sensitivity of the devices.

Figure 8.30 top shows the FWHM of the transmittance dips for both samples. As it is visible, a reduction of the FWHM is presented for the device deposited rotating the UWTF. Figure 8.30 bottom depicts the change of the main resonance wavelength with the refractive index of the outer medium. The change in resonance wavelength as a function of the outer refractive index follows a linear behavior for both devices. The device sensitivity, known as the relationship between the $\Delta\lambda$ and the Δn (the slope of linear fit to the experimental data depicted in Figure 8.30 bottom), is enhanced when rotating the substrate. A two-fold increase of the sensitivity is obtained for the sensor deposited with rotation with respect to the

device deposited in a fixed position, from 5230 nm/RIU to 2730 nm/RIU, respectively.

The enhanced homogeneity of the $Al_xIn_{1-x}N$ ternary induced by the rotation of the UWTF during the device deposition is directly related with an improvement of the sensor performance, as demonstrated by the increase of the coupling strength and the sensitivity, together with the decrease of the FWHM of the resonance dip.

8.3.4.2. Effect of the use of $Al_xIn_{1-x}N$ as dielectric layer

Three devices were further developed so that it is possible to study the effect of the dielectric composition. The devices were formed by a 20 nm-thick Al metal layer and 60 nm-thick InN, $Al_{0.36}In_{0.64}N$ and AlN as dielectric layer.

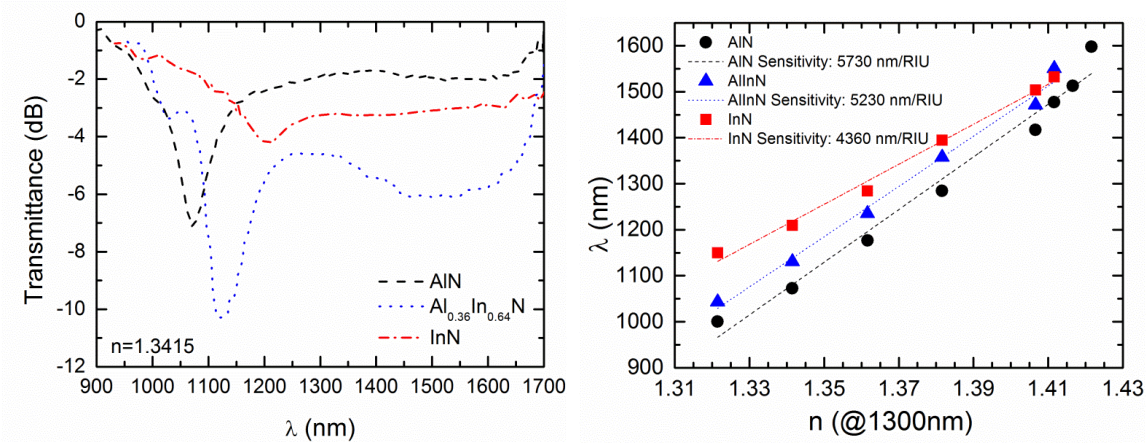

Figure 8.31. Left: Comparison of the transmittance of three devices with 20 nm Al/ 60 nm $Al_xIn_{1-x}N$ bilayer with x=0, 0.36, 1, for an outer refractive index of 1.3415. Right: Change in the resonant wavelength with the outer refractive index for the devices of Fig. 4 (20 nm Al/ 60 nm $Al_xIn_{1-x}N$ bilayer for x=0, 0.36, 1).

Figure 8.31 left depicts a comparison of the experimental transmittance spectrum of the three devices for an outer refractive index of 1.3415. A blue-shift of the resonance wavelength is observed when increasing the aluminum composition of the dielectric layer. This blue-shift is attributed to a decrease of the refractive index of the dielectric layer as shown above.

On the other hand, an enhanced coupling intensity is obtained for the sensor with 60 nm of $Al_{0.36}In_{0.64}N$ dielectric layer. This could be attributed to a decrease of the

dielectric structural quality due to the low growth temperature used for the device (see Chapter 7).

Figure 8.31 right shows the linear fit to the experimental data used to obtain the sensitivity of the devices, which shows an increase of 1.3 when increasing the aluminum content from 4360 nm/RIU to 5230 nm/RIU and 5730 nm/RIU for InN, $Al_{0.36}In_{64}N$ and AlN dielectric layers, respectively.

8.3.4.3. Effect of the metal layer thickness

The effect of the metal layer thickness is studied comparing devices with 8 and 20 nm-thick Al and 60 nm $Al_{0.36}In_{0.64}N$ on top. It is well known that if the metal layer thickness is below a certain threshold value, the sensitivity of the device is improved [Homo97].

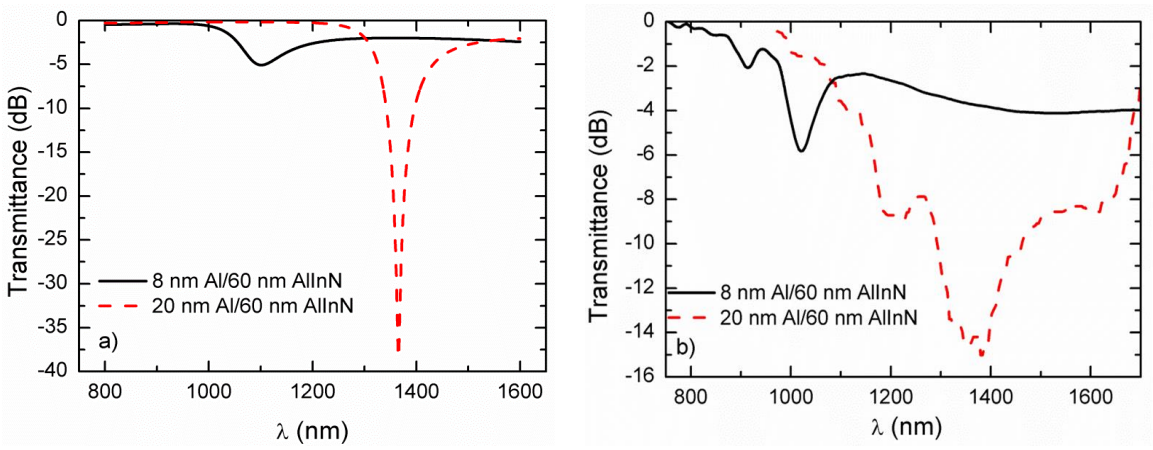

Figure 8.32. a) Simulation of the effect of the metal layer thickness. b) Comparison of the transmittance of devices with 8 nm Al and 20 nm Al/ 60 nm $Al_{0.36}In_{0.64}N$ bilayer for the same outer medium.

The theoretical transmittance of devices with different metal thicknesses are shown in Figure 8.32a. It can be seen that a red shift in the resonance wavelength occurs when increasing the thickness. The experimental measurements are compared in Figure 8.32b, where the transmittance spectra for an outer medium of 60% volume ethylene glycol are shown. The red shift observed when increasing the metal layer thickness is due to the change in the SPR wavevector with the layer thickness [Raet88].

The FWHM of the transmittance dips increases when increasing the metal layer thickness (see Figure 8.33) and the coupling strength increases a factor of 2.5 when increasing the metal layer thickness. Besides, the sensitivity increases from 2960 nm/RIU to 5230 nm/RIU for the device with 8 and 20 nm-thick of Al, respectively. Depending on the use of the sensor, for interferometric sensing or spectral interrogation, the metal layer thickness has to be chosen considering a trade-off between the sensitivity, the resonant wavelength and SPR spectral width.

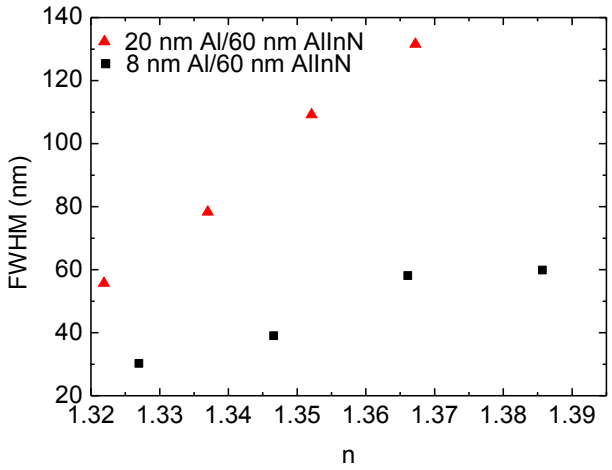

Figure 8.33. FWHM of the transmittance dips of the 8 and 20 nm Al/ 60 nm $Al_{0.36}In_{0.64}N$ bilayer.

8.3.5. Conclusions

In conclusion, it has been demonstrated the feasibility of using $Al_xIn_{1-x}N$ layers for SPR sensing.

- Simulation routines can be used to predict the values of the SPR resonance wavelength.
- It is necessary to rotate the substrate holder when growing the ternary compound to improve the homogeneity. The homogeneity of the ternary compound is a crucial parameter to obtain narrower transmittance resonance dips (with a ×4 reduction) and higher sensitivities (with a ×2 increase).
- However, for the growth of the Al layer and binary dielectrics is better to put the sample perpendicular to the target.

- The transmittance resonance dip can be selected within a range of wavelengths without sensitivity amelioration by changing the dielectric composition. The increase of Al content in the dielectric layer induces a blue shift of the resonant wavelength due to the reduction of the refractive index of the dielectric.

- In the case of the metal layer thickness it is shown that the increase of the Al thickness (from 8 to 20 nm) leads to an increase of both, the sensitivity by a factor of $\times 2$ and resonance wavelength although there is an increase in its FWHM. The metal layer thickness has to be chosen considering a trade-off between the sensitivity, the resonant wavelength and SPR spectral width depending on the use of the sensor.

- The SPR sensor with 20 nm-thick Al / 60 nm-thick $Al_{0.36}In_{0.64}N$ dielectric layer has the highest coupling strength for the range under study; which makes this sensor useful for high sensitivity measurements for a specific operation wavelength.

Chapter 9

Conclusions and perspectives

The growth of $Al_xIn_{1-x}N$ layers by RF sputtering on sapphire, p-silicon (111), glass and optical fiber substrates has been reported in this Thesis. Also the structural, chemical, morphological, electrical and optical characterization of the layers have been analyzed. Finally, the applications of the grown layers have been described.

It has been demonstrated that it is possible to grow high quality (with FWHM of the (0002) $Al_xIn_{1-x}N$ rocking curve below 5^o) $Al_xIn_{1-x}N$ layers on sapphire, p-Si (111) and glass substrates by RF sputtering by the co-sputtering of pure In and pure Al targets in nitrogen atmosphere at a wide range of growth temperatures (from RT to 550°C). In all cases the power applied to the indium target was fixed to 40 W and the chamber pressure was set at 0.47 Pa.

The conclusions and perspectives of each part of the Thesis are shown in this Chapter.

9.1. $Al_xIn_{1-x}N$ grown on sapphire by RF sputtering

Conclusions

First the layer properties were studied as a function of the growth conditions analyzing the effect of the power applied to the aluminum target and the substrate

temperature. For it two set of samples were grown, the first one keeping constant the growth temperature to 300°C and ranging the power applied power to the aluminum target from 0 to 150 W. With this set of samples it has been demonstrated that the alloy composition can be controlled by the power applied to the aluminum target, and thus the band gap energy is varied. The second set of samples was grown ranging the substrate temperature from 300 to 550°C while keeping the power applied to the aluminum target fixed to 150 W, this set of samples proved that the layer morphology is highly influenced by the growth temperature. In this study, all the layers present a wurtzite structure highly oriented in the (0002) direction with a carrier concentration in the range of 10^{20} cm^{-3}.

For achieving compact $Al_xIn_{1-x}N$ layers with high surface quality (RMS<2 nm), the substrate temperature must be above 450°C, in particular for the layers under study at this temperature and with a power applied to the aluminum target of 150 W, $Al_xIn_{1-x}N$ layers with a 39% aluminum and a band gap energy of 2 eV are obtained.

These properties make $Al_xIn_{1-x}N$ grown on sapphire substrate appropriate for photoconductors and high reflectivity mirrors in the UV-visible wavelength range.

In particular, we have explored the application of $Al_xIn_{1-x}N$ layers grown on sapphire substrate as photoconductors. The developed devices were characterized, they present high responsivity at low irradiance for wavelengths above the band gap, reaching 7 A/W for an irradiance of 10 W/m^2. The response is strongly sublinear with the optical power, and it decreases smoothly for excitation below the band gap, dropping by more than an order of magnitude at 633 nm. The devices present persistent photoconductivity effects. The general performance of these low cost devices is comparable to AlGaN photoconductors fabricated by MBE or MOVPE.

Perspectives

It will be interesting to span the study to the whole range of composition, because in this work we have focused the study to high indium content $Al_xIn_{1-x}N$ (at least 61% of In content). For it, it will be necessary to increase the power applied to the aluminum target up to 225 W and to reduce the power applied to the indium

target until 20 W. Also it will be possible the use of an additional Al target sputtered by DC current to increase the Al content of the layers.

Another issue to improve is the reduction of the carrier concentration so that the Burstein-Moss effect is diminished and the band gap energy should be red shifted. This can be achieved with the improvement of the sputtering system by including a filter in the nitrogen line so that the oxygen present in the nitrogen is reduced to parts per billion (ppb) and thus the incorporation of this impurity to the layer is decreased. This modification of the sputtering system should be accompanied with a new optimization of the growth of $Al_xIn_{1-x}N$ because the change in the reactive gas can modify the layer properties.

The photoconductors should be further characterized by studying their frequency-response in order to study the trapping centers involved in the photocurrent generation. For it the setup measurement should be modified and a lock-in amplifier and a chopper should be used in order to change the frequency of the measurement.

9.2. $Al_xIn_{1-x}N$ grown on p-silicon (111) by RF sputtering

Conclusions

First the growth of $Al_xIn_{1-x}N$ layers directly on p-Si (111) substrates was optimized by studying the effect of the growth conditions (power applied to the aluminum target and substrate temperature) on the layer properties. All the layers present wurtzite structure highly oriented in the *c*-axis. The aluminum composition can be ranged by changing the power applied to the aluminum target as in sapphire, however it was shown that the substrate temperature barely affects the layer composition.

In these samples the oxygen impurity concentration was measured in the range of ~4% by WDX, this amount of oxygen is partly responsible of the high carrier concentration of the layers.

It has been found that compact layers grown at 550°C and applying 40 W and 150 W to the In and Al targets, respectively, show an Al composition of 36% and they present a RMS surface roughness of 3 nm and a high RT PL emission intensity centered at 1.75 eV.

An AlN buffer layer has been proposed for improving the layer properties of $Al_xIn_{1-x}N$. Its growth on p-Si (111) has been optimized for the growth of the $Al_xIn_{1-x}N$ layers.

The AlN growth has been optimized by studying the effect of the substrate temperature (300 – 700°C), power applied to the aluminum target (150 – 225 W) and Al intermediate layer (0 – 14 nm). The increase of the substrate temperature to 600°C leads to samples with better crystal qualities and smoothest surface roughness, however the sputtering system is limited to 700°C because at higher temperatures the substrate holder suffers from chemical reactions. The increase in the applied power to the aluminum target is related to a decrease in the FWHM of the rocking curve leading to layers with higher crystal quality achieving a minimum at 225 W for layers grown at 450°C. The aluminum intermediate layer effect has been studied at high temperature (600°C) and at high power applied to the aluminum target (225 W) in both cases it has been seen that the intermediate layer does not improve the AlN layer properties.

Once the AlN buffer layer has been improved a set of samples was grown to study the effect of the AlN thickness on the $Al_xIn_{1-x}N$ properties. The buffer layer thickness was ranged from 0 to 25 nm while the $Al_xIn_{1-x}N$ layer thickness was fixed to 80 nm. The growth temperature was fixed to 450°C for avoiding the change in substrate temperature during the AlN and $Al_xIn_{1-x}N$ growth so that the impurities present at the interface are reduced. The nitrogen flow was kept at 6 sccm and the chamber pressure was set at 0.47 Pa. The power applied to the Al target while growing the AlN buffer layer was of 225 W and for the growth of the $Al_xIn_{1-x}N$ layer at 150 W and the power applied to the In target was fixed at 40 W. All the layers are crystalline and present wurtzite structure highly oriented in the *c*-axis independently of the AlN buffer thickness, also it is observed that the buffer layer does not affect to the $Al_xIn_{1-x}N$ composition and that the crystal quality (shown as a reduction of the FWHM of the rocking curve of the (0002) $Al_xIn_{1-x}N$ diffraction peak) is improved when the AlN buffer layer is in the 4 to 15 nm range. In all

cases, compact morphologies are achieved with surface roughness around 1.3 nm. All the layers present low temperature PL centered at 1.8 eV, it being suitable for photovoltaic applications.

These layers ($Al_xIn_{1-x}N$ /AlN/p-Si) have been processed into solar cell devices with a mesa structure and metal contacts on the $Al_xIn_{1-x}N$ layer and silicon substrate. The response of the devices has been studied both in dark and under illumination conditions. The use of an AlN buffer layer improves the operation of the device due to the improvement of the $Al_xIn_{1-x}N$ material. The values extracted from the IV characteristics under dark and illumination conditions show that the best device is the one formed by 4 nm AlN and 80 nm $Al_xIn_{1-x}N$ on p-Si (111). It is the one with lower internal resistance and lower ideality factor and higher short circuit current and open circuit voltage. It is also the one that presents higher EQE.

Perspectives

It is needed to improve the contacts deposited on the silicon substrate to improve their ohmicity and thus improve the solar cell response. It will be interesting to develop macroscopic devices to study the comparison between them and the analyzed microscopic devices. It is also needed a better optimization of the AlN / $Al_xIn_{1-x}N$ layer thicknesses so that the external quantum efficiency of the devices is maximized.

9.3. $Al_xIn_{1-x}N$ grown at low substrate temperature

Conclusions

$Al_xIn_{1-x}N$ layers were grown at low temperatures (RT and 100°C) to study the influence of the growth temperature and substrate (sapphire, p-Si (111) and glass) on the $Al_xIn_{1-x}N$ properties. The obtained layers at these temperatures are polycrystalline oriented in the *c*-axis and with wurtzite structure. An Al composition of 37% has been estimated by HRXRD measurements for $Al_xIn_{1-x}N$ layers grown at low substrate temperatures pointing out to almost fully relaxed layers due to the coincidence with the layer composition obtained by WDX

measurements for $Al_xIn_{1-x}N$ layers grown at 300°C. The increase of the growth temperature leads to a reduction of the FWHM of the rocking curve pointing out to better crystal qualities. The layers grown at low temperature present a closely-packed columnar like morphology with low RMS surface roughness (<3 nm) independently of the substrate and temperature, it is needed to increase the growth temperature to 450°C for $Al_xIn_{1-x}N$ grown on sapphire and to 300°C for layers grown on p-Si (111) to achieve compact layers. The layers present a band gap energy of around 2.4 eV for glass and sapphire substrates and for both growth temperatures. However, there is red shift of the band gap energy when increasing the growth temperature from RT to 300°C, this shift is related with a high Burstein-Moss effect due to the high carrier concentration present in the layers.

It has been demonstrated that is possible to grow high quality $Al_xIn_{1-x}N$ layers at low temperatures so that it is possible the use of flexible substrates and structures that cannot be heated.

Surface plasmon resonance sensor devices have been developed using tapered optical fibers as substrate and a metal dielectric bilayer grown by RF sputtering at RT. The metal layer was an Al layer and the $Al_xIn_{1-x}N$ layer was used as the dielectric layer. Different aspects were studied, first it was considered the effect of the homogeneity of the $Al_xIn_{1-x}N$ layer, for it different samples were grown changing the rotation of the substrate holder and we show that in ternary compounds it is very important to rotate the substrate holder while growing the dielectric layer to increase its homogeneity and thus to obtain narrower transmittance resonance dips and higher sensitivities.

Another parameter that was studied was the composition of the dielectric layer, ranging it between 0 (InN) and 1 (AlN). We demonstrated that it is possible to select the transmittance resonance dip within a range of wavelengths without sensitivity amelioration just changing the composition of the dielectric material.

Finally the effect of the metal layer thickness was studied. Obtaining that the increase of the Al thickness within some limits increases the sensitivity and resonance wavelength although there is an increase in FWHM of the transmittance dip.

The SPR sensor composed by a metal layer of 20 nm Al and a dielectric layer of 60 nm $Al_{0.36}In_{0.64}N$ has the highest coupling strength for the range under study; which makes it useful for high sensitivity measurements for a specific operation wavelength.

Perspectives

It will be interesting to explore the possibility of growing the $Al_xIn_{1-x}N$ layers on flexible substrates such as plastic for developing photoconductors and other wearable devices. For it, the $Al_xIn_{1-x}N$ deposition on this kind of substrate should be optimized taking into account the effect of power applied to In and Al targets and the sputtering pressure and the substrate damaging during growth.

References

[AbLC11] Abbas, Abdennour ; Linman, Matthew J. ; Cheng, Quan: New trends in instrumental design for surface plasmon resonance-based biosensors. In: *Biosensors and Bioelectronics* Bd. 26 (2011), Nr. 5, S. 1815–1824

[ADKA10] Aschenbrenner, T ; Dartsch, H ; Kruse, C ; Anastasescu, M ; Stoica, M ; Gartner, M ; Pretorius, A ; Rosenauer, A ; u. a.: Optical and structural characterization of AlInN layers for optoelectronic applications. In: *Journal of Applied Physics* Bd. 108 (2010), Nr. 6, S. 63533

[AfDI16a] Afzal, Naveed ; Devarajan, Mutharasu ; Ibrahim, Kamarulazizi: Influence of substrate temperature on the growth and properties of reactively sputtered In-rich InAlN films. In: *Journal of Materials Science: Materials in Electronics* Bd. 27 (2016), Nr. 5, S. 4281–4289

[AfDI16b] Afzal, N. ; Devarajan, M. ; Ibrahim, K.: A comparative study on the growth of InAlN films on different substrates. In: *Materials Science in Semiconductor Processing* Bd. 51 (2016), S. 8–14

[AHEA04] Assouar, M. B. ; El Hakiki, M. ; Elmazria, O. ; Alnot, P. ; Tiusan, C.: Synthesis and microstructural characterisation of reactive RF magnetron sputtering AlN films for surface acoustic wave filters. In: *Diamond and Related Materials* Bd. 13 (2004), Nr. 4–8, S. 1111–1115

[AHNA11] Amirhoseiny, M. ; Hassan, Z. ; Ng, S. S. ; Ahmad, M. A.: Characterizations of InN Thin Films Grown on Si (110) Substrate by Reactive Sputtering. In: *Journal of Nanomaterials* Bd. 2011 (2011), S. 579427, 1–7

[Albe03] Albella Martín, José María: *Laminas delgadas y recubrimientos preparación, propiedades y aplicaciones* : CSIC, 2003 — ISBN 8400081668

[Amba98] Ambacher, O: Growth and applications of Group III-nitrides. In: *Journal of Physics D: Applied Physics* Bd. 31 (1998), Nr. 20, S. 2653–2710

[ASGK13] Alvi, Naveed ul Hassan ; Soto Rodriguez, Paul E D ; Gómez, Victor J ; Kumar, Praveen ; Willander, Magnus ; Nötzel, Richard: Highly Sensitive and Fast Anion-Selective InN Quantum Dot Electrochemical Sensors. In: *Applied Physics Express* Bd. 6 (2013), Nr. 11, S. 115201

[BDBK13] Berger, Christoph ; Dadgar, Armin ; Bläsing, Jürgen ; Krost, Alois: In-situ growth monitoring of AlInN/AlGaN distributed bragg reflectors for the UV-spectral range. In: *Journal of Crystal Growth* Bd. 370 (2013), S. 87–91

[BDBL15] Berger, C ; Dadgar, A ; Bläsing, J ; Lesnik, A ; Veit, P ; Schmidt, G ; Hempel, T ; Christen, J ; u. a.: Growth of AlInN/GaN distributed Bragg reflectors with improved interface quality. In: *Journal of Crystal Growth* Bd. 414 (2015), S. 105–109

[BeFi99] Bernardini, F ; Fiorentini, V: Spontaneous versus Piezoelectric Polarization in III-V Nitrides: Conceptual Aspects and Practical Consequences. In: *Phys. Stat. Sol. (B)* Bd. 216 (1999), Nr. 391, S. 391–398

[BeFV97] Bernardini, Fabio ; Fiorentini, Vincenzo ; Vanderbilt, David: Spontaneous polarization and piezoelectric constants of III-V nitrides. In: *Physical Review B* Bd. 56 (1997), Nr. 16, S. 4

[BGMM14] Besleaga, C. ; Galca, A. C. ; Miclea, C. F. ; Mercioniu, I. ; Enculescu, M. ; Stan, G. E. ; Mateescu, A. O. ; Dumitru, V. ; u. a.: Physical properties of AlxIn1-xN thin film alloys sputtered at low temperature. In: *Journal of Applied Physics* Bd. 116 (2014), Nr. 15

[BhHY03] Bhuiyan, Ashraful Ghani ; Hashimoto, Akihiro ; Yamamoto, Akio: Indium nitride (InN): A review on growth, characterization, and properties. In: *Journal of Applied Physics* Bd. 94 (2003), Nr. 5, S. 2779–2808

[BNMN16] Blasco, R. ; Núñez-Cascajero, A. ; Monroy, E. ; Naranjo, F. B. ; Valdueza-Felip, S.: Electrical simulations of thin film AlInN on Silicon heterojunctions deposited by sputtering for photovoltaic applications. In: *European Material Research Society Fall Meeting*, 2016

[BPGH99] Bernede, J C ; Pouzet, J ; Gourmelon, E ; Hadouda, H: Recent studies on photoconductive thin films of binary compounds. In: *Synthetic Metals* Bd. 99 (1999), Nr. 1, S. 45–52

[BRMG09] Briot, O. ; Ruffenach, S. ; Moret, M. ; Gil, B. ; Giesen, Ch ; Heuken, M. ; Rushworth, S. ; Leese, T. ; u. a.: Growth of InN films and nanostructures by MOVPE. In: *Journal of Crystal Growth* Bd. 311 (2009), Nr. 10, S. 2761–2766

[BSKH03] Bhuiyan, Ashraful Ghani ; Sugita, Kenichi ; Kasashima, Ken ; Hashimoto, Akihiro ; Yamamoto, Akio ; Davydov, Valery Yu.: Single-

crystalline InN films with an absorption edge between 0.7 and 2 eV grown using different techniques and evidence of the actual band gap energy. In: *Applied Physics Letters* Bd. 83 (2003), Nr. 23, S. 4788

[BuTa05] Butcher, K. S A ; Tansley, T. L.: InN, latest development and a review of the band-gap controversy. In: *Superlattices and Microstructures* Bd. 38 (2005), Nr. 1, S. 1–37

[BWCT04] Butcher, K. S A ; Wintrebert-Fouquet, M. ; Chen, P. P T ; Tansley, T. L. ; Dou, H. ; Shrestha, S. K. ; Timmers, H. ; Kuball, M. ; u. a.: Nitrogen-rich indium nitride. In: *Journal of Applied Physics* Bd. 95 (2004), Nr. 11 I, S. 6124–6128

[ChSo08] Chaniotakis, Nikos ; Sofikiti, Nikoletta: Novel semiconductor materials for the development of chemical sensors and biosensors: A review. In: *Analytica Chimica Acta* Bd. 615 (2008), Nr. 1

[CWPH14] Chen, Wei Chun ; Wu, Yue Han ; Peng, Chun Yen ; Hsiao, Chien Nan ; Chang, Li: Effect of In/Al ratios on structural and optical properties of InAlN films grown on Si(100) by RF-MOMBE. In: *Nanoscale Research Letters* Bd. 9 (2014), Nr. 1, S. 1–7

[CWTY14] Chen, Wei-chun ; Wu, Yue-han ; Tian, Jr ; Yen, Tzu-chun ; Lin, Pei-yin ; Chen, Jr-yu ; Hsiao, Chien-nan ; Chang, Li: Effect of Growth Temperature on Structural Quality of In-Rich InxAl1-xN Alloys on Si (111) Substrate by RF-MOMBE. In: *ISRN Nanomaterials* Bd. 2014 (2014)

[DKSE02] Davydov, V. Yu ; Klochikhin, A. A. ; Seisyan, R. P. ; Emtsev, V. V. ; Ivanov, S. V. ; Bechstedt, F. ; Furthmüller, J. ; Harima, H. ; u. a.: Absorption and emission of hexagonal InN. Evidence of narrow fundamental band gap. In: *Physica Status Solidi (B) Basic Research* Bd. 229 (2002), Nr. 3, S. 1972–1974 — ISBN 1521-3951

[DLBA10] Darakchieva, V ; Lorenz, K ; Barradas, N P ; Alves, E ; Monemar, B: Hydrogen in InN : A ubiquitous phenomenon in molecular beam epitaxy grown material. In: *Applied Physics Letters* Bd. 96 (2010), S. 81907

[DXCL09] Dong, C J ; Xu, M ; Chen, Q Y ; Liu, F S ; Zhou, H P ; Wei, Y ; Ji, H X: Growth of well-oriented AlxIn1-xN films by sputtering at low temperature. In: *Journal of Alloys and Compounds* Bd. 479 (2009), Nr. 1, S. 812–815

[ENDV11] Esteban, Óscar ; Naranjo, Fernando B. ; Díaz-Herrera, Natalia ; Valdueza-Felip, Sirona ; Navarrete, María Cruz ; González-Cano, Agustín: High-sensitive SPR sensing with Indium Nitride as a dielectric overlay of optical fibers. In: *Sensors and Actuators, B: Chemical* Bd. 158 (2011), Nr. 1, S. 372–376

[ESCA15] Espinosa, Nayeli ; Schwarz, Stefan U. ; Cimalla, Volker ; Ambacher, Oliver: Detection of different target-DNA concentrations with highly sensitive AlGaN/GaN high electron mobility transistors. In: *Sensors and Actuators B: Chemical* Bd. 210 (2015), S. 633–639

[FeBe02] Ferhat, M. ; Bechstedt, F.: First-principles calculations of gap bowing in InxGa1-xN and InxAl1-xN alloys: Relation to structural and thermodynamic properties. In: *Physical Review B* Bd. 65 (2002), Nr. 7, S. 75213

[FIWO04] Fujimori, Takao ; Imai, Hitoshi ; Wakahara, Akihiro ; Okada, Hiroshi ; Yoshida, Akira ; Shibata, Tomohiko ; Tanaka, Mitsuhiro: Growth and characterization of AlInN on AlN template. In: *Journal of Crystal Growth* Bd. 272 (2004), Nr. 1–4, S. 381–385

[GBED05] González-Cano, Agustín ; Bueno, Francisco-Javier ; Esteban, Oscar ; Díaz-Herrera, Natalia ; Navarrete, María-Cruz: Multiple surface-plasmon resonance in uniform-waist tapered optical fibers with an asymmetric double-layer deposition. In: *Applied Optics* Bd. 44 (2005), Nr. 4, S. 519–526

[GCGG14] Gogneau, Noelle ; Chrétien, Pascal ; Galopin, Elisabeth ; Guilet, Stephane ; Travers, Laurent: Impact of the GaN nanowire polarity on energy harvesting Impact of the GaN nanowire polarity on energy harvesting. In: *Applied Physics Letters* Bd. 104 (2014), Nr. 213105, S. 1–5

[GCZD15] Guo, Luan ; Chen, Guangde ; Zhu, Youzhang ; Duan, Xiangyang ; Ye, Honggang: The growth of Sea-urchin-like AlN nanostructures by modified CVD and their Field Emission properties. In: *Journal of Crystal Growth* Bd. 426, Elsevier (2015), S. 49–53

[GEHW16] Green, Martin A. ; Emery, Keith ; Hishikawa, Yoshihiro ; Warta, Wilhelm ; Dunlop, Ewan D.: Solar cells efficiency tables (version 48). In: *Prog. Photovolt: Res. Appl.* Bd. 24 (2016), Nr. 7, S. 905–913

[Gil98] Gil, Bernard: *Group III Nitride Semiconductor Compounds Physics and Applications* : Oxford Science Publications, 1998 — ISBN 9780198501596

[GITM09] Giordano, C. ; Ingrosso, I. ; Todaro, M. T. ; Maruccio, G. ; De Guido, S. ; Cingolani, R. ; Passaseo, A. ; De Vittorio, M.: AlN on polysilicon piezoelectric cantilevers for sensors/actuators. In: *Microelectronic Engineering* Bd. 86 (2009), Nr. 4–6, S. 1204–1207

[GKBB06] Gallinat, Chad S. ; Koblmüller, Gregor ; Brown, Jay S. ; Bernardis, Sarah ; Speck, James S. ; Chern, Grace D. ; Readinger, Eric D. ; Shen, Hongen ; u. a.: In-polar InN grown by plasma-assisted molecular beam epitaxy. In: *Applied Physics Letters* Bd. 89 (2006), S. 32109

[GNED14] González-Cano, A. ; Navarrete, M.C. ; Esteban, Ó ; Díaz-Herrera, Natalia: Plasmonic sensors based on doubly-deposited tapered optical fibers. In: *Sensors* Bd. 14 (2014), Nr. 3, S. 4791–4805

[GOKT07] Guo, Q X ; Okazaki, Y ; Kume, Y ; Tanaka, T ; Nishio, M ; Ogawa, H: Reactive sputter deposition of AlInN thin films. In: *Journal of Crystal Growth* Bd. 300 (2007), Nr. 1, S. 151–154

[Gree79] Green, Robert: Hall Effect Measurements in Materials Characterization. In: *White paper* (1879), Nr. 440, S. 1–12

[GSMN99] Guo, Qixin ; Shingai, Nobuhiro ; Mitsuishi, Yoshiaki ; Nishio, Mitsuhiro ; Ogawa, Hiroshi: Effects of nitrogen/argon ratio on composition and structure of InN films prepared by r.f. magnetron sputtering. In: *Thin Solid Films* Bd. 343–344 (1999), S. 524–527

[GSNO98] Guo, Qixin ; Shingai, Nobuhiro ; Nishio, Mitsuhiro ; Ogawa, Hiroshi: Deposition of InN thin films by radio frequency magnetron sputtering. In: *Journal of Crystal Growth* Bd. 189–190 (1998), S. 466–470

[GTNO06] Guo, Q.X. ; Tanaka, T. ; Nishio, M. ; Ogawa, H.: Growth properties of AlN films on sapphire substrates by reactive sputtering. In: *Vacuum* Bd. 80 (2006), Nr. 7, S. 716–718

[GTNO08] Guo, Qixin ; Tanaka, Tooru ; Nishio, Mitsuhiro ; Ogawa, Hiroshi: Structural and Optical Properties of AlInN Films Grown on Sapphire Substrates. In: *Japanese Journal of Applied Physics* Bd. 47 (2008), Nr. 1S, S. 612

[GYTN03] Guo, Qixin ; Yahata, Kousuke ; Tanaka, Tooru ; Nishio, Mitsuhiro ; Ogawa, Hiroshi: Growth and characterization of reactive sputtered AlInN films. In: *Physica Status Solidi (C)* Bd. 0 (2003), Nr. 7, S. 2533–2536

[Hana09] Hanada, T: Basic Properties of ZnO, GaN, and Related Materials. In: *Oxide and Nitride Semiconductors*, 2009 — ISBN 9783540888468, S. 1–19

[Hash94] Hashimoto, Akihiro: Metalorganic chemical vapor deposition growth of InN for InN / Si tandem solar cell ISb. In: *Solar Energy Materials and Solar Cells* Bd. 35 (1994)

[HaWo16] Harotoonian, Vache ; Woodall, Jerry M.: Growth and Characterization of Single Crystalline InN Grown on GaN by RF Sputtering for Robust Schottky Contacts. In: *Journal of Electronic Materials* Bd. 45 (2016), Nr. 12, S. 6305–6309

[HBDD07] Hums, C ; Bläsing, J ; Dadgar, A ; Diez, A ; Hempel, T ; Christen, J ; Krost, A ; Lorenz, K ; u. a.: Metal-organic vapor phase epitaxy and

properties of AlInN in the whole compositional range. In: *Applied Physics Letters* Bd. 90 (2007), Nr. 2, S. 22105

[HCFG10] He, Hong ; Cao, Yongge ; Fu, Renli ; Guo, Wang ; Huang, Zhi ; Wang, Meili ; Huang, Changgang ; Huang, Jiquan ; u. a.: Band gap energy and bowing parameter of In-rich InAlN films grown by magnetron sputtering. In: *Applied Surface Science* Bd. 256 (2010), Nr. 6, S. 1812–1816

[HCFW10] He, Hong ; Cao, Yongge ; Fu, Renli ; Wang, Hai ; Huang, Jiquan ; Huang, Changgang ; Wang, Meili ; Deng, Zhonghua: Structure and optical properties of InN and InAlN films grown by rf magnetron sputtering. In: *Journal of Materials Science: Materials in Electronics* Bd. 21 (2010), Nr. 7, S. 676–681

[HDDS10] Han, Qifeng ; Duan, Chenghong ; Du, Guoping ; Shi, Wangzhou ; Ji, Lechun: Magnetron sputter epitaxy and characterization of wurtzite AlInN on Si(111) substrates. In: *Journal of Electronic Materials* Bd. 39 (2010), Nr. 5, S. 489–493

[HFGC07] Horcas, I. ; Fernández, R. ; Gómez-Rodríguez, J. M. ; Colchero, J. ; Gómez-Herrero, J. ; Baro, a. M.: WSXM: A software for scanning probe microscopy and a tool for nanotechnology. In: *Review of Scientific Instruments* Bd. 78 (2007), Nr. 1, S. 13705

[HGCA02] Huttel, Y ; Gomez, H ; Cebollada, A ; Armelles, G ; Alonso, M I: Epitaxial growth of AlN on sapphire (0001) by sputtering : a structural , morphological and optical study. In: *Journal of Crystal Growth* Bd. 242 (2002), S. 116–123 — ISBN 3491806070

[HoBo00] Honsberg, Christiana ; Bowden, Stuart: *PVEducation.org*. URL http://pveducation.org

[Homo08] Homola, Jirí: Surface plasmon resonance sensors for detection of chemical and biological species. In: *Chemical reviews* Bd. 108 (2008), Nr. 2, S. 462–493

[Homo97] Homola, Jiří: On the sensitivity of surface plasmon resonance sensors with spectral interrogation. In: *Sensors and Actuators B: Chemical* Bd. 41 (1997), S. 207–211

[HoYG99] Homola, Jiří ; Yee, Sinclair S. ; Gauglitz, Günter: Surface plasmon resonance sensors: review. In: *Sensors and Actuators B: Chemical* Bd. 54 (1999), Nr. 1, S. 3–15

[Inc00] Inc., Clear Metals: *Technology*. URL http://clearmetalsinc.com/technology/

[Jeff10] Jeff Hetch: *PHOTONIC FRONTIERS: SHORTWAVE LASER DIODES:*

The quest for practical green laser diodes. URL http://www.laserfocusworld.com/articles/2010/12/photonic-frontiers-shortwave-laser-diodes-the-quest-for-practical-green-laser-diodes.html

[JFHK07] Jani, Omkar ; Ferguson, Ian ; Honsberg, Christiana ; Kurtz, Sarah: Design and characterization of GaNInGaN solar cells. In: *Applied Physics Letters* Bd. 91 (2007), Nr. 13, S. 13–16

[JiSG09] Jiang, L F ; Shen, W Z ; Guo, Q X: Temperature dependence of the optical properties of AlInN. In: *Journal of Applied Physics* Bd. 106 (2009), Nr. 1, S. 13515

[JJLK15] Jeong, Min Woo ; Jeon, Seung Won ; Lee, Sang Hun ; Kim, Yongchan: Effective heat dissipation and geometric optimization in an LED module with aluminum nitride (AlN) insulation plate. In: *Applied Thermal Engineering* Bd. 76 (2015), S. 212–219

[JoKh01] Jose, Joshy ; Khadar, M Abdul: Role of grain boundaries on the electrical conductivity of nanophase zinc oxide. In: *Materials Science and Engineering: A* Bd. 304–306 (2001), S. 810–813

[KAGR03] Koblmueller, G. ; Averbeck, R. ; Geelhaar, L. ; Riechert, H. ; Hösler, W. ; Pongratz, P.: Growth diagram and morphologies of AlN thin films grown by molecular beam epitaxy. In: *Journal of Applied Physics* Bd. 93 (2003), Nr. 12, S. 9591–9596

[KBBF10] Krost, a. ; Berger, C. ; Bläsing, J. ; Franke, a. ; Hempel, T. ; Dadgar, a. ; Christen, J.: Strain evaluation in AlInN/GaN Bragg mirrors by in situ curvature measurements and ex situ x-ray grazing incidence and transmission scattering. In: *Applied Physics Letters* Bd. 97 (2010), Nr. 18, S. 3–6

[KeAr00] Kelly, P.J. ; Arnell, R.D.: Magnetron sputtering: a review of recent developments and applications. In: *Vacuum* Bd. 56 (2000), Nr. 3, S. 159–172

[KeBO91] Kenny, R.P. ; Birks, T.A. ; Oakley, K.P.: Control of optical fibre taper shape. In: *Electronics Letters* Bd. 27 (1991), Nr. 18, S. 1654

[KKIK07] Kamimura, Jumpei ; Kouno, Tetsuya ; Ishizawa, Shunsuke ; Kikuchi, Akihiko ; Kishino, Katsumi: Growth of high-In-content InAlN nanocolumns on Si (1 1 1) by RF-plasma-assisted molecular-beam epitaxy. In: *Journal of Crystal Growth* Bd. 300 (2007), Nr. 1, S. 160–163

[KMCD11] Kim-Chauveau, H. ; de Mierry, P. ; Chauveau, J-M. ; Duboz, J-Y.: The influence of various MOCVD parameters on the growth of Al1−xInxN ternary alloy on GaN templates. In: *Journal of Crystal Growth* Bd. 316 (2011), Nr. 1, S. 30–36

[KrRa68] Kretschmann, E. ; Raether, H.: Radiative Decay of Non Radiative Surface Plasmons Excited by Light. In: *Zeitschrift fur Naturforschung - Section A Journal of Physical Sciences* Bd. 23 (1968), Nr. 12

[KSKF97] Karmann, S ; Schenk, H.P.D ; Kaiser, U ; Fissel, a ; Richter, Wo: Growth of columnar aluminum nitride layers on Si(111) by molecular beam epitaxy. In: *Materials Science and Engineering: B* Bd. 50 (1997), S. 228–232

[KuKF89] Kubota, K. ; Kobayashi, Y. ; Fujimoto, K.: Preparation and properties of III-V nitride thin films. In: *Journal of Applied Physics* Bd. 66 (1989), Nr. 7

[KZWC12] Kuang, Xu Ping ; Zhang, Hua Yu ; Wang, Gui Gen ; Cui, Lin ; Zhu, Can ; Jin, Lei ; Sun, Rui ; Han, Jie Cai: AlN films prepared on 6H-SiC substrates under various sputtering pressures by RF reactive magnetron sputtering. In: *Applied Surface Science* Bd. 263 (2012), S. 62–68

[LDNH01] Lukitsch, M. J. ; Danylyuk, Y. V. ; Naik, V. M. ; Huang, C. ; Auner, G. W. ; Rimai, L. ; Naik, R.: Optical and electrical properties of Al1-xInxN films grown by plasma source molecular-beam epitaxy. In: *Applied Physics Letters* Bd. 79 (2001), Nr. 5, S. 632

[LDTD13] Liu, H F ; Dolmanan, S B ; Tripathy, S ; Dalapati, G K ; Tan, C C ; Chi, D Z: Effects of AlN thickness on structural and transport properties of In-rich n-AlInN/AlN/p-Si(0 0 1) heterojunctions grown by magnetron sputtering. In: *Journal of Physics D: Applied Physics* Bd. 46 (2013), Nr. 9, S. 95106

[LFAW06] Lorenz, K. ; Franco, N. ; Alves, E. ; Watson, I. M. ; Martin, R. W. ; O'Donnell, K. P.: Anomalous ion channeling in AlInN/GaN bilayers: Determination of the strain state. In: *Physical Review Letters* Bd. 97 (2006), Nr. 8, S. 1–4

[LGBN99] Leroux, M ; Grandjean, N. ; Beaumont, B. ; Nataf, G. ; Semond, F. ; Massies, J. ; Gibart, P.: Temperature quenching of photoluminescence intensities in undoped and doped GaN. In: *Journal of Applied Physics* Bd. 86 (1999), Nr. 7, S. 3721–3728

[LGHK01] Ledoux, G. ; Guillois, O. ; Huisken, F. ; Kohn, B. ; Porterat, D. ; Reynaud, C.: Crystalline silicon nanoparticles as carriers for the extended red emission. In: *Astronomy and Astrophysics* Bd. 377 (2001), S. 707–720

[LGWC08] Li, B. K. ; Ge, W. K. ; Wang, J. N. ; Chen, K. J.: Persistent photoconductivity and carrier transport in AlGaNGaN heterostructures treated by fluorine plasma. In: *Applied Physics Letters* Bd. 92 (2008), Nr. 8

[LiYK04] Liou, B T ; Yen, S H ; Kuo, Y K: Vegard's law deviation in band gaps and bowing parameters of the wurtzite III-nitride ternary alloys. In:

Semiconductor Lasers and Applications Ii Bd. 5628 (2004), S. 296–305 — ISBN 0277-786X

[LONL02] Li, J ; Oder, T N ; Nakarmi, M L ; Lin, J Y ; Jiang, H X ; Al, Mg-doped: Optical and electrical properties of Mg-doped p-type AlxGa1-xN. In: *Applied Physics Letters* Bd. 80 (2002), Nr. 7, S. 1210–1212

[LSES03] Lu, Hai ; Schaff, William J. ; Eastman, Lester F. ; Stutz, C. E.: Surface charge accumulation of InN films grown by molecular-beam epitaxy. In: *Applied Physics Letters* Bd. 82 (2003), Nr. 11, S. 1736–1738 — ISBN 00036951

[LTDC12] Liu, H F ; Tan, C C ; Dalapati, G K ; Chi, D Z: Magnetron-sputter deposition of high-indium-content n-AlInN thin film on p-Si(001) substrate for photovoltaic applications. In: *Journal of Applied Physics* Bd. 112 (2012), Nr. 6, S. 63114

[LüDW13] Lü, Mo ; Dong, Chengjun ; Wang, Yiding: Proposal and achievement of a relatively Al-rich interlayer for In-rich AlxIn1−xN films deposition. In: *Journal of Wuhan University of Technology-Mater. Sci. Ed.* Bd. 28 (2013), Nr. 5, S. 868–875

[LWGX08] Luo, Weijun ; Wang, Xiaoliang ; Guo, Lunchun ; Xiao, Hongling ; Wang, Cuimei ; Ran, Junxue ; Li, Jianping ; Li, Jinmin: Influence of AlN buffer layer thickness on the properties of GaN epilayer on Si(1 1 1) by MOCVD. In: *Microelectronics Journal* Bd. 39 (2008), Nr. 12, S. 1710–1713

[LYTT08] Lobanova, A. V. ; Yakovlev, E. V. ; Talalaev, R. A. ; Thapa, S. B. ; Scholz, F.: Growth conditions and surface morphology of AlN MOVPE. In: *Journal of Crystal Growth* Bd. 310 (2008), Nr. 23, S. 4935–4938

[Mala03] Malakhov, V. Ya: Potential PV materials-based InN thin films: Fabrication, structural and optical properties. In: *Solar Energy Materials and Solar Cells* Bd. 76 (2003), Nr. 4, S. 637–646

[März09] März: *High Resolution X-Ray Diffraction: User guide manual*, 2009

[MMDS99] Martin, R W ; Middleton, P G ; Donnell, K P O ; Stricht, W Van Der: Exciton localization and the Stokes' shift in InGaN epilayers. In: *Applied Physics Letters* Bd. 74 (1999), Nr. 2, S. 263

[MMGI97] Muñoz, E. ; Monroy, E. ; Garrido, J a. ; Izpura, I. ; Sa, F J. ; Calleja, E.: Photoconductor gain mechanisms in GaN ultraviolet detectors. In: *Applied Physics Letters* Bd. 71 (1997), Nr. 7, S. 870–872

[MNJP15] Monteagudo-Lerma, Laura ; Naranjo, Fernando ; Jimenez-Rodriguez, Marco ; Postigo, Pablo ; Barrios, Elena ; Corredera, Pedro ; Gonzalez-Herraez, Miguel: InN-based optical waveguides developed by RF sputtering for all-optical applications at 1.55 um. In: *IEEE*

Photonics Technology Letters Bd. 27 (2015), Nr. 17, S. 1857–1860

[Mont15] Monteagudo-Lerma, Laura: *Development of III-nitride-based waveguides for application in all-optical integrated circuits at 1.55 um*, Universidad de Alcalá, 2015

[MoOC03] Monroy, E ; Omnes, F ; Calle, F: Wide-bandgap semiconductor ultraviolet photodetectors. In: *Semiconductor Science and Technology* Bd. 18 (2003), Nr. 4, S. R33–R51

[MoVi09] Moram, M A ; Vickers, M E: X-ray diffraction of III-nitrides. In: *Reports on Progress in Physics* Bd. 72 (2009), Nr. 3, S. 36502

[MSTW15] Muziol, G. ; Siekacz, M. ; Turski, H. ; Wolny, P. ; Grzanka, S. ; Grzanka, E. ; Feduniewicz-Żmuda, A. ; Borysiuk, J. ; u. a.: High power nitride laser diodes grown by plasma assisted molecular beam epitaxy. In: *Journal of Crystal Growth* Bd. 425 (2015), S. 398–400

[MVNG13] Monteagudo-Lerma, L ; Valdueza-Felip, S ; Núñez-Cascajero, A ; González-Herráez, M ; Monroy, E ; Naranjo, F B: Two-step method for the deposition of AlN by radio frequency sputtering. In: *Thin Solid Films* Bd. 545 (2013), Nr. 0, S. 149–153

[MVNR16] Monteagudo-Lerma, L. ; Valdueza-Felip, S. ; Núñez-Cascajero, A. ; Ruiz, A. ; González-Herráez, M. ; Monroy, E. ; Naranjo, F. B.: Morphology and arrangement of InN nanocolumns deposited by radio-frequency sputtering: Effect of the buffer layer. In: *Journal of Crystal Growth* Bd. 434, Elsevier (2016), S. 13–18

[Nati16] National Center for Photovoltaics: *Best research cells efficencies*. URL https://www.nrel.gov/pv/

[NCFI11] Neufeld, Carl J. ; Cruz, Samantha C. ; Farrell, Robert M. ; Iza, Michael ; Lang, Jordan R. ; Keller, Stacia ; Nakamura, Shuji ; Denbaars, Steven P. ; u. a.: Effect of doping and polarization on carrier collection in InGaN quantum well solar cells. In: *Applied Physics Letters* Bd. 98 (2011), Nr. 24, S. 243507

[NeEk96] Neumayer, Deborah A ; Ekerdt, John G: Growth of Group III Nitrides. A Review of Precursors and Techniques. In: *Chemistry of Materials* Bd. 8 (1996), Nr. 1, S. 9–25

[NEMG16] Núñez-Cascajero, A. ; Estéban ; Méndez, J. A. ; González-Herráez, M. ; Naranjo, F. B.: Infrared SPR sensing with III-nitride dielectric layers. In: *Sensors and Actuators, B: Chemical* Bd. 223 (2016), S. 768–773

[NFTK07] Naoi, H. ; Fujiwara, K. ; Takado, S. ; Kurouchi, M. ; Muto, D. ; Araki, T. ; Na, H. ; Nanishi, Y.: Growth of in-rich in x Al 1-x N films on

(0001) sapphire by RF-MBE and their properties. In: *Journal of Electronic Materials* Bd. 36 (2007), Nr. 10, S. 1313–1319

[NJMG17] Núñez-Cascajero, Arántzazu ; Jiménez-Rodríguez, Marco ; Monroy, Eva ; González-Herráez, Miguel ; Naranjo, Fernando B.: Development of AlInN photoconductors deposited by sputtering. In: *Physica Status Solidi (a)* (2017), S. 1600780

[NMVN16] Núñez-Cascajero, Arántzazu ; Monteagudo-Lerma, Laura ; Valdueza-Felip, Sirona ; Navío, Cristina ; Monroy, Eva ; González-Herráez, Miguel ; Naranjo, Fernando B.: Study of high In-content AlInN deposition on p-Si (111) by RF-sputtering. In: *Japanese Journal of Applied Physics* Bd. 55 (2016), S. 05FB07

[NVMM16] Núñez-Cascajero, Arántzazu ; Valdueza-Felip, Sirona ; Monteagudo-Lerma, Laura ; Monroy, Eva ; Taylor-Shaw, E ; Martin, R.W. Robert ; González-Herráez, Miguel ; Naranjo, Fernando B. ; u. a.: In-rich Al x In 1 - x N grown by RF-sputtering on sapphire : from closely-packed columnar to high-surface quality compact layers. In: *Journal of Physics D: Applied Physics* Bd. 50 (2016), S. 1–9

[Patt39] Patterson, A L: The Scherrer Formula for X-Ray Particle Size Determination. In: *Physical Review* Bd. 56 (1939), Nr. 10, S. 978–982

[PBHG03] Petrov, I. ; Barna, P.B. ; Hultman, L. ; Greene, J.E.: Microstructural evolution during film growth. In: *Journal of Vacuum Science & Technology A: Vacuum, Surfaces, and Films* Bd. 21 (2003), Nr. 5, S. S117

[PHMČ03] Piliarik, M. ; Homola, J. ; Maníková, Z. ; Čtyroký, J.: Surface plasmon resonance sensor based on a single-mode polarization-maintaining optical fiber. In: *Sensors and Actuators, B: Chemical.* Bd. 90, 2003, S. 236–242

[PiBo52] Pines, David ; Bohm, David: A Collective Description of Electron Interactions: II. Collective vs Individual Particle Aspects of the Interactions. In: *Physical Review* Bd. 85 (1952), Nr. 2, S. 338–353

[PMSC02] Pau, J L ; Monroy, E ; Sánchez-García, M A ; Calleja, E. ; Muñoz, E.: AlGaN ultraviolet photodetectors grown by molecular beam epitaxy on Si (111) substrates. In: *Materials Science* Bd. 93 (2002), S. 159–162

[Poly00] Polyanskiy, M. N.: *Refractive index database.* URL http://refractiveindex.info

[PPQO97] Peng, T ; Piprek, J ; Qiu, G ; Olowolafe, J O ; Unruh, K M ; Swann, C P ; Schubert, E F.: Band gap bowing and refractive index spectra of polycrystalline AlxIn1-xN films deposited by sputtering. In: *Applied Physics Letters* Bd. 71 (1997), Nr. 17, S. 2439–2441

[PSPS13] Priambodo, Purnomo Sidi ; Sukoco, Didik ; Purnomo, Wahyudi ; Sudibyo, Harry ; Hartanto, Djoko: Electric Energy Management and Engineering in Solar Cell System. In: Morales-Acevedo, A. B. T.-S. C.-R. and A. P. (Hrsg.): *Solar cells- Research and applicantion perspectives* : InTech, 2013 — ISBN 9789533070865

[PSZO06] Pu, X D ; Shen, W Z ; Zhang, Z Q ; Ogawa, H ; Guo, Q X: Growth and depth dependence of visible luminescence in wurtzite InN epilayers. In: *Applied Physics Letters* Bd. 88 (2006), Nr. 15, S. 151904

[Pvli00] PV Lighthouse, Pty: *PV Lighthouse*. URL www.pvlighthouse.com.au

[Raet88] Raether, H: *Surface Plasmons on Smooth and Rough Surfaces and on Gratings* : Springer, 1988 — ISBN 978-3-540-17363-2

[RIAV12] Rodríguez-Madrid, J. G. ; Iriarte, G. F. ; Araujo, D. ; Villar, M. P. ; Williams, O. A. ; Müller-Sebert, W. ; Calle, F.: Optimization of AlN thin layers on diamond substrates for high frequency SAW resonators. In: *Materials Letters* Bd. 66 (2012), Nr. 1, S. 339–342

[Sánc00] Sánchez-García, M A: *Crecimiento y caracterización de Nítruros del grupo III sobre Si (111) por epitaxia de haces moleculares Tesis Doctoral*, Universidad Politécnica de Madrid, 2000

[SASC97] Shikanai, Amane ; Azuhata, Takashi ; Sota, Takayuki ; Chichibu, Shigefusa ; Kuramata, Akito ; Horino, Kazuhiko ; Nakamura, Shuji: Biaxial strain dependence of exciton resonance energies in wurtzite GaN. In: *Journal of Applied Physics* Bd. 81 (1997), Nr. 1, S. 417

[SaTe91] Saleh, Bahaa E. A. ; Teich, Malvin Carl: *Fundamentals of photonics*, 1991 — ISBN 0471839655

[SCGU10] Sofikiti, N. ; Chaniotakis, N. ; Grandal, J. ; Utrera, M. ; Sánchez-García, M. A. ; Calleja, E.: GaN and InN nanocolumns as electrochemical sensing elements: Potentiometric response to KCl, pH and urea. In: *Materials Letters* Bd. 64 (2010), Nr. 12, S. 1332–1335

[SCTP13] Schulz, Stefan ; Caro, Miguel a. ; Tan, Lay-Theng ; Parbrook, Peter J. ; Martin, Robert W. ; O'Reilly, Eoin P.: Composition-Dependent Band Gap and Band-Edge Bowing in AlInN: A Combined Theoretical and Experimental Study. In: *Applied Physics Express* Bd. 6 (2013), Nr. 12, S. 121001

[SDKK09] Sahonta, S. L. ; Dimitrakopulos, G. P. ; Kehagias, Th ; Kioseoglou, J. ; Adikimenakis, A. ; Iliopoulos, E. ; Georgakilas, A. ; Kirmse, H. ; u. a.: Mechanism of compositional modulations in epitaxial InAlN films grown by molecular beam epitaxy. In: *Applied Physics Letters* Bd. 95 (2009), Nr. 2

[Sesh02] Seshan, Krishna: *Handbook of Thin-Film Deposition Processes and Techniques: Principles, Methods, Equipment and Applications* : Noyes Publications, 2002 — ISBN 0815514425

[ShJG07] Sharma, Anuj K. ; Jha, Rajan ; Gupta, B. D.: Fiber-optic sensors based on surface plasmon resonance: A comprehensive review. In: *IEEE Sensors Journal* Bd. 7 (2007), Nr. 8

[SHKY02] Saito, Y. ; Harima, H. ; Kurimoto, E. ; Yamaguchi, T. ; Teraguchi, N. ; Suzuki, A. ; Araki, T. ; Nanishi, Y.: Growth temperature dependence of indium nitride crystalline quality grown by RF-MBE. In: *Physica Status Solidi (B) Basic Research* Bd. 234 (2002), Nr. 3, S. 796–800

[SHTW15] Singh, Meenakshi ; Holzinger, Michael ; Tabrizian, Maryam ; Winters, Sinéad ; Berner, Nina C. ; Cosnier, Serge ; Duesberg, Georg S.: Noncovalently functionalized monolayer graphene for sensitivity enhancement of surface plasmon resonance immunosensors. In: *Journal of the American Chemical Society* Bd. 137 (2015), Nr. 8, S. 2800–2803

[SMBM15] Saidi, I. ; Mejri, H. ; Baira, M. ; Maaref, H.: Electronic and transport properties of AlInN/AlN/GaN high electron mobility transistors. In: *Superlattices and Microstructures* Bd. 84 (2015), S. 113–125

[SPHB05] Seppänen, T. ; Persson, P. O. Å. ; Hultman, L. ; Birch, J. ; Radnóczi, G. Z.: Magnetron sputter epitaxy of wurtzite Al(1-x)In(x)N by dual reactive dc magnetron sputter deposition. In: *Journal of Applied Physics* Bd. 97 (2005), Nr. 8, S. 83503

[SPPV07] Sharma, Sangita ; Patel, Pragnesh B. ; Patel, Rignesh S. ; Vora, J. J.: Density and Comparative Refractive Index Study on Mixing Properties of Binary Liquid Mixtures of Eucalyptol with Hydrocarbons at 303.15, 308.15 and 313.15 K. In: *E-Journal of Chemistry* Bd. 4 (2007), Nr. 3, S. 343–349

[Spro00] Sproul, Alistar: Understanding the p-n Junction. In: *Resources for the secondary science teacher* — ISBN 9789287037480 9287037485

[StKB95] Stevens, K. S. ; Kinniburgh, M. ; Beresford, R.: Photoconductive ultraviolet sensor using Mg-doped GaN on Si(111). In: *Applied Physics Letters* Bd. 66 (1995), Nr. 25, S. 3518–3520

[Stri92] Strite, S.: GaN, AlN, and InN: A review. In: *Journal of Vacuum Science & Technology B: Microelectronics and Nanometer Structures* Bd. 10 (1992), Nr. 4, S. 1237

[TaFo86] Tansley, T L ; Foley, C P: Optical band gap of indium nitride. In: *J. Appl. Phys.* Bd. 59 (1986), Nr. 9, S. 3241–3244

[TaKa11] Taniyasu, Yoshitaka ; Kasu, Makoto: Polarization property of deep-

ultraviolet light emission from C-plane AlN/GaN short-period superlattices. In: *Applied Physics Letters* Bd. 99 (2011), Nr. 25, S. 251112

[TaKM06] Taniyasu, Yoshitaka ; Kasu, Makoto ; Makimoto, Toshiki: An aluminium nitride light-emitting diode with a wavelength of 210[thinsp]nanometres. In: *Nature* Bd. 441 (2006), Nr. 7091, S. 325–328

[TaKM07] Taniyasu, Yoshitaka ; Kasu, Makoto ; Makimoto, Toshiki: Threading dislocations in heteroepitaxial AlN layer grown by MOVPE on SiC (0001) substrate. In: *Journal of Crystal Growth* Bd. 298 (2007), S. 310–315

[TCIY06] Terashima, Wataru ; Che, Song Bek ; Ishitani, Yoshihiro ; Yoshikawa, Akihiko: Growth and characterization of AlInN ternary alloys in whole composition range and fabrication of InN/AlInN multiple quantum wells by RF molecular beam epitaxy. In: *Japanese Journal of Applied Physics* Bd. 45 (2006), Nr. 21, S. L539–L542

[UsMG15] Usha, Sruthi ; Mishra, Satyendra ; Gupta, Banshi: Fabrication and Characterization of a SPR Based Fiber Optic Sensor for the Detection of Chlorine Gas Using Silver and Zinc Oxide. In: *Materials* Bd. 8 (2015), Nr. 5, S. 2204–2216

[Vald11] Valdueza-Felip, Sirona: *Nitride-based semiconductor nanostructures for applications in optical communications at 1.5 um*, Universidad de Alcalá, 2011

[Vars67] Varshni, Y.P.: Temperature dependence of the energy gap in semiconductors. In: *Physica* Bd. 34 (1967), Nr. 1, S. 149–154

[Vega21] Vegard, L: Die Konstitution der Mischkristalle und die Raumfüllung der Atome. In: - *Zeitschrift für Physik* Bd. 5 (1921), Nr. 1, S. 17–26

[VIMG12] Valdueza-Felip, S. ; Ibáñez, J. ; Monroy, E. ; González-Herráez, M. ; Artús, L. ; Naranjo, F. B.: Improvement of InN layers deposited on Si(111) by RF sputtering using a low-growth-rate InN buffer layer. In: *Thin Solid Films* Bd. 520 (2012), Nr. 7, S. 2805–2809

[ViMM03] Villatoro, Joel ; Monzón-Hernández, David ; Mejía, Efrain: Fabrication and modeling of uniform-waist single-mode tapered optical fiber sensors. In: *Applied optics* Bd. 42 (2003), Nr. 13, S. 2278–2283

[VNGL10] Valdueza-Felip, S. ; Naranjo, F. B. ; González-Herráez, M. ; Lahourcade, L. ; Monroy, E. ; Fernández, S.: Influence of deposition conditions on nanocrystalline InN layers synthesized on Si(1 1 1) and GaN templates by RF sputtering. In: *Journal of Crystal Growth* Bd. 312 (2010), Nr. 19, S. 2689–2694

[VNGL11] Valdueza-Felip, Sirona ; Naranjo, Fernando B. ; González-Herráez, Miguel ; Lahourcade, Lise ; Monroy, Eva ; Fernández, Susana: High-surface-quality nanocrystalline InN layers deposited on GaN templates by RF sputtering. In: *Physica Status Solidi (A)* Bd. 208 (2011), Nr. 1, S. 65–69

[VuMe03] Vurgaftman, I ; Meyer, J R: Band parameters for nitrogen-containing semiconductors. In: *Journal of Applied Physics* Bd. 94 (2003), Nr. 6, S. 3675–3696

[VuMR01] Vurgaftman, I. ; Meyer, J. R. ; Ram-Mohan, L. R.: Band parameters for III-V compound semiconductors and their alloys. In: *Journal of Applied Physics* Bd. 89 (2001), Nr. 11 I, S. 5815–5875

[WaRe01] Wang, Kai ; Reeber, Robert R.: Thermal expansion and elastic properties of InN. In: *Applied Physics Letters* Bd. 79 (2001), Nr. 11, S. 1602–1604

[WaYo04] Wang, Xinqiang ; Yoshikawa, Akihiko: Molecular beam epitaxy growth of GaN, AlN and InN. In: *Progress in Crystal Growth and Characterization of Materials* Bd. 48–49 (2004), S. 42–103

[WCHH09] Weng, W.Y. ; Chang, S.J. ; Hsueh, T.J. ; Hsu, C.L. ; Li, M.J. ; Lai, W.C.: AlInN resistive ammonia gas sensors.pdf. In: *Sensors and Actuators B: Chemical* Bd. 140 (2009), S. 139–142

[WHMS97] Wickenden, Dennis K. ; Huang, Zhenchun ; Mott, D. Brent ; Shu, Peter K.: Development of gallium nitride photoconductive detectors. In: *Johns Hopkins APL Technical Digest (Applied Physics Laboratory)* Bd. 18 (1997), Nr. 2, S. 217–224

[Wiki00] Wikibooks: *The Opensource Handbook of Nanoscience and Nanotechnology*. URL https://en.wikibooks.org/wiki/Nanotechnology/AFM

[WPMI15] Weisbuch, Claude ; Piccardo, Marco ; Martinelli, Lucio ; Iveland, Justin ; Peretti, Jacques ; Speck, James S.: The efficiency challenge of nitride light-emitting diodes for lighting. In: *Physica Status Solidi (a)* Bd. 212 (2015), Nr. 5, S. 899–913

[Wu09] Wu, Junqiao: When group-III nitrides go infrared: New properties and perspectives. In: *Journal of Applied Physics* Bd. 106 (2009), Nr. 1, S. 11101

[WWCT14] Wu, Yue Han ; Wong, Yuen Yee ; Chen, Wei Chun ; Tsai, Dung Sheng ; Peng, Chun Yen ; Tian, Jr Sheng ; Chang, Li ; Yi Chang, Edward: Indium-rich InAlN films on GaN/sapphire by molecular beam epitaxy. In: *Materials Research Express* Bd. 1 (2014), Nr. 1, S. 15904

[WWLA04] Wu, J. ; Walukiewicz, W. ; Li, S. X. ; Armitage, R. ; Ho, J. C. ;

Weber, E. R. ; Haller, E. E. ; Lu, Hai ; u. a.: Effects of electron concentration on the optical absorption edge of InN. In: *Applied Physics Letters* Bd. 84 (2004), Nr. 15, S. 2805–2807

[WWSY03] Wu, J. ; Walukiewicz, W. ; Shan, W. ; Yu, K. M. ; Ager, J. W. ; Li, S. X. ; Haller, E. E. ; Lu, Hai ; u. a.: Temperature dependence of the fundamental band gap of InN. In: *Journal of Applied Physics* Bd. 94 (2003), Nr. 7, S. 4457–4460

[WWYA02] Wu, J. ; Walukiewicz, W. ; Yu, K. M. ; Ager, J. W. ; Haller, E. E. ; Lu, Hai ; Schaff, William J. ; Saito, Yoshiki ; u. a.: Unusual properties of the fundamental band gap of InN. In: *Applied Physics Letters* Bd. 80 (2002), Nr. 21, S. 3967–3969

[WZKS96] Walker, D ; Zhang, X ; Kung, P ; Saxler, A ; Javadpour, S ; Xu, J ; Razeghi, M: AlGaN ultraviolet photoconductors grown on sapphire. In: *Applied Physics Letters* Bd. 68 (1996), Nr. 15, S. 2100–2102

[YeWL08] Yeh, Tung-Sheng ; Wu, Jenn-Ming ; Lan, Wen-How: Electrical properties and optical bandgaps of AlInN films by reactive sputtering. In: *Journal of Crystal Growth* Bd. 310 (2008), Nr. 24, S. 5308–5311

[YeWL09] Yeh, Tung-Sheng ; Wu, Jenn-Ming ; Lan, Wen-How: The effect of AlN buffer layer on properties of AlxIn1−xN films on glass substrates. In: *Thin Solid Films* Bd. 517 (2009), Nr. 11, S. 3204–3207

[YIKH10] Yamamoto, Akio ; Islam, Md R. ; Kang, Ting Ting ; Hashimoto, Akihiro: Recent advances in InN-based solar cells: Status and challenges in InGaN and InAlN solar cells. In: *Physica Status Solidi (C)* Bd. 7 (2010), Nr. 5, S. 1309–1316

[YKDY09] Yang, J. H. ; Kang, S. M. ; Dinh, D. V. ; Yoon, D. H.: Influence of AlN buffer layer thickness and deposition methods on GaN epitaxial growth. In: *Thin Solid Films* Bd. 517, Elsevier B.V. (2009), Nr. 17, S. 5057–5060

[YKNK98] Yamaguchi, Shigeo ; Kariya, Michihiko ; Nitta, Shugo ; Kato, Hisaki ; Takeuchi, Tetsuya ; Wetzel, Christian ; Amano, Hiroshi ; Akasaki, Isamu: Structural and optical properties of AlInN and AlGaInN on GaN grown by metalorganic vapor phase epitaxy. In: *Journal of Crystal Growth* Bd. 195 (1998), Nr. 1, S. 309–313

[YKNT00] Yamaguchi, Shigeo ; Kariya, Michihiko ; Nitta, Shugo ; Takeuchi, Tetsuya ; Wetzel, Christian ; Amano, Hiroshi ; Akasaki, Isamu: Anomalous features in the optical properties of Al1−xInxN on GaN grown by metal organic vapor phase epitaxy. In: *Applied Physics Letters* Bd. 76 (2000), Nr. 7, S. 876–878

[YLYW12] Yen, Cheng Hsiung ; Lai, Wei Chih ; Yang, Ya Yu ; Wang, Chun

Kai ; Ko, Tsun Kai ; Hon, Schang Jing ; Chang, Shoou Jinn: GaN-based light-emitting diode with sputtered AlN nucleation layer. In: *IEEE Photonics Technology Letters* Bd. 24 (2012), Nr. 4, S. 294–296

[YMAN09] Yamaguchi, T. ; Muto, D. ; Araki, T. ; Nanishi, Y.: Growth and characterization of N-polar and In-polar InN films by RF-MBE. In: *Journal of Crystal Growth* Bd. 311 (2009), Nr. 10, S. 2780–2782

[YSZP73] Yim, W M ; Stofko, E J ; Zanzucchi, P J ; Pankove, J I ; Ettenberg, M ; Gilbert, S L: Epitaxially grown AlN and its optical band gap. In: *Journal of Applied Physics* Bd. 44 (1973), Nr. 1, S. 292–296

[YuMa03] Yu, E. T. ; Manasreh, M. O.: *III-V nitride semiconductors: Applications and device*. London : Taylor & Francis, New York, 2003

[YWYL11] Yun, Lijun ; Wei, Tongbo ; Yan, Jianchang ; Liu, Zhe ; Wang, Junxi ; Li, Jinmin: MOCVD epitaxy of InAlN on different templates. In: *Journal of Semiconductors* Bd. 32 (2011), Nr. 9, S. 93001

[YYHH03] Yoshimoto, Masahiro ; Yamamoto, Hiroaki ; Huang, Wei ; Harima, Hiroshi ; Saraie, Junji ; Chayahara, Akiyoshi ; Horino, Yuji: Widening of optical bandgap of polycrystalline InN with a few percent incorporation of oxygen. In: *Applied Physics Letters* Bd. 83 (2003), Nr. 17, S. 3480

List of publications

The following publications have provided the material for this doctoral dissertation.

International Journals

1. **Development of AlInN photoconductors deposited by sputtering.** A. Núñez-Cascajero; M. Jiménez-Rodríguez; E. Monroy; M. González-Herráez; F. B. Naranjo. *Phys. Status Solidi (A) (2017).*

2. **In-rich $Al_xIn_{1-x}N$ grown by RF sputtering on sapphire: from closely-packed columnar to high-surface quality compact layers.** A. Núñez-Cascajero; S. Valdueza-Felip; L. Monteagudo-Lerma; E. Monroy; E Taylor-Shaw; R W Martin; M. González-Herráez; F. B. Naranjo. *J. Appl. Phys. D: Appl. Phys. 50, 065101 (2017).*

3. **Study of high In-content AlInN deposition on p-Si (111) by RF sputtering.** A. Núñez-Cascajero; L. Monteagudo-Lerma; S. Valdueza-Felip; C. Navio; E. Monroy; M. González-Herráez; F. B. Naranjo. *Jpn. J. Appl. Phys. 55, 05FB07 (2016).*

4. **Infrared SPR sensing with III-nitride dielectric layers**. A. Núñez-Cascajero, Ó. Estéban, J. A. Méndez, M. González Herráez, F. B. Naranjo. *Sens. Actuators, B 223, 768-773 (2016).*

5. **Morphology and arrangement of InN nanocolumns deposited by radio-frequency sputtering: effect of the buffer layer**. L. Monteagudo-Lerma, S. Valdueza-Felip, A. Núñez-Cascajero, A. Ruiz, M.

González-Herráez, E. Monroy and F.B. Naranjo. *J. Cryst. Growth 434, 13-18 (2016).*

6. **Effect of the barrier thickness on the performance of multiple-quantum-well InGaN photovoltaic cells**. L. Redaelli, A. Mukhtarova, A. Ajay, A. Núñez-Cascajero, S. Valdueza-Felip, C. Durand, J. Eymery and E. Monroy. *Jpn. J. Appl. Phys., 54, 072302 (2015).*

7. **High In-content InGaN layers synthesized by plasma-assisted molecular-beam epitaxy: Growth conditions, strain relaxation, and In incorporation kinetics.** S. Valdueza-Felip, E. Bellet-Amalric, A. Núñez-Cascajero, Y. Wang, M.-P. Chauvat, P. Ruterana, S. Pouget, K. Lorenz, E. Alves, and E. Monroy. *J. Appl. Phys. 116, 233504 (2014).*

8. **Two-step method for the deposition of AlN by radio-frequency sputtering**. L. Monteagudo-Lerma, S. Valdueza-Felip, A. Núñez-Cascajero, M. González-Herráez, E. Monroy, F.B. Naranjo. *Thin Solid Films 545, 149-153 (2013).*

National book chapters

1. **Desarrollo de nitruros basados en InN para aplicaciones fotovoltaicas.** A. Núñez-Cascajero, L. Monteagudo-Lerma, M. Jiménez-Rodríguez, S. Valdueza-Felip, E. Monroy, A. Ruiz, M. González-Herráez and F. B. Naranjo. *Quintas Jornadas de Jóvenes Investigadores de la Universidad de Alcalá 65-74, ISBN: 978-84-16133-98-7 (2016).*

2. **Estudio y aplicaciones de láseres de pulsos ultracortos basados en anclaje de modos.** M. Jiménez-Rodríguez, A. Núñez-Cascajero, L. Monteagudo-Lerma, F. B. Naranjo and M. González-Herráez. *Quintas Jornadas de Jóvenes Investigadores de la Universidad de Alcalá 93-102, ISBN: 978-84-16133-98-7 (2016).*

3. **Optical properties of low-Al content AlInN films deposited by reactive radio-frequency sputtering**. A. Núñez-Cascajero, L. Monteagudo-Lerma, M. González-Herráez, A. J. López, F. B. Naranjo. *Libro*

de Actas de la 8ª Reunión Española de Optoelectrónica 467-471, ISBN: 978-84-88754-21-9 (2013).

4. **Guías de onda de puntos cuánticos de GaN/AlN actuando como absorbents saturables altamente eficientes a 1.55 µm.**: L. Monteagudo-Lerma, S. Valdueza-Felip, A. Núñez-Cascajero, F. B. Naranjo, P. Corredera, L. Rapenne, E. Sarigiannidou, G. Strasser, E. Monroy, M. González-Herráez. *Libro de Actas de la 8ª Reunión Española de Optoelectrónica 22-26, ISBN: 978-84-88754-21-9 (2013).*

Contributions to conferences

- 28 contributions to international and national conferences.